OPTICAL FIBER-BASED MULTI-DIRECTIONAL FABRY-PEROT INTERFEROMETRY PROBE

by

Farzaneh Shabahang

A dissertation submitted to the faculty of
The University of North Carolina at Charlotte
in partial fulfillment of the requirements
for the degree of Doctor of Philosophy in
Optical Sciences and Engineering

Charlotte

2022

Approved by

____
Dr. Stuart. T. Smith

____
Dr. Angela Davies Allen

____
Dr. Greg Gbur

____
Dr. Tsing-Hua Her

____
Dr. Ethan Chiang

ABSTRACT

FARZANEH SHABAHANG. Optical Fiber-Based Multi-Directional Fabry-Perot interferometry Probe.

(Under direction of DR. STUART. T. SMITH)

The motivation of this thesis is to create an optical probe for the measurement of surfaces in confined spaces. This thesis presents design and operation of an optical fiber-based probe to measure a surface profile or relative displacement of external surfaces, with the vertical range of 3 nanometers to 300 micrometers and resolution of 3.25 nm. Three different probe designs have been fabricated and tested. These three probes are classified as; a single-axis, dual-axis non-simultaneous and dual-axis simultaneous measurements. The main common components of the probe system are; Graded index lens (GRIN lens) for focusing light onto the surface, two by one fiber couplers/ splitters, photodetectors, single mode optical fibers, piezo electric actuators, and single-mode laser diode coherent sources.

Displacement is measured by mechanically modulating the optical cavity formed by an internal surface and the external surfaces being measured, each cavity of which comprises a Fabry-Perot interferometer. To modulate the phase for each of the designed probe models, a piezo electric actuator is used to oscillate the GRIN lens sinusoidally along the optical axis and perpendicular to the external test surface, with a desired frequency of modulation.

For harmonics extraction, quadrature detection and phase unwrapping, a LabVIEW FPGA program has been implemented.

For the single-axis surface measurement probe, a closed loop-controlled scanning stage was designed and fabricated using a voice coil and mechanical flexures. A specimen attached to the scanning stage is translated under the vertical probe to measure the surface profile. The range of this scan is 1.2 mm with a resolution of traverse 17.5 μm and can scan the surface profile with speed of 1 mm/sec. The working distance of the probe is a flexible number depends on the assembly of GRIN lens and fiber tip and can change between 0 to 20 mm.

For the dual-axis displacement measurement probe, two plain mirrors were attached to separate piezoelectric translation stages with their translation axis along each probe axis. Movement of each stage is measured using capacitance displacement gauges (Lion Precision CPL-190) and will mimic the effect of scanning. During experiments, each of the piezoelectric actuators is energized using a slowly, sinusoidally varying voltage resulting in a peak to valley motion of the surfaces typically of around two micrometers amplitude (corresponding to between six to ten optical fringes). The results of both non-simultaneously and simultaneously independent displacement measurements of plain mirrors is presented in this thesis. Uncertainty measurements is calculated for each probe axis and a result of 8.1 nm rms noise was measured for them.

The reason for using optical fibers and a GRIN lens in this study is to make the probe as compact and flexible as possible to be appropriate for scanning inaccessible, hard to reach surfaces such as inside of a hole or barrel or any other hard to reach areas which is not possible to scan with commercial lens-based microscopes. Also, the multi-directional optical fiber probe design, increase the flexibility of surfaces scan substantially relative to the available surface measurement fiber-based products.

ACKNOWLEDGMENTS

I would like to thank my advisor, Dr. Stuart T. Smith, for his immense support and guidance over the years. Secondly, I would like to send a very special thanks to my parents Sorour and Yousef for their unwavering support. Additionally, I would like to thank UNCC Center for Precision Metrology and National Science Foundation (NSF) for their financial and scheduling support that made this possible. I would also thank Dr. Angela Allen, Dr. Greg Gbur and Dr. Tsing-hua Her who will be putting time and effort now and in the future as my thesis defend committee members. Lastly, there are several individuals who helped make this work possible, including Jeffery thousand, Brian Dutterer, Scott Williams, Masoud Arablu, Kumar Arumugam, DJ Hastings and Mohammad Dolatshahi.

TABLE OF CONTENTS

LIST OF FIGURES

LIST OF TABLES

CHAPTER 1 INTRODUCTION

1-1 MOTIVATION AND GOALS

The work of this thesis was motivated by conversations with industrial affiliates who were not able to find commercial probes for metrological inspection of features inside confined spaces. Examples of desired measurements include mainly small holes and turbine fixturing geometries, and other features such as trenches, flat surfaces, with limited access. Additionally, a large majority of these applications are part of large structures that cannot be transported or fit into measuring equipment in a metrology laboratory.

It was postulated that an interferometric, fiber-based, non-contact, optical probe could have the potential to be fabricated from small components and be capable of measurement bandwidth that would enable high resolution rapid surface scanning. As a consequence, the goal of this thesis is to realize metrological optical probing using fiber-based probes to overcome the range and space limitation of current systems and achieve an accessible fiber optics probe to measure unlimited range of hard-to-reach surfaces with a high flexibility and an acceptable speed of scan. To realize this goal, it has been necessary to design, manufacture, fabricate and evaluate a variety of probes with each successive prototype addressing issues revealed by the experiments. As a consequence of this evolutionary process this thesis collects the common development activities for each successive probe in themed chapters, these being; implementation approach, design, performance testing and evaluation, surface measurements, and conclusion and future work.

To create these fiber probes, many challenges had to be addressed. The first task was to fabricate and optimize a Fabry-Perot fiber-based interferometer using optical fibers, fiber coupler/splitters, photodetector, coherent laser diode source and create testing facilities to evaluate the performance of the probes for scanning surface profiles. A specification table including vertical and lateral resolution, vertical range (lateral range is unlimited), maximum lateral speed of scan and RMS values and standard deviation of the measurements was created to form a baseline comparison between probe designs. For maximizing the lateral resolution of surface profile measurement, a GRIN lens is used to focus the laser spot onto test surfaces. One major step was to overcome laser instability problems by designing and implementing a diode laser stabilization system. Also, a study to evaluate different laser sources and necessary current and temperature control systems was undertaken. For all probes, a mechanical modulation of the reference mirror in the interferometer configurations was used to create a quadrature signal from which optical phase could be extracted. Creating a mechanical modulation system to apply the maximum frequency of modulation on both single-axis and dual-axis configurations of the design represented another design challenge in this project. The final challenge was to design an opto-mechanical probe system to operate each of the single-axis and the dual-axis configurations. From these studies a multi-directional, Fabry-Perot fiber-based interferometer probe capable of scanning multi surfaces independently and simultaneously, was designed, manufactured, assembled, and tested. A list of novel measurement techniques created during these studies are;

- Design, manufacture, and performance evaluation of a fiber Fabry Perot cavity probe based on mechanical modulation system with lateral resolution enhancement using a GRIN lens.
- Two-axis simultaneous measurements of dynamically varying Fabry Perot cavity lengths providing similar performance specifications for each axis.
- Working in the visible spectrum using low-cost components in a compactly packaged device.

The major effort of this thesis was trying to separate the measurement signal from a variety of noise disturbances. Major among sources of errors are

- Reflections within the optical system
- Temperature sensitivity of the optics and in particular the optical fibers
- Low signal strength due to the low reflectivity of the reference surfaces

- Mechanical vibration, electrical noise, and digitization noise of ADC and DAC electronics

All of the above contribute to a reduction in fringe visibility. Other sources of errors will include;

- Efficiency of the fiber coupler.
- Reflection of the surface.
- Surface slope.
- Distance of specimen surface relative to focal plane.

Each of these factors reduce the amplitude of the signal thereby reducing the signal to noise ratio.

The major goal of the thesis is to validate operation of a multi-axis interferometric probe. This has been demonstrated by simultaneously measuring moving surfaces into orthogonal directions. Results from these experiments provide the complete system noise measurement for both stationary and moving surfaces. The influence of specimen reflectivity and surface slope have not been evaluated and remain a topic for future work. Noise measurements and other performance testing results are presented in chapter 5 and summarized in the conclusions in chapter 7.

LITERATURE SURVEY

The scope of this literature survey encompasses all the optical methods for the quantitative measurement of surface topography. Such instruments are split into two categories, these being conventional lens-based instruments and optical fiber surface probes. Each category is discussed in separate sub-sections below. Interestingly, any of the lens-based instruments are currently commercially available while fiber-based probes are predominantly still the topic of laboratory research. However, a drawback of the lens- based systems is the large volume of the optics and short working distance that precludes measurements in confined spaces.

1-2-1 DEVICES AND METHODS IN THE FIELD OF OPTICAL PROFILE AND SURFACE MEASUREMENT

To improve quality control, manufacturing surfaces with small tolerances need precise measurement techniques. A broad variety of approaches for high precision profilometry and surface measurement have emerged in the recent years. These may be divided into two groups; optical and non-optical surface measurement (Lee et.al, 2012).

Non-optical techniques can be divided into mechanical techniques, electrical techniques and microscopic techniques include resistance, capacitance, and inductance measurement methods. Stylus profilometry, scanning electron microscopy (SEM), scanning probe microscopy (SPM) and atomic force microscopy (AFM) are some examples. These techniques usually have nonlinearity and small dynamic range and cannot meet the requirements to profile manufacturing surfaces.

Laser trigonometry, structured light and time of flight are some examples of optical techniques. Other, more commonly used, methods of optical surface measurement include white light interferometry, confocal interference microscopy, spectroscopic confocal microscopy, Fizeau interferometry, optical coherence tomography, and digital holographic microscopy which are discussed in this section. These more commonly used methods have the advantage of high resolution and large measurement range (Wang et.al, 2017).

1-2-1-1 WHITE LIGHT INTERFEROMETRY

One of the most important methods of non-contact surface profilometry is interferometry. A very fast, accurate and repeatable technique in this field is phase-shifting interferometry (PSI) but it has some limitations. Surface discontinuities greater than a quarter-wavelength cannot be measured with a single wavelength measurement because of phase ambiguity. One way of solving this issue is using multiple wavelength measurement which still suffer from wavelength inaccuracy and environmental instability.

White light interferometry (SWLI) or coherence scanning microscopy (CSM) is a method that has overcome many of these roughness and discontinuity measurement problems (Groot, 2015).

Advantages of coherence scanning microscopy over conventional microscopy systems are a high lateral and vertical resolution in nanometer range and ability of scanning a large variety of surfaces having different reflectivity. (Lee et.al, 2012).

White light interferometry uses a Michelson configuration with a spatially incoherent broadband light source. In this technique a target sample will be scanned in z- axis by mechanically moving the specimen in the beam axis or moving the reference arm along that axis. During the scan, white light fringes are monitored for each point of (x, y) image. A coherence function is given by the envelope of these fringes. This function can be demodulated and gives back the peak amplitude of the envelope A (x, y) and corresponding to the measured z-location of the peak Z (x, y). Taken over all points, a high lateral and vertical resolution image (x, y, z) of the object will result (Lee et.al, 2012). Figure 1 shows a schematic of a white light interferometry system.

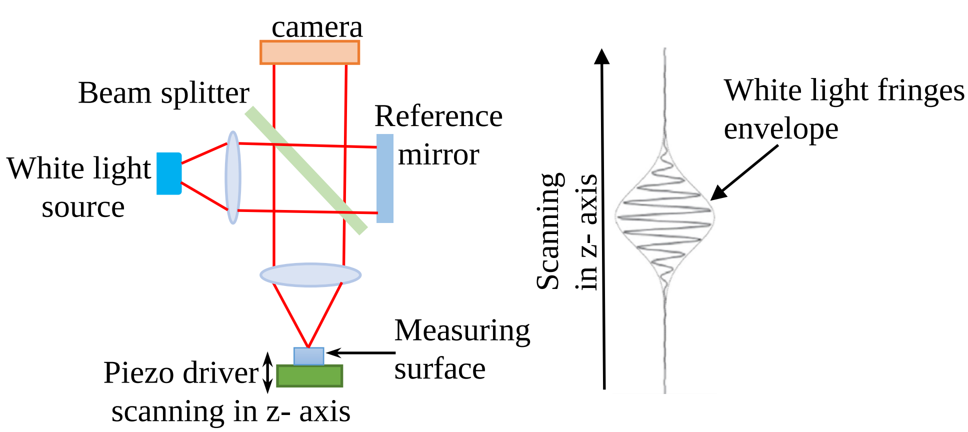

Figure 1. Schematic diagram illustrating the operation of a white light interferometer.

Coherence scanning microscopy started with the work of (Davidson et.al, 1987). He was trying to scan semiconductor surfaces with a sufficiently higher resolution relative to the conventional interferometers on fine features. After that (Dresel et. al, 1992) realized that by generating completely random speckles it is possible to measure a surface with sufficient roughness. This provided the ability to launch commercial products to measure inaccessible surfaces for both rough surface testing and high-precision measurement without the need to spatially unwrap fringes. Today most of the interference microscopes for evaluation of areal surface topography operate according to the CSMI principle (Groot, 2015). CSM have unique specifications such as vertical resolution of 100 nm, lateral resolution of 340 nm, a high spectral bandwidth of 400-1000 nm, a relatively broad vertical range of 150 µm – 20 mm and speed of 34 µm/s.

1-2-1-2 CONFOCAL INTERFERENCE MICROSCOPY

Confocal interferometry was first invented by Marvin Minsky (Minsky, 1961) who generated confocal images of specimens. Minsky's original design only required one lens and one pinhole. This invention did not become a commercial microscopy technique until computers had sufficient processing power to obtain images in times that were comparable to other microscopy systems.

Confocal microscopy technique is basically a sectioning imaging method that uses pinholes or slits to make a structured illumination pattern and detect the restricted backscattered or reflected pattern from the specimen with a similar configuration of pinholes and slits in front of the detector. This restricted pattern blocks the light that comes from the regions of the surface out of the focal plane of the microscope's objective and gives back a high contrast image of a particular section of specimen for which the total image intensity is also a maximum when the surface is at the focal plane. By moving the stage along vertical axis and imaging section by section, a 3D image of specimen will be achieved.

The largest commercial application of confocal microscopy is imaging biological samples containing fluorophores that get excited by illumination. This feature of biological samples enables the observer to be able to image them easily by illuminating and detecting reflection from a particular point within or at a surface. Confocal microscopy helps to block the out of focus fluorescence that reduces the

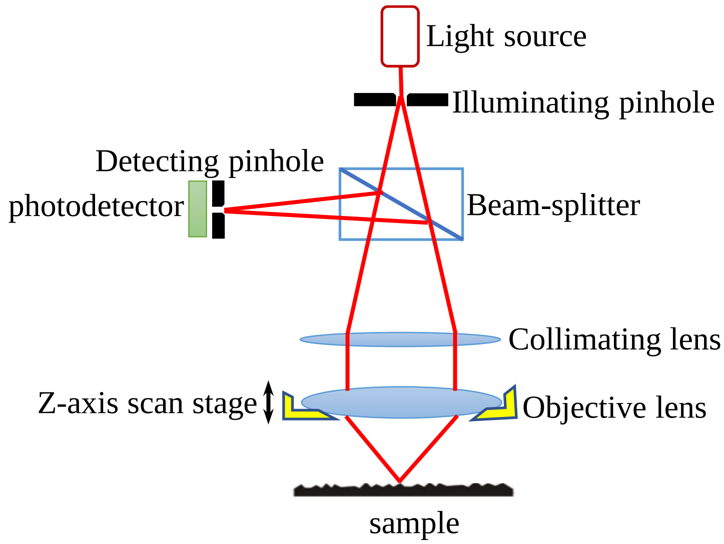

Figure 2. Schematic of confocal microscopy.

contrast of the in-focus plane and provide a high contrast detailed image of the required section. (Artigas, 2011). Figure 2 illustrates a schematic of confocal microscopy.

1-2-1-3 SPECTROSCOPIC CONFOCAL MICROSCOPY

Chromatic confocal microscopy uses chromatic dispersion of light and different focal length of each wavelength to extract the topography of a surface. Unlike the conventional confocal microscopy, in chromatic confocal microscopy a chromatic objective lens is used to create chromatic dispersion and a spectrometer is replaced with the photodetector to analyze the detected spectrum of reflected light. In that case different colors with different focal point can scan different layers of the specimen and extract the topography and height of each layer. This eliminates the need of vertical scanning and captures the topography of many layers at once. Alternatively, for specularly reflecting surfaces it functions as a displacement sensor. Chromatic confocal microscopy can be a good non- contact substitute for stylus profilometry and has been used in texture measuring instruments, roundness measurement instruments and coordinate measuring machines (CMMs) for more than 20 years (Blateyron,2011). Figure 3 is an illustration of a color confocal microscope. A plot of wavelength-to-depth codification at 0 scanning angle is shown in Figure 4 (Byung Seon Chun et.al, 2009).

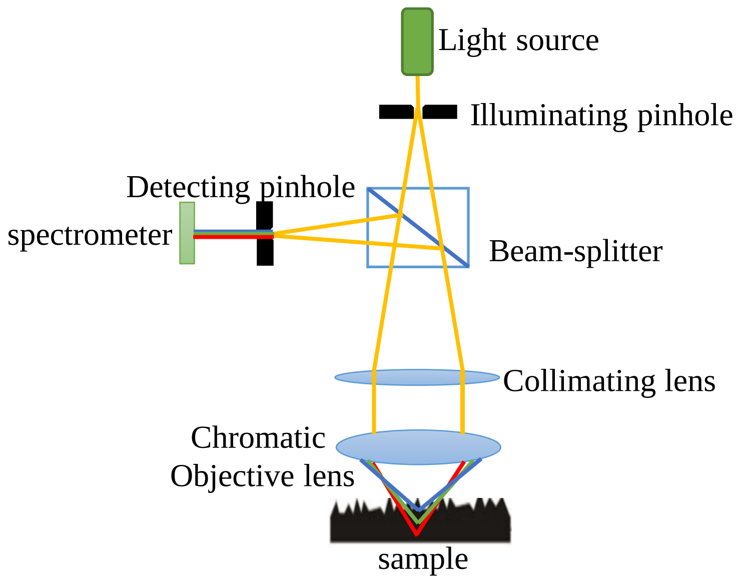

Figure 3. Schematic of color confocal probe.

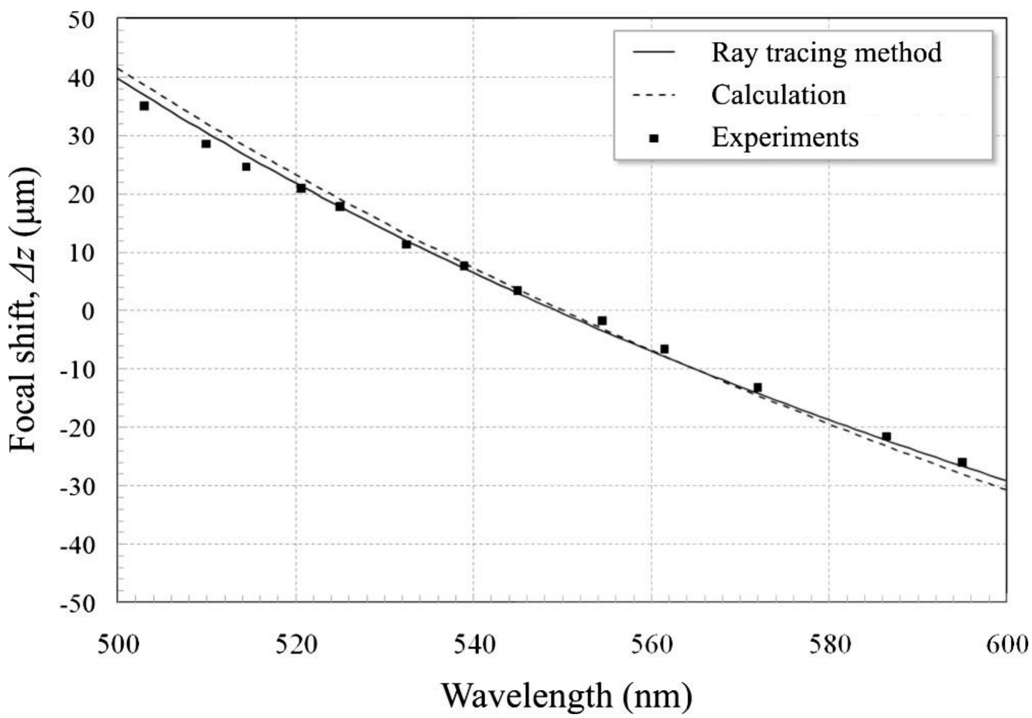

Figure 4. Plot of wavelength-to-depth codification at 0 scanning angle.

1-2-1-4 FIZEAU INTERFEROMETER

Fizeau interferometer was first invented by Armand Hippolyte Louis Fizeau. He invented the interferometer configuration for measurements of glass parameters in 1862. The modern form of today's Fizeau interferometer was created in 1970 after invention of the modular Fizeau interferometer with a laser source and computerized phase measurements. In 1972 Carl Zanoni and George Hunter at ZYGO, made a new Fizeau interferometer by putting a simple polarizer in front of a multi-mode, low-cost laser with a long coherence length (Apre-instruments, 2018).

A Fizeau interferometer is basically a Michelson interferometer with the major difference being that it is used to measure high reflectivity mirrors. The interferometer is consist of an optical flat having two surfaces, one, a parallel surface and the other, a slightly tilted surface respect to the test surface as shown in Figure 5. This tilted angle is less than a milliradian. The interference pattern measured by the detector will be the superposition of beams reflected from the flat surface and tilted surface. Because of the optical path difference between the reflection from the tilted surface and the flat surface, an interferometric fringe pattern forms were this superposition happened on the detector. This pattern will be a clear fringe structure with straight interference stripes for ideal flat test surface. Any deviations between the surface shapes lead to distortions of those stripes (Kajava, 1994).$OPD = 2\alpha y$

$$OPD = \frac{\lambda}{2} \qquad DESTRUCTIVE$$

$$OPD = \lambda \qquad CONSTRUCTIVE$$

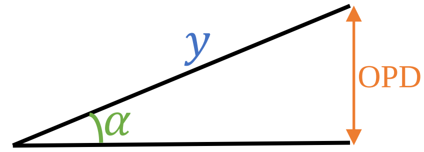

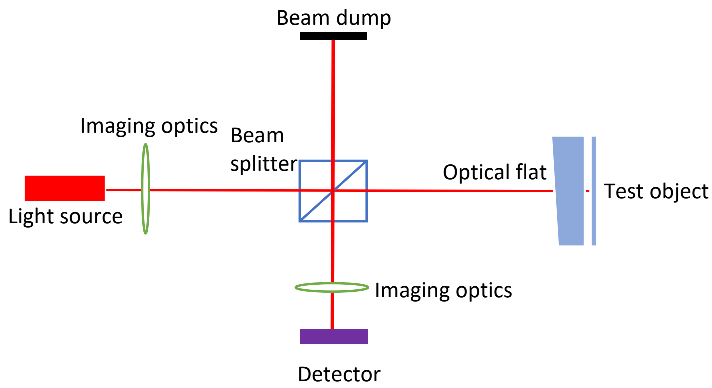

Figure 5 schematic of Fizeau interferometer

1-2-1-5 MULTI WAVELENGTH INTERFEROMETRY

Single wavelength phase shifting interferometry is a powerful tool that has a good vertical resolution and sensitivity appropriate for scanning micro-machined surfaces. Limitations of this method show up in scanning surfaces with step heights more than a half of wavelength. When phase changes more than π between two adjacent pixels the phase ambiguity problem causes error in the result scan.

One way of solving this problem is using an infrared (IR) light source with longer wavelength instead of visible light. This will extend the range of scanning but not solve the problem completely. White light interferometry is another approach to solve the problem of discontinuity, but it has the limitation of requiring large number of frames to be recorded.

A better way is using two wavelength phase shifting interferometry or multi wavelength phase shifting interferometry (Paul Kumar, 2008).

Using a two or multi-color source, can cause a significantly longer range of scan, without ambiguity and without sacrificing the accuracy of the single-source instrument (Groot, 2015). A schematic of multi-wavelength interferometry is shown in Figure 6. This method is basically combining different interferometers into one to cover a broad range of scan with different resolution. The idea comes from the phase unwrap equation (1-1) which determine the resolution and range of vertical scan depending on the wavelength of the light source being used.

$$\Delta L=\varphi/2\pi\ \lambda\pm N\lambda \qquad 1\text{-}1$$

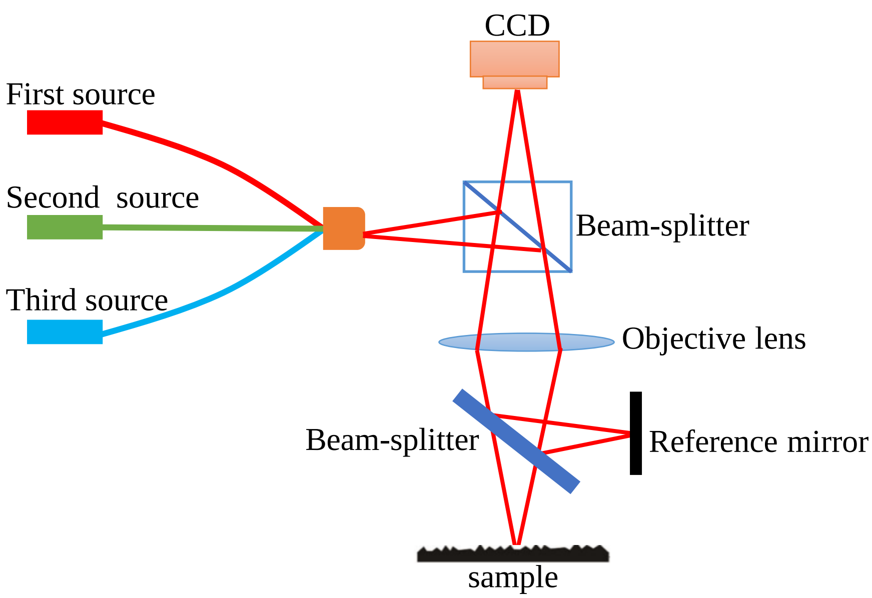

Figure 6. Schematic of multi wavelength interferometer

Although multi wavelength interferometry has became a novel method of scanning and overcome many limitations of conventional techniques, it has the disadvantage of needing multiple coherent sources or tunable sources which makes it costly and challenging.

1-2-1-6 OPTICAL COHERENCE TOMOGRAPHY

Optical coherence tomography (OCT) is commonly associated as a medical imaging technology. Three-dimensional medical imaging techniques such as magnetic resonance imaging (MRI), functional magnetic resonance imaging (FMRI), X-ray computed tomography, radioisotope imaging (PET and SPECT) and ultrasound and diffuse optical tomography, are all limited by low spatial resolution. Among all those, optical coherence tomography allows three-dimensional cross-sectional imaging within biological samples with a good spatial resolution of 10 μm or less (Popescu. Et.al, 2011). Even between high resolution imaging techniques like conventional and confocal microscopy and multi wavelength interferometry, optical coherence tomography, has another advantage of penetrating deep under the surface of biological samples.

The OCT concept emerged in the late 1980s and rapidly developed as a technique enabling high-resolution, real-time, and in-situ imaging of tissue microstructure without the need for tissue excision and processing (Popescu. Et.al, 2011). Many fiber-based OCT probes have been produced, most of the commercial probes find application as a surgical diagnostic tool (Aumann S, 2019). Typically for these probes imaging is obtained by physically scanning the fiber tip (time-based OCT) or, more typically, by scanning the optical wavelength (frequency-based) (Suzuki T et.al, 2021). The advantage of these type of probes is that it is possible to obtain three dimensional images of multi-layer structures such as biological membranes in vivo using fiber imaging. In these applications, OCT is limited to materials with specific absorption and refractive properties (Brezinski M, 2014). Additionally, the lack of knowledge of optical properties in the region of imaging complicates its use for dimensional metrology (Bak E, 2021).

Optical coherence tomography works with a low-coherence light source. A two-by-two fiber coupler splits the light into two arms with same optical path. The fiber tip will be placing in front of a reference arm and the sample arm, as shown in Figure 7. When the sample is inhomogeneous, light will be backscattered when it encounters an interface between materials of different refractive index and will be detected using a detector. Because of the low coherence of the light an interfering fringe pattern will form on the detector with the light interfering from reference arm and sample arm, traveling with less than a half of wavelength difference. By translating the reference arm (A scan), the reference beam will interfere with the light coming from the relevant sampling backscattered light with appropriate optical path difference (Popescu D. P et al, 2011).

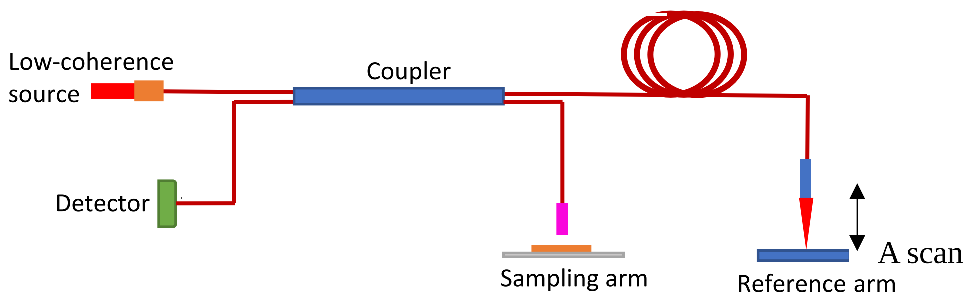

Figure 7. Schematic of optical coherence tomography

1-2-1-7 DIGITAL HOLOGRAPHIC MICROSCOPY

Dennis Gabor invented Holography in 1948 while he was trying to improve resolution of electron beam microscopy and realized that the diffraction pattern of the electron beam contains complete information regarding the amplitude and phase of the electron wave. After emerging high power coherent laser light sources and the ability of off-axis illumination with a separate reference wave Holography immediately applied to recording and imaging by visible light.

Digital holography replaces physical and chemical recording processes with electronic ones, and the optical reconstruction process with numerical computation. Schnars and Jueptner, in1994, were the first to use a CCD camera directly connected to a computer as the input and compute the image in a Fresnel holography setup.

In digital holography, the holographic interference pattern is optically generated by superposition of object and reference beams, typically using a Mach-Zehnder optical configuration, which is digitally sampled by a CCD camera and transferred to a computer as an array of numbers. The propagation of optical fields is completely described by diffraction theory, that is used for numerical reconstruction of the image as an array of complex numbers representing the amplitude and phase of the optical field. A basic digital holographic microscopy (DHM) setup consists of an illumination source, an interferometer, a digitizing camera, and a computer with necessary programs.

Digital holography offers several significant advantages, such as the ability to acquire holograms rapidly, availability of complete amplitude and phase information of the optical field, and versatility of the interferometric and image processing techniques. Indeed, digital holography by numerical diffraction of optical fields allows imaging and image processing techniques that are difficult or not feasible in real-space holography (Myung K. Kim, 2010). Figure 8 shows a schematic of a digital holography system.

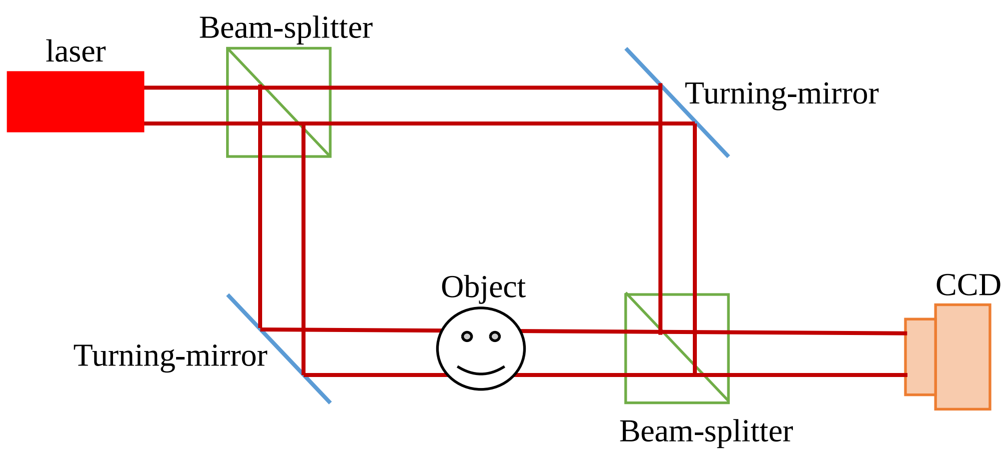

Figure 8 schematic of digital holography

In this section, devices, and methods in the field of optical surface measurement was listed and briefly described. Each of these methods have their own advantages and limitations but most of them are being commercialized and available as a product in the market. The specifications of measurements for described method, is presented in Table 1. This includes lateral and vertical range, lateral and vertical resolution, speed of scan and bandwidth.

Table 1 Optical surface topography instrument (conventional lens-based) performance specifications from commercial suppliers and relevant journal publications describing operation

Technique	Vertical Range	Speed	Bandwidth	Lateral Range	Vertical Resolution	Lateral Resolution	References
White light interferometry	150-20000 µm	34 µm/s	400-1000 nm	150 x 150 mm	0.1 µm	0.34 µm	[3,4]
Confocal interference microscopy		8 image/s	405-640 nm	12.7x12.7 mm	10 nm	0.2 µm	[5,6]
Spectroscopic confocal	30 mm		450 – 2500 nm	25 mm	5 µm	300 nm	[8]
Fizeau interferometer	4 m		633 nm	150 mm			[9,10]
Multi wavelength interferometry	200 µm	20 kHz	104 kHz	1.2 mm	0.01 nm	0.5 nm	[11]
Optical coherence tomography	1.9-20 mm	5.0-248 kHz	175-1325 nm	6 x 6 mm	3.0-14 µm	4-24 µm	[12-16]
Digital holographic microscopy	1.2 µm	25 MHZ	0.01 nm	1360×1024 pixels	0.1 nm	4.65 µm	[17,18]

1-2-2 OPTICAL FIBER PROFILING PROBES

Optical fibers offer a number of unique attributes such as flexibility to provide an illumination source in hard-to-reach places, multiplexing to switch sources or signals, remote sensing, low propagating loss, high sensitivity, low fabrication cost, small form factor, high purity of materials, simultaneous sensing ability, high temperature operation, and immunity to electromagnetic interference. As a consequence, over the last few decades optical fibers have been widely deployed in telecommunication, sensing, control, and precision industries. To date, a variety of studies have been undertaken to utilize optical fibers as sensing indicators for temperature, strain, pressure, rotation, displacement, refractive index (RI), polarization, and ultrasound (Lee, 2012)

Optical fiber profiling probes and sensors use the fibers to extend the flexibility of devices to measure inaccessible surfaces. They have the advantage of being capable of providing compact probes that overcomes this issue with the existing lens-based conventional profilometers and surface measurement devices that are currently commercially produced.

Figure 9 shows a block diagram of a fiber-based sensor or profiling probe that consist of four major elements of coherent source, optical fiber to transfer light from source to measurand, optical fiber to transfer light from measurand to optoelectronic detector and the signal processing circuits and software. The measurand or target of measurement can be different depends on which kind of sensor is going to be made and what kind of physical parameter is going to be measured. (Tiwari et.al, 2018).

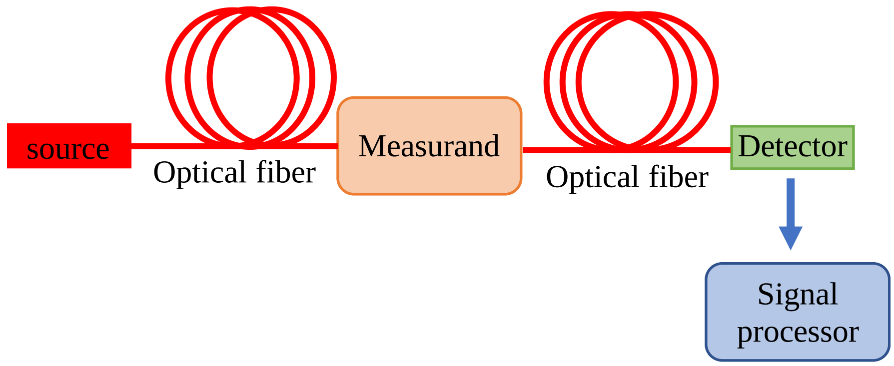

Figure 9 optical fiber profiling probes

Optical fiber probes are categorized into extrinsic and intrinsic groups. Extrinsic sensors are using the fiber, as a carrier which guide the energy or light to the head of probe and carry the reflection of light back to the sensor or detector without any modulation or change on the light inside the fiber. Intrinsic probes, on the other hand, operate through direct modulation of the light guided in the fiber by the measured parameter (measurand).

Extrinsic and intrinsic fiber-based sensors use four types of measuring method such as amplitude (intensity) sensors, wavelength (frequency) sensors, interferometric sensors, and polarimetric sensors. Below is a short description of each type.

1-2-2-1 AMPLITUDE (INTENSITY) SENSORS (EXTRINSIC)

Intensity based sensors are considered as extrinsic kind of optical fiber sensors. They are consisting of a light source and a detector and basically work based on a fact that the reflected intensity from the object to the detector is a function of distance between the light source/ detector and the object.

Intensity sensors are also sometimes called photonic sensors. They usually work using a single fiber or bundle of optical fibers for illumination and detection. There are different configurations for both.

The intensity detected into the detector follow a response function which is characterized by signals both at zero distance and at large distances, with an intensity peak at a specific distance, close to the fiber tips. The distance that yields the peak intensity is typically hundreds of micrometers and depends on the fibers, diameters, numerical apertures (NA) and the geometrical distribution of illumination and detection fibers. Based on this response function, the topography of the surface can be estimated (Berkovic et al, 2012).

One method to produce an intensity-based proximity sensor is to use an optical fiber bundle, the free end of each is the surface proximity sensor (Nan, 2016). This fiber bundle comprises a center fiber surrounded by a circular array of similar fibers. Light emerging from the central fiber is reflected from the surface back into the outer fibers with an intensity that is a function of the fiber probe to surface separation. This sensor has a high bandwidth but requires calibration and is sensitive to reflectance and scattering properties of the measured surface.

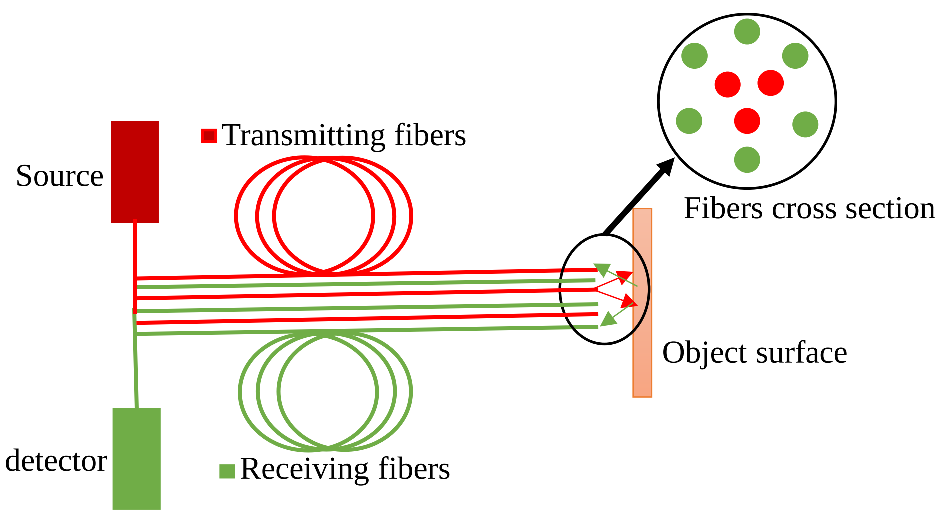

Figure 10 Schematic of intensity-based optical fiber probe

1-2-2-2 WAVELENGTH OR FREQUENCY SENSORS (INTRINSIC)

Frequency-based optical fiber sensors work based on the wavelength as the changing parameter measure perturbations on the measurand. Most of frequency fiber sensors are intrinsic. Fiber Bragg Grating is one of the most popular frequency fiber sensors that was first discovered by Ken Hill in 1978. FBG has many advantages such as low cost, small size, real-time response, high accuracy, high sensitivity, and immunity to electromagnetic interference. Various parameters, such as temperature, pressure, stress, and refractive index can be measured using FBGs. Current applications of fiber Bragg gratings are found in high temperature sensors, health and biomedical devices, structural engineering, industries, biochemical applications, radioactive environment, aerospace, maritime and civil engineering, and many other fields.

FBG is consist of several reflecting surfaces which reflect light with a resonance wavelength called FBG wavelength λ_B given by equation (1-2).

$$\lambda_B=2n\Lambda \qquad 1\text{-}2$$

where n is the refractive index and Λ the grating period and is produced by the constructive interference of all, reflected from different surfaces lights. Any perturbation in the extrinsic parameters such as length, temperature, pressure, or perturbations of air that affect the refractive index and causing a shift in the Brag wavelength, will be monitored in the reflected or transmitted spectrum of the grating (Kersey et.al, 1997). For example, the temperature sensitivity of a fiber-brag grating on pbs-doped silica is improved to 0.016 nm/°C within the temperature range of 20 °C to 150 °C (Xiangping Pan et al, 2018).

One application of FBG is making displacement sensors. By attaching the free end of the FBG to the displacing part, an increase in its length as the part moves will induce a strain in the fiber. This strain will be measured as a corresponding change in the reflected spectrum (Chen et.al, 2011).

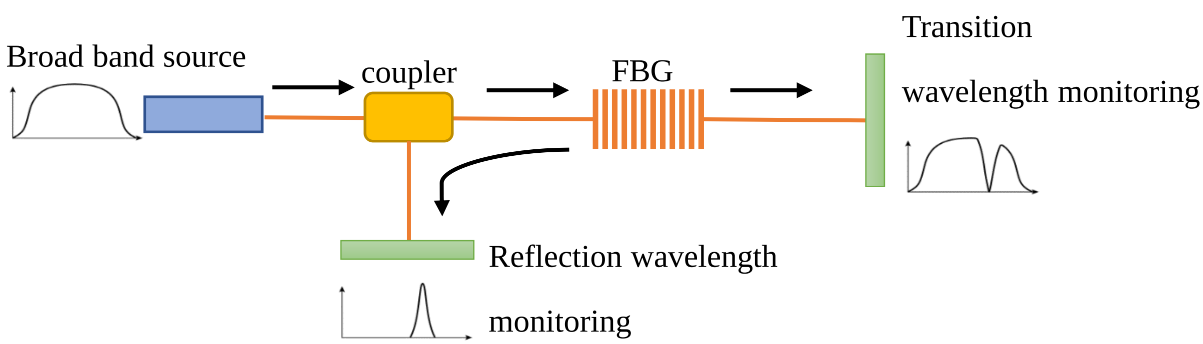

Figure 11 Schematic of Fiber Brag Grating (frequency-based) sensor

1-2-2-3 INTERFEROMETRIC SENSORS (EXTRINSIC OR INTRINSIC)

A fiber optic interferometer uses the interference between two beams that have propagated through different optical paths of either a single fiber or two different fibers with one of the optical paths arranged to be easily affected by external perturbations. Interferometers provide temporal and spectral information, for the detection of changes in the wavelength, phase, intensity, frequency, and bandwidth of the signal. These sensing approaches there are particularly useful because of the large dynamic range (often limited only by other technologies necessary to implement the method), high accuracy (with wavelengths often know to parts in 107 or more), and high sensitivity (sub-nanometer resolution can often be readily achieved).

Fiber optic interferometers can sense various physical parameters including temperature, strain, pressure, and refractive index. They are categorized into four types of optical configuration, these being; Fabry-Perot, Mach-Zehnder, Michelson and Sagnac.

1-2-2-3-1 Fabry- Perot interferometer

A Fabry-Perot interferometer is formed by two parallel surfaces with a fix distance. The resultant interference is the superposition of multiple reflections from these two surfaces. Fabry-Perot interferometer can be any type of extrinsic or intrinsic. In the extrinsic type, the interference occurs in an external cavity between the head of fiber and a parallel mirror.

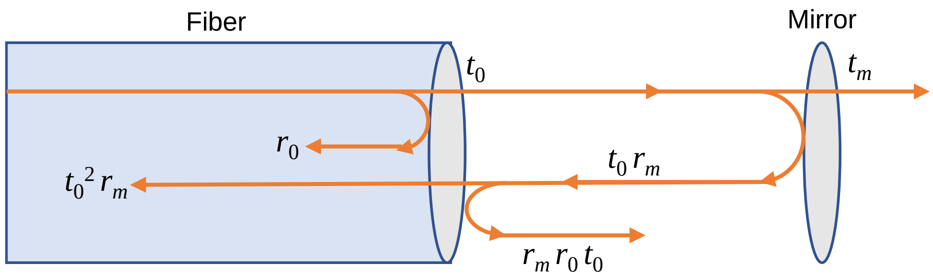

Figure 12 Fabry Perot interferometry

Extrinsic fiber Fabry-Perot cavity have some advantages and disadvantages. As an advantage they are good to obtain high finesse interference signal because of using mirrors with high reflectivity. Also, its fabrication is simple and low cost. However, they have the disadvantage of low coupling efficiency, careful alignment, and non-linear response.

In an intrinsic type of the fiber Fabry-Perot interferometry, the reflecting components and cavity are inside the fiber (Lee, 2012).

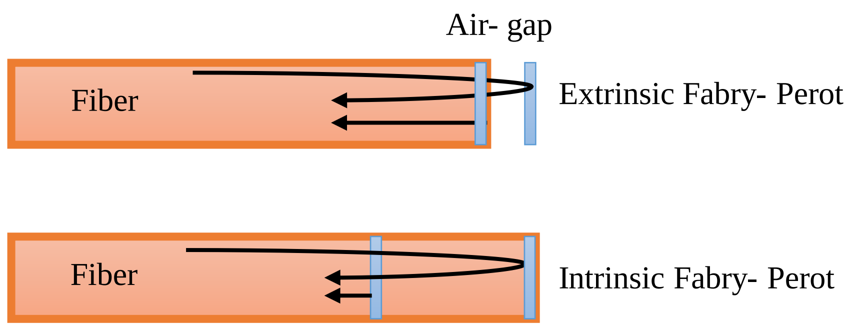

Figure 13 Fabry Perot interferometry Extrinsic & intrinsic

When two lights reflected from two surfaces of a Fabry- Perot cavity combine, a phase difference caused by optical path difference can be calculated based on the intensity of the superimposed detected light. See equation (1-3).

$$\Delta\emptyset = \frac{2\pi}{\lambda} n(2L) \qquad \text{1-3}$$

In practice, the interference will be the sum of increasingly attenuated signals traveling two, four, six, etc. times the length of the cavity ultimately resulting in non-linearities between the displacement an interferometer phase (Wilkinson and Pratt, 2011). This phase difference, in turn, depends on the wavelength, refractive index of cavity material and length of the cavity. With monitoring this phase difference many parameters such as temperature, pressure (affecting refractive index), cavity length (displacement) can be measured.

1-2-2-3-2 Mach – Zehnder interferometer

Mach-Zehnder interferometers are popular in many sensing applications because of their flexible configuration. They are simply consisting of a splitter to split the coherent light source into a reference arm and sensing arm, and a coupler to recombine them together and read the superposition into the detector. The sensing arm will be exposed to the measurand and every variation in the refractive index or optical path difference will be monitored in the detector with measuring the phase difference (Lee, 2012).

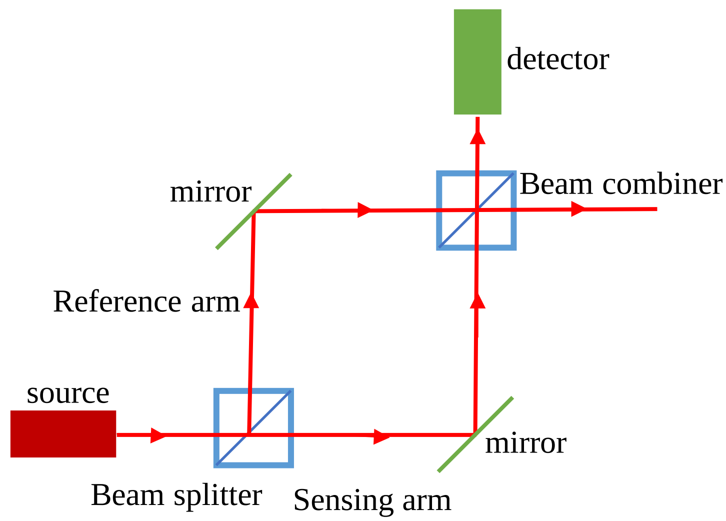

Figure 14 Mach Zehnder interferometry

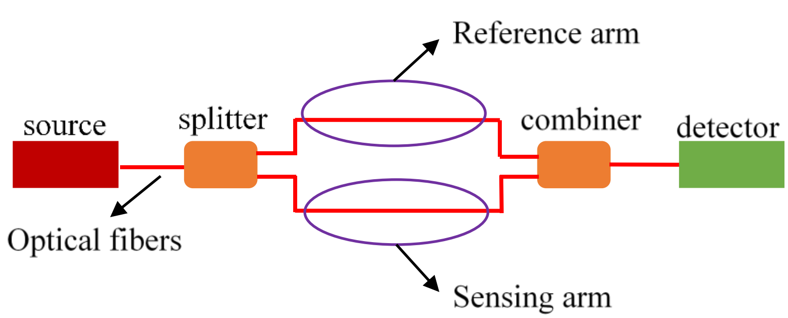

Figure 15 Fiber-based Mach Zehnder interferometer

1-2-2-3-3 Michelson interferometer

Michelson interferometer sensor is like a half of a Mach-Zehnder interferometer. It consists of two reference and sensing arms with a difference that the light is split and combines with the same beam splitter. Michelson interferometer is more compact relative to Mach-Zehnder, but it is necessary to adjust the difference between reference arm and sensing arm length to be within the coherence length. Like other types of interferometers, any change in the refractive index or optical path of sensing arm will be monitored at the detector as a phase difference (Lee, 2012).

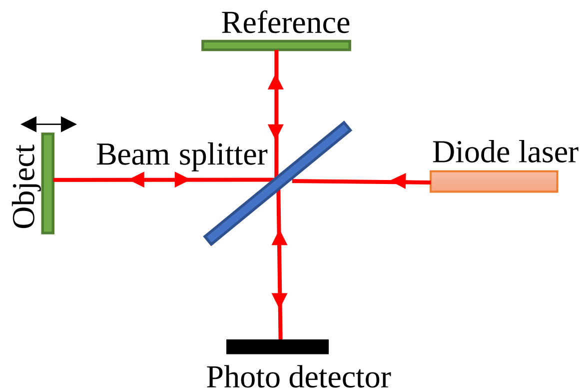

Figure 16 Michelson interferometer

Michelson optical fiber interferometers can also be configured using a two-by-two fiber optic coupler to split the laser light into sensing arm and reference arm and combine the reflected light back from both surfaces, see Figure 17. With emerging optical fibers and related fiber-based equipment such as fiber coupled detectors and pigtail lasers this technology is becoming an economic technique for optical fiber profilometry and surface measurement and is particularly suited for hard-to-reach areas and biomedical samples.

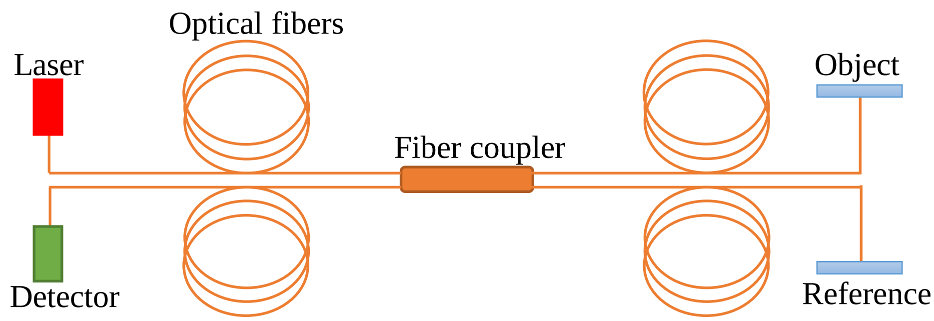

Figure 17 Fiber-based Michelson interferometer

1-2-2-3-4 Sagnac interferometer

Sagnac interferometers, also requiring only a single beam splitter, have several advantages of simple structure, easy fabrication, and environmental robustness. It consists of a loop in which two beams propagate along in counter directions with different polarization state. See Figure 18. The input light is split into two directions by a beam splitter and the two counter propagating beams are combined again with same beam splitter. The polarization dependent propagating speed of the mode guided along the loop will determine the optical path difference (Lee, 2012).

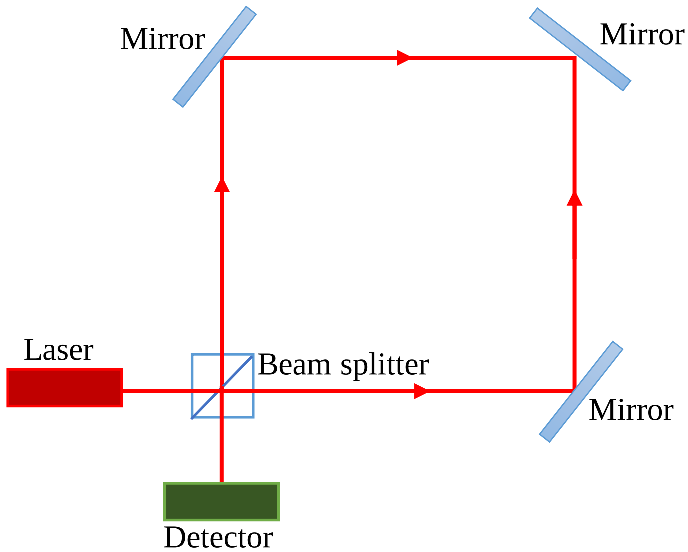

Figure 18 Sagnac interferometer

In fiber- based Sagnac interferometer a coupler splits the light into two directions of a loop fiber with two different polarization and couple them into the photodetector to interfere with a phase difference after passing through the sensing part of the optical fiber. See Figure 19.

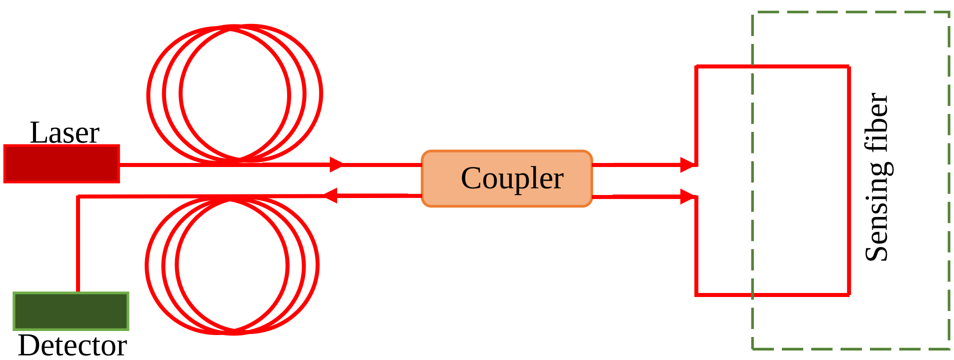

Figure 19 Fiber based Sagnac interferometer

1-2-2-4 HOMODYNE QUADRATURE LASER INTERFEROMETRY

Quadrature detection technique is a good way of displacement measurement laser interferometry using a single frequency source. Detecting a phase quadrature is feasible with interfering orthogonally polarized signals. In this method the displacement can be measured with a high sensitivity and the direction of displacement can be determine using the direction of quadrature, changing clockwise or counterclockwise. The accuracy of the measurement is dependent on the ellipse fit to the represented residue algorithm and the simple arctangent phase unwrapping program (Pozar and Mozina, 2011). A simple schematic of a HQLI setup is shown in Figure 20.

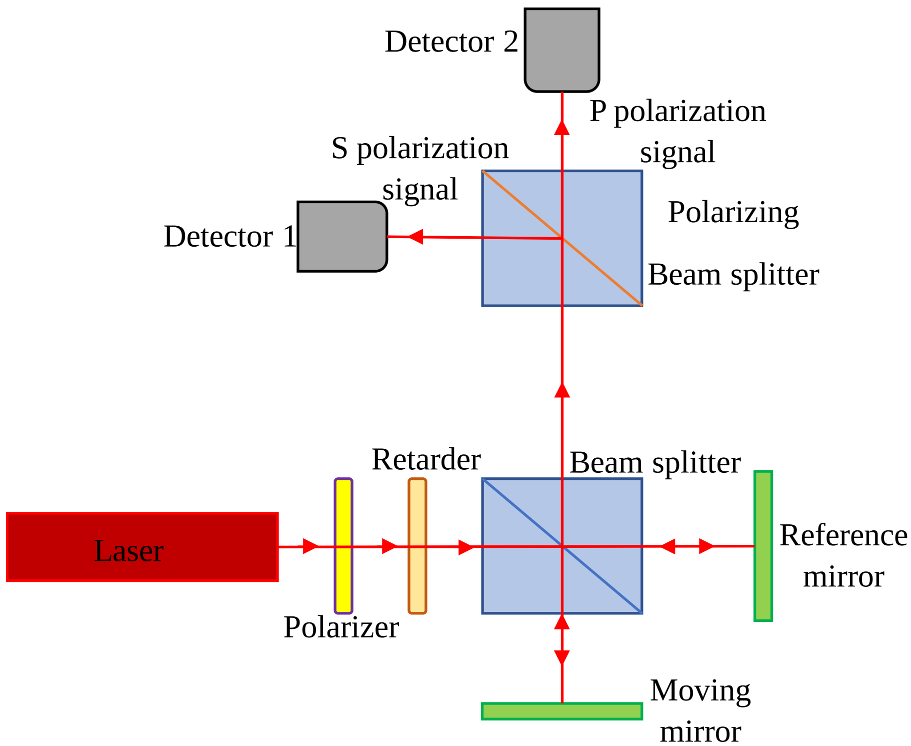

Figure 20. Schematic of a HQLI setup

In this figure it is shown that after circularly polarizing the signal using a polarizer and a retarder, the light goes through a Michelson interferometer including a reference mirror and a moving mirror (the measuring displacement surface). The light finally divides into P polarization signal and S polarization signal using a polarizing beam splitter and detect with different photodetectors in front of each signal. A quadrature can be formed with these two signals of orthogonal polarization to measure the displacement of moving mirror.

1-2-2-5 POLARIMETRIC SENSORS (INTRINSIC)

A pressure sensor using polarization maintaining optical fibers for a light with wavelength of 1300 nm has been successfully developed by (Chen and Bock, 2011). In this method a linearly polarized light will be launched into the fiber and be detected on the other end. A polarizer will be placed in front of the detector to determine the state of the polarization. Any change is the state of polarization such as temperature, pressure and noise contain information about the effecting parameters. Figure 21 shows a schematic of a fiber based polarimetric sensor.

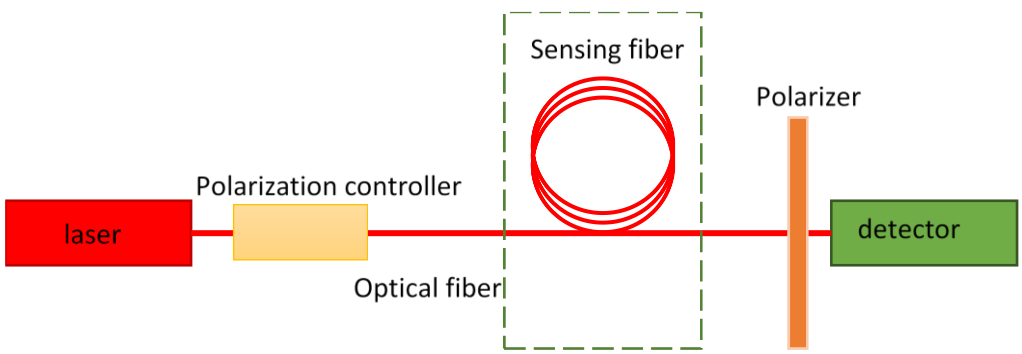

Figure 21 fiber-based polarimetric sensor

Fiber-based probes designed for quantitative surface topographic measurements, typically launch a modulated light source from a fiber onto specular surfaces and monitor the light that reflects back into the fiber. (Nowakowski et al. 2016) used a bare fiber with wavelength modulation of the source beam being used to obtain quadrature for phase detection. A drawback of this system was the large contact area and limited modulation frequency (1.2 kHz) of the 1550 nm laser source. Tao Jin et al (Tao Jin et al, 2021) also use a bare fiber probe and in this work provide phase modulation using an electro optic modulator in the fiber path. Both probe systems are capable of measuring probe to specimen variations of up to 20 mm. The first use of a GRIN lens to focus the beam of a fiber-based probe was presented by Schulz and Lehmann in 2013 (Schulz and Lehmann, 2013). In this work a probe is developed that comprises a flexible probe body to which is fastened the source optical fiber, GRIN lens, and a beam bender. A piezo electric element is used to mechanically modulate the optical path by bending the flexible probe body. This probe used two sources with wavelengths 1310 nm and 1550 nm (used to resolve phase ambiguities) and report profiles measured using the 1310 nm source. The profile presented in this paper is a triangular reference surface of amplitude 200 nm using a mechanical modulation of 300 Hz.

Table 2. Optical surface topography instrument (fiber profiling probes) performance specifications from commercial suppliers and relevant journal publications describing operation

Sensor Type	Vertical Range	Lateral Range	Vertical Resolution	Lateral Resolution	Speed	Bandwidth	Dimensions of probe	Sensing Methods	Ref
Intensity	150 µm	220 mm	1 µm	200 µm			1.4×0.5×.4 mm	external	[19]
Interferometric (Fabry Perot)	100 mm	unlimited	3.25 nm	17.5 µm	1 mm/s			external	[1,2,20,24,25,29,39]

1-2 NOVELTY OF THE PROBES PRESENTED IN THIS THESIS

The two-axis probe system presented in this thesis comprises a GRIN lens that focuses two diode sources of wavelengths 633 nm and 660 nm. These two wavelengths are split using a dichroic mirror so that each wavelength forms a separate measurement axis. Reflections from the surface return both beams back into the GRIN lens. Quadrature detection is obtained by mechanically modulating the probe (GRIN lens and optics assembly) in the two, orthogonal, directions of each of the beam axes. The mechanically modulated beams returning from the measured surfaces interact with the internal reflections at the GRIN lens-fiber interface. As a result of the interference, each wavelength will modulate at the frequency of the mechanical oscillation in each direction. In the probe of this study the mechanical frequency of modulation is different in each direction. These separated modulation frequencies will contain harmonics for which the amplitude of the odd and even parts contain the interference phase. Therefore, lock-in demodulation can determine interferometric phase in each direction from a single photodetector measurement. Interference occurs within the probe head which is 5 mm diameter and 40 mm long.

Based on reviews of the published literature on fiber-based surface measuring probes only the paper of (M Schulz and P Lehmann, 2013) uses mechanical modulation at the tip of the probe. There have been no published studies that utilize beam splitters, and multi-directional and multi-modulation frequency scanning.

This probe has the potential for further miniaturization and because it comprises minimal optical components it can be manufactured at a low cost. Other attributes of this probe include Fabry Perot quadrature, short optical path, common path, a common reference mirror, and full quadrature detection on all axes can be measured using a single detector.

CHAPTER 2 PRINCIPLE OF OPERATION MODULATION INTERFEROMETRY

2-1 MODULATION SYSTEMS

In this chapter an overview of different modulating systems including acoustic and mechanical methods of modulation is being discussed.

2-1-1 PREVIOUS USED IN THE INSTRUMENTATION DEVELOPMENT LABORATORY: AOM AND EXTERNAL MIRROR

2-1-1-1 AOM MODULATION

To evaluate the performance of a modulated source measurement system a Michelson interferometry setup was designed and fabricated. This system included a laser diode (current controlled using a Thorlabs driver), an Acousto Optic Modulator (AOM), a Pinhole (slit) to extract one of the diffracted beams and a Michelson Interferometry setup that is consist of a beam splitter, a fixed mirror, and a moving mirror. The moving mirror was controlled using a piezo electric actuator flexure stage moving sinusoidally back and forth along the beam axis. Interference of reflected light from the fixed mirror and moving mirror, occurs at the beam splitter and is transmitted to the photodetector. The interference signal from the photodetector was processed using two lock-in amplifiers to extract harmonics and the LabVIEW phase unwrapping program to convert the measured signal to mirror displacement. In Figure 22 a picture of the setup for current driving unit including an optical isolator, a beam splitter to get feedback from a photodetector and the Thorlabs current driver module is shown. Also, a schematic of the Michelson Interferometer stage is illustrated in Figure 22.

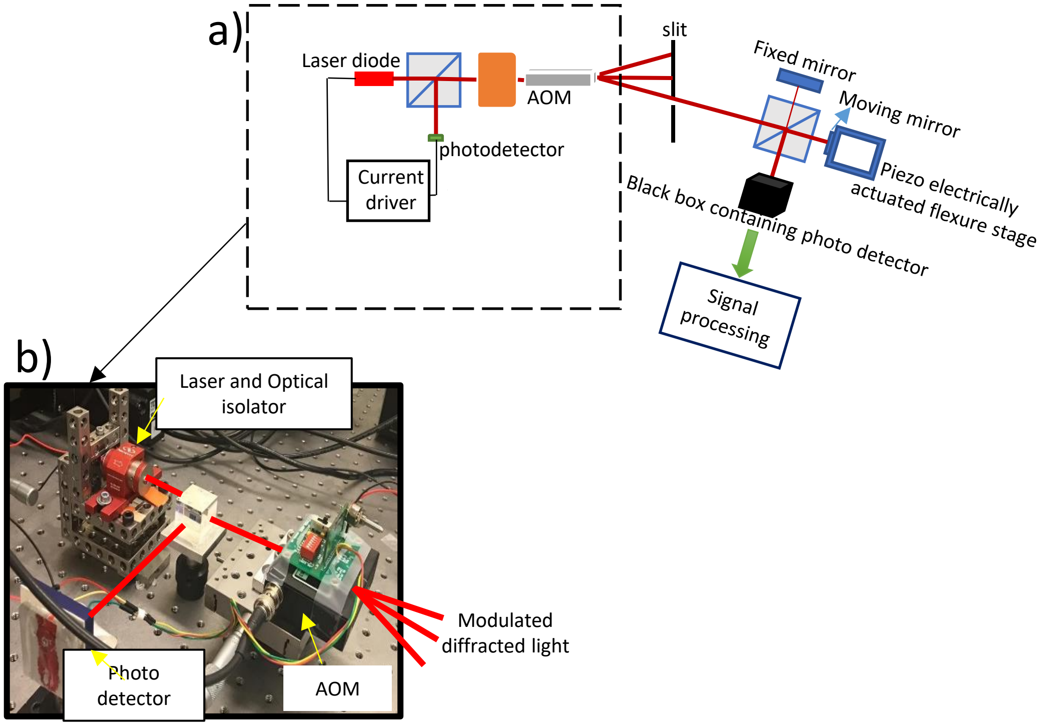

Figure 22 Michelson Interferometer using Acousto Optic Modulator a) schematic diagram indicating major system components, b) photograph of the assembled apparatus.

An AOM operates by applying a sinusoidal signal to a piezoelectric actuator that is bonded onto a piece of crystal. The motion of the actuator transmits a force to the AOM crystal resulting in stress waves that propagate through it. These periodic travelling stress waves induce a corresponding periodic variation in the refraction in the crystal that then acts as a grating to the light passing through it. As the result, the transmitted light diffracts at the output of AOM and splits into several beams forming a diffraction pattern. Any of these beams except the zero order, is modulated and contains the harmonics that can be extracted using the frequency of the modulation applied to the AOM crystal.

Figure 23 shows a preliminary result of measuring displacement of a mirror mounted on a piezo electric flexure stage. The operating frequency for the AOM in this experiment was 60 MHz and this 60

MHz signal was modulated at 300 kHz (Arablu and Smith, 2018). Displacement of 3.7 μm for the moving mirror was measured.

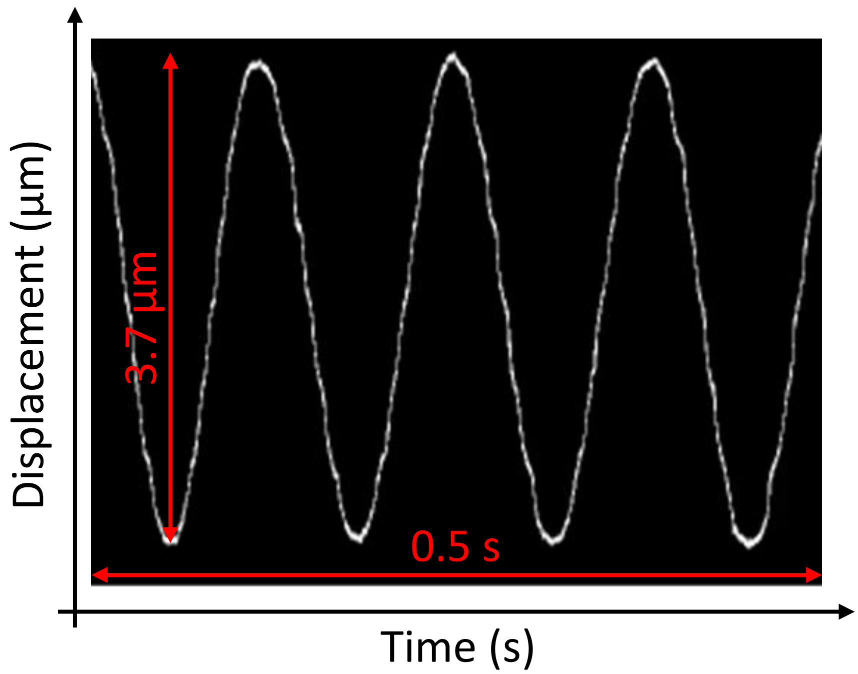

Figure 23. displacement measurement of a moving mirror using AOM modulation technique.

2-1-1-2 MECHANICAL MODULATION

2-1-1-2-1 MICHELSON INTERFEROMETER MEASUREMENT SYSTEM USING MECHANICAL MODULATION

After measuring the displacement of the moving mirror mounted on a piezo electric actuator flexure stage, the next step was replacing AOM with mechanical modulation method using an external mirror (the fixed mirror in the previous experiment) moving back and forth on the axis of the beam to provide the frequency of modulation.

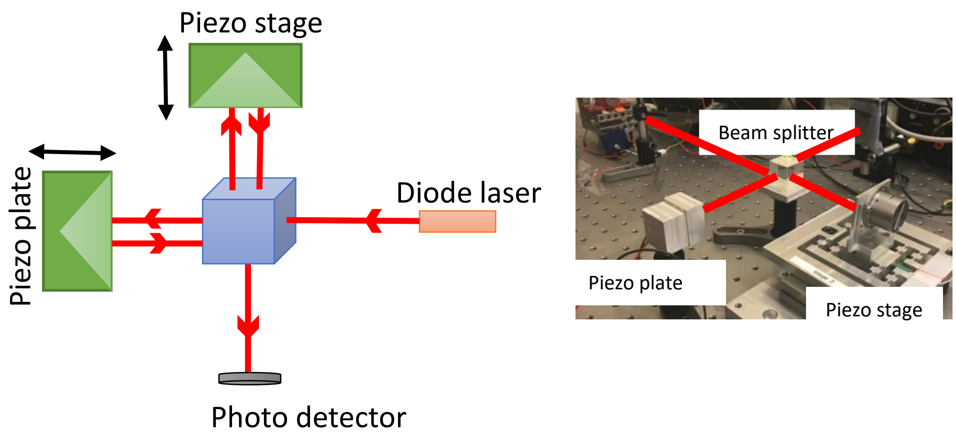

Figure 24. schematic and photograph of a Michelson Interferometry setup with mechanical modulation method

In this method, displacement of a mirror mounted on a piezo electric actuator flexure is being measured and the other beam is reflected back from a mirror mounted on a piezo electric plate stage moving at the applied modulation frequency. See Figure 24.

Figure 25 shows the result of displacement measurement of the moving mirror displacing sinusoidally with a peak to valley displacement of 3.7 µm and using a modulation frequency of 40 kHz.

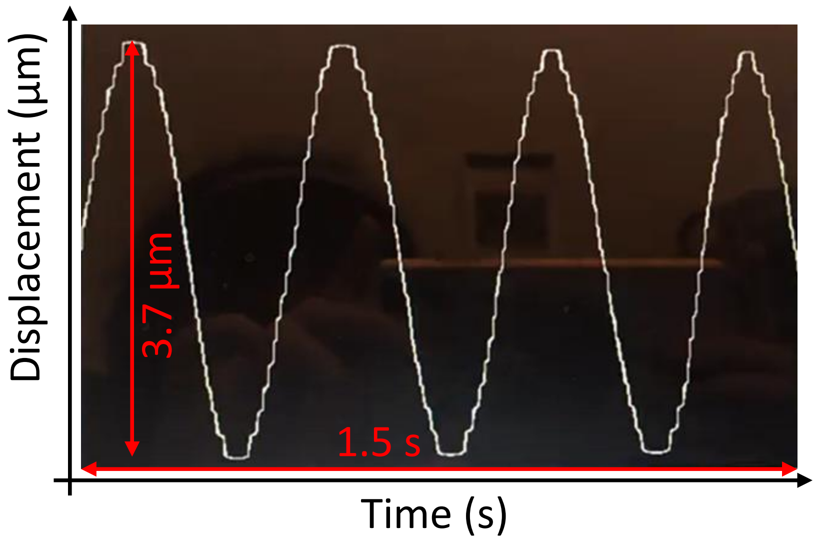

Figure 25. preliminary result for displacement measurement of a moving mirror using mechanical modulation technique.

2-1-1-2-2 FABRY-PEROT FIBER-BASED INTERFEROMETRY SYSTEM USING MECHANICAL MODULATION METHOD

After measuring the displacement of moving mirror using mechanically modulation of the light successfully, the last step was to create a prototype a fiber-based system with optical phase measurement based on Fabry Perot interferometry.

For the purpose of mechanically modulating the light at the fiber tip and coupling this back into the fiber successfully, a piezo electric flexure stage including a fiber holder part was designed and fabricated. The schematic of the whole system including signal conditioning units is illustrated in Figure 26.

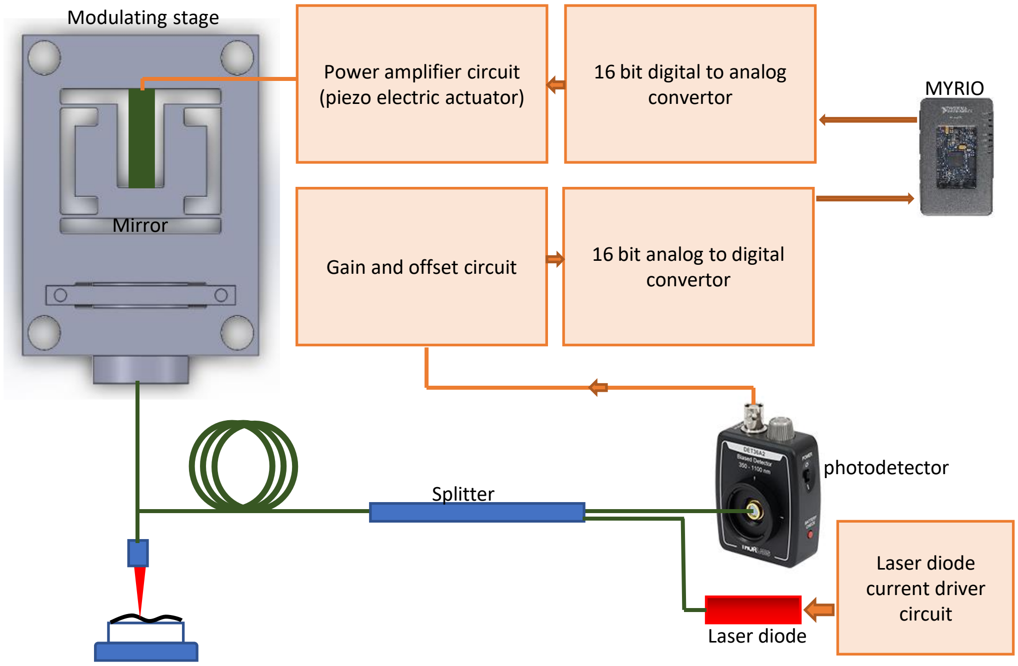

Figure 26. Schematic of fiber-based probe system using mechanical modulation of light.

The result of measurements for measuring displacement of a moving mirror using Fabry-Perot interferometry and mechanical modulation technique is presented in Figure 27. In this measurement the modulation frequency was 9 kHz, and the mirror displacement is 2 μm. There is some issue regarding the quadrature extraction in this experiment. In the process of extract of phase, it is necessary to normalize the amplitude of harmonics, offset removal, synchronization of sampling, and real-time data processing. The purpose of this experiment is to demonstrate phase extraction within the FPGA real-time system and eliminate the laboratory lock-in amplifiers, so the probe can operate as a stand-alone system. Resolution of these multiple issues resulted in the elimination of this characteristic.

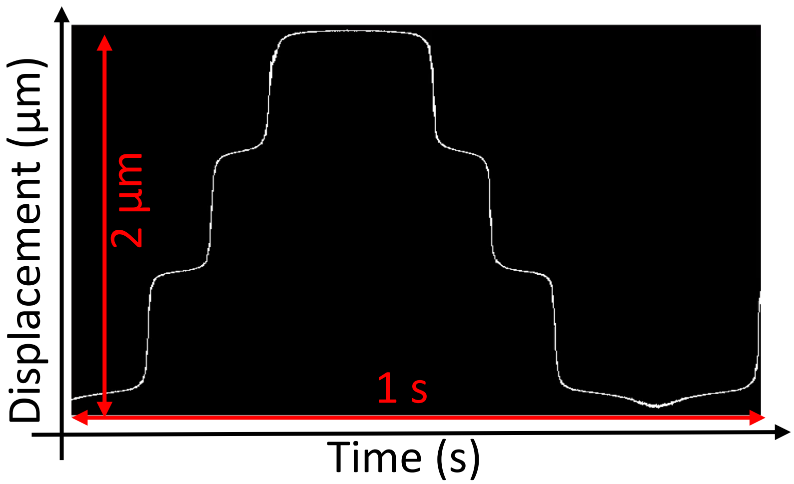

Figure 27. the preliminary result for displacement measurement of a moving mirror using mechanical modulation technique and fiber based Fabry Perot interferometry

2-1-2 METHODS USED IN THIS THESIS: DIRECT PROBE MODULATION

For the major probe development of this thesis the modulation happens at the surface of measurement as shown in Figure 28. The advantage of this approach is that it eliminates the phase shift and distortions from stray reflections as the light travels through the fiber. This reduces the errors substantially and also enables the creation of a more compact system. Two probes have been created; one optical probe is designed to modulate vertically for a simple one directional probe and the second probe is simultaneously oscillated vertically and horizontally using a tube piezo electric actuator to create a bi-directional probe.

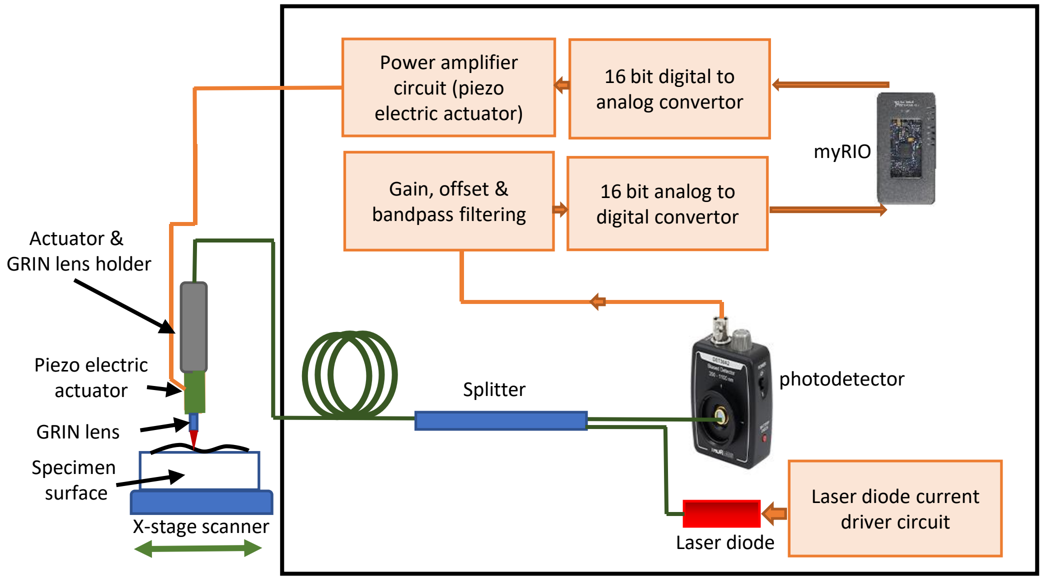

Figure 28. Schematic of direct probe modulation system.

The piezoelectric actuator tube is capable of moving in 3 orthogonal axes of x, y, and z simultaneously by applying the appropriate voltages to different plates on the outer and inner electrodes. As shown in Figure 29, in order to actuate it simultaneously in one horizontal axis and the vertical axis, a voltage signal of frequency content ω_1+ω_2 is applied to +X and -Y plates and also ω_1-ω_2 is applied to the -X and +Y plates. Doing this, the tube actuates with frequency ω_2 on the horizontal axis direction and with frequency ω_1 on the vertical axis. Chapters 3 through 6 present the design, manufacture, performance testing, and surface measurements results of these probes.

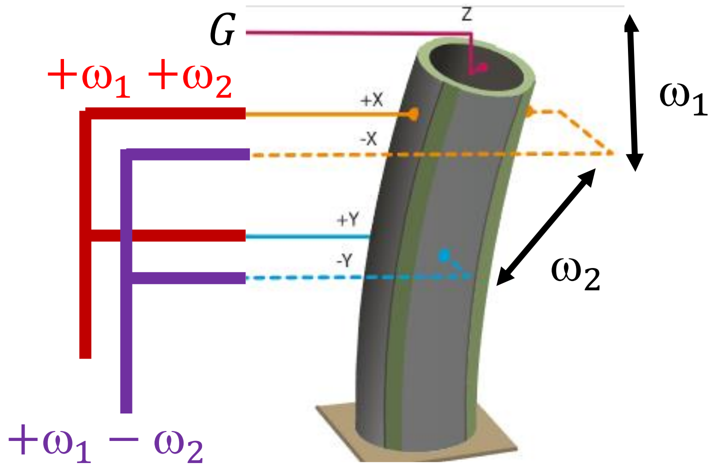

Figure 29. Piezo electric actuator tube

CHAPTER 3 FIBER-BASED PROBE DESIGN AND IMPLEMENTATION

An optical model of fiber to grin lens coupling and Fabry Perot interference of the focused beam is first discussed. After that theoretical model are presented for simple interference, modulated signal, Fourier transformation, and phase unwrapping methods used for digital signal processing presented. The final section details a two directional Fabry Perot interferometry system and the two directional modulation and demodulation process.

3-1 OPTICAL MODELS

3-1-1 FIBER TO GRIN LENS COUPLING OPTICAL MODEL

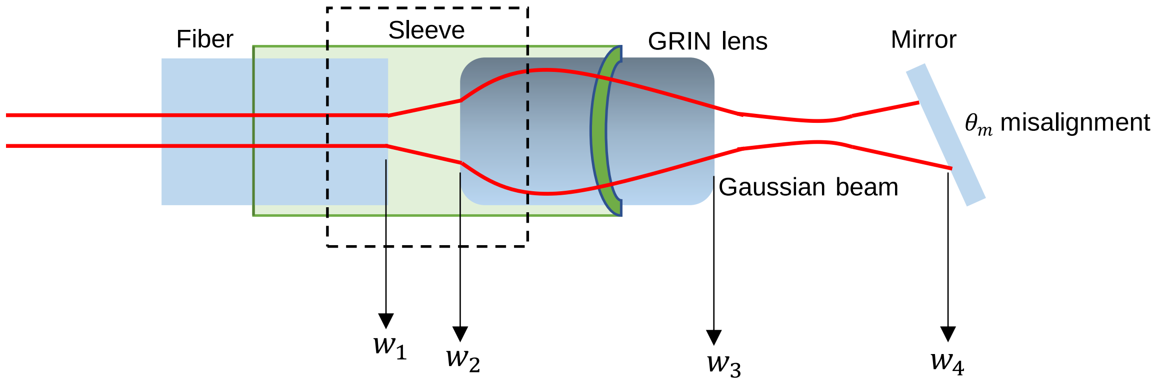

Figure 30 Fiber to GRIN lens coupling optical model

Three components are used for coupling the light to a GRIN lens and selecting the focal length; a pigtail ferrule optical fiber, a Grin lens, and a sleeve to hold them parallel relative to each other. If the fiber ferrule and the GRIN lens have contact inside the sleeve the output beam from the GRIN lens will be collimated. For focusing the beam onto a certain spot, it needs to keep the GRIN lens and the fiber ferule within a certain distance and with changing this gap it is possible to adjust the focal length of the lens.

For modeling the process, the beam propagation in divided into four stages and the beam size at the end of each stage is illustrated as w_1, w_2, w_3 and w_4.

The GRIN lens refractive index n(r) is the largest along the longitudinal axis and decreases quadratically with radial distance [Robert W. Gilsdorf and Joseph C. Palais, 1994]:

$$n(r) = n_0 \left(1 - \frac{Ar^2}{2}\right) \qquad \text{3-1}$$

where n_0 is the refractive index of the GRIN lens at the central axis (1.66), A [mm^{-1}] is the gradient constant (0.724 mm^{-1}) and r [mm] is the radius of the GRIN lens (0.9 mm).

When a beam propagates through the GRIN lens, the angle and position of the output ray change can be predicted as a matrix shown in equation (3-2).

$$\begin{pmatrix} r_2 \\ \theta_2 \end{pmatrix} = \begin{pmatrix} \cos\sqrt{A}z & \frac{1}{n_0\sqrt{A}}\sin\sqrt{A}z \\ -n_0\sqrt{A}\sin\sqrt{A}z & \cos\sqrt{A}z \end{pmatrix}\begin{pmatrix} r_1 \\ \theta_1 \end{pmatrix} \qquad \text{3-2}$$

where r_1 and θ_1 are the input position and input angle of the ray, r_2 and θ_2 are the output position and output angle of the ray and z is the length of the GRIN lens.

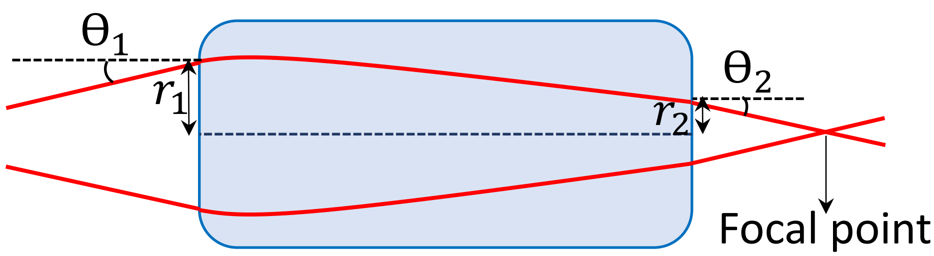

Figure 31. A diagram of GRIN lens functionality

At stage one the angle of the ray is equal to the numerical aperture of the fiber ferule NA and the beam size is equal to the diameter of fiber w_1.

At stage two the beam propagates as a gaussian beam over the distance between the fiber ferule and the GRIN lens. See equation (3-3).

$$w_2(z) = w_1\left[1 + \left(\frac{\lambda d}{\pi n_a {w_1}^2}\right)^2\right]^{1/2} \qquad \text{3-3}$$

In this equation w_2 is the beam size at the entrance of the GRIN lens, w_1 is the size of the fiber, d is the separation between fiber ferule and GRIN lens, n_a is the refractive index of air (1) and λ is the light source wavelength (633 nm). Figure 32 shows the plot for gaussian beam propagation over the distance between the fiber ferule and the GRIN lens.

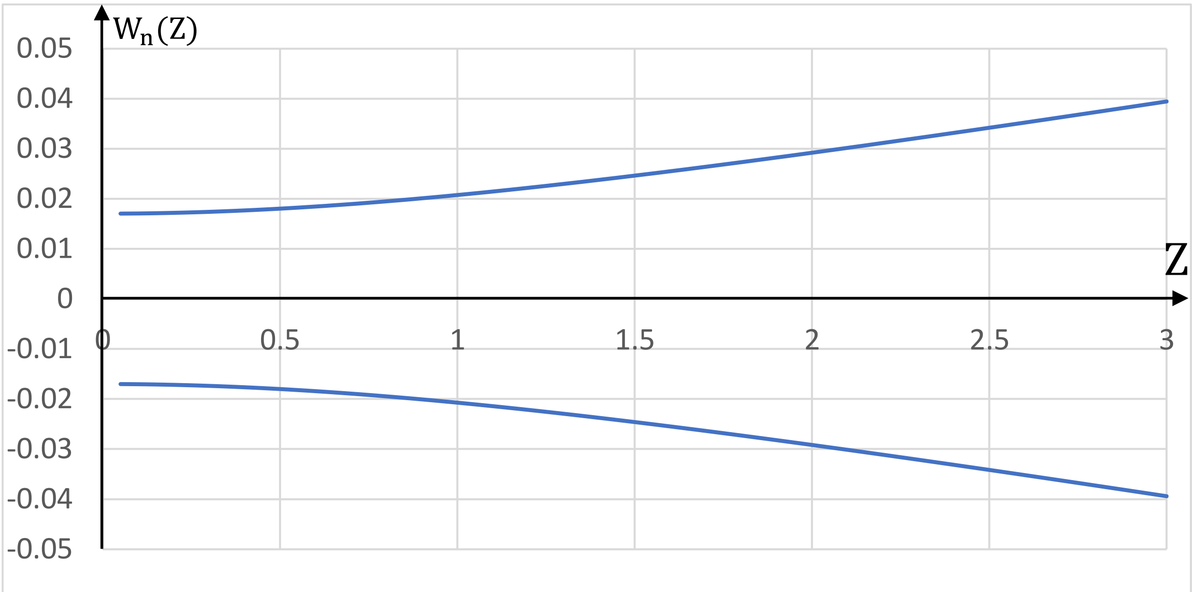

Figure 32. Gaussian beam propagation over the distance between the fiber ferule and the GRIN lens.

At stage three light has propagated through the Grin lens and having one quarter-pitch GRIN lens, the angle and position of rays is shown in equation (3-4) and (3-5).

$$r_2 = \frac{NA}{n_0\sqrt{A}} \tag{3-4}$$

$$\theta_2 = -n_0\sqrt{A}\ w_2(z) \tag{3-5}$$

After the calculations and considering the numbers and constants for this experiment, r_2 is equal to 0.52 mm.

At stage four the light propagates as a gaussian beam and the beam size at the mirror is shown in equation (3-6).

$$w_4(z) = w_0\left[1 + \left(\frac{\lambda z}{\pi n_a {w_0}^2}\right)^2\right]^{1/2} \tag{3-6}$$

where z here is the length of Fabry Perot cavity. Figure 33 shows the gaussian beam propagation over the distance after the GRIN lens.

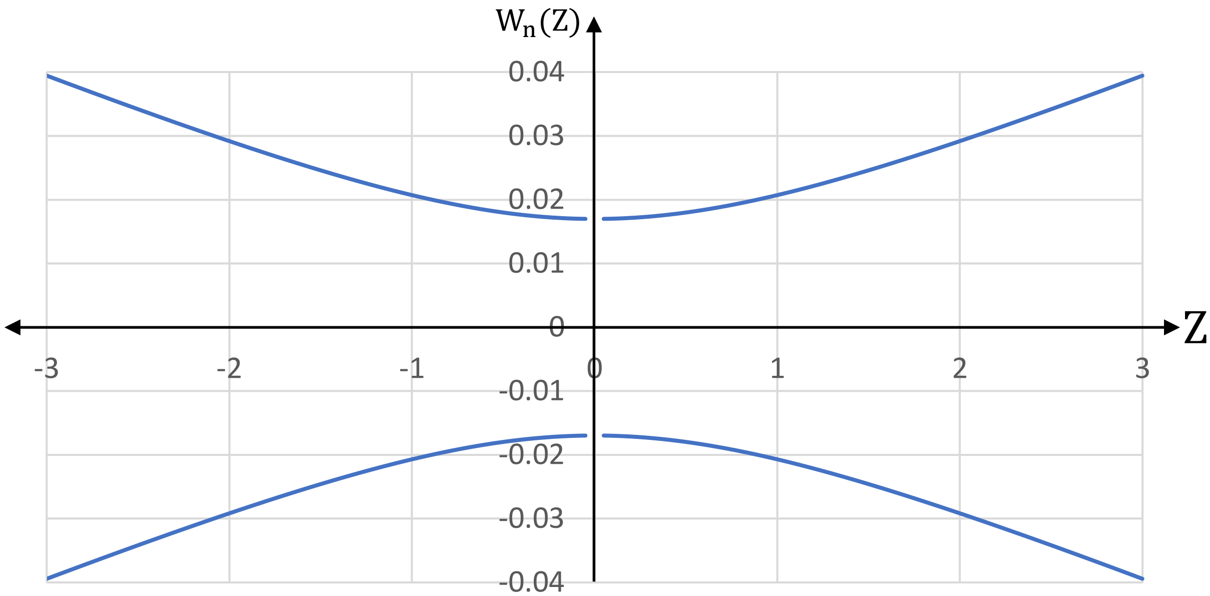

Figure 33. Gaussian beam propagation over the distance after the GRIN lens.

Figure 34 is a picture of the pigtailed fiber ferule and the GRIN lens, assembling using a glass sleeve.

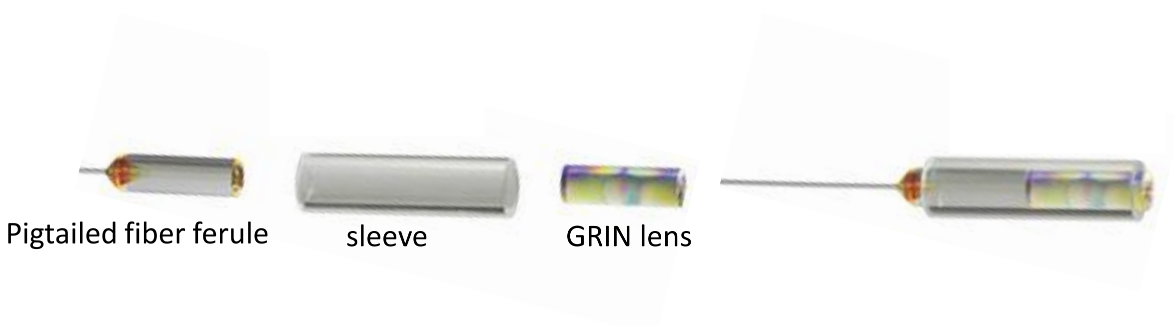

Figure 34 pigtail ferule and GRIN lens before and after assembly (Thorlabs)

3-1-2 FABRY PEROT INTERFERENCE

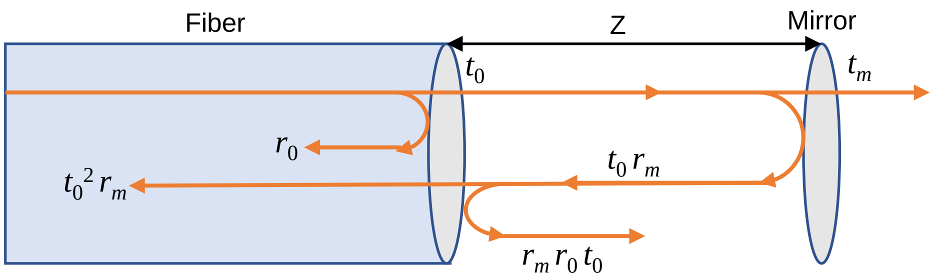

Figure 35 Fabry Perot fiber-mirror multiple reflections

Wilkinson and Pratt (2011) have presented a Fabry Perot cavity model considering n times reflections and transmissions to calculate the phase and intensity of the light reflected from a Fiber mirror external cavity. From this model, the field reflected back into the fiber is given by equation (3-7).

$$r = r_0 C_0 + \frac{t_0^2}{r_0} \sum_{n=1}^{\infty} (r_m r_0)^n C_n e^{-i\pi} \qquad \text{3-7}$$

$$r = a(z_R, \theta_m) + ib(z_R, \theta_m) \qquad \text{3-8}$$

$$\varphi = \tan^{-1} \frac{b}{a} \qquad \text{3-9}$$

$$r^2 = a^2 + b^2 \qquad \text{3-10}$$

where r_0 and t_0 are respectively reflection and transmission coefficients from fiber surface and r_m and t_m are respectively reflection and transmission coefficients from mirror surface. φ is the phase and r^2 is the amplitude of the signal.

This model defines C_n coupling coefficient that includes the influence of misalignment (θ_m) between the fiber end face and external mirror, and Gouy effect of beam focusing using a GRIN lens if an approximately Gaussian beam profile (z_R is the Rayleigh length) is assumed, given by

$$C_n = \Delta_n e^{i\beta_n} e^{i\Theta_n} \qquad 3\text{-}11$$

where, C_n is fiber-mirror coupling coeficient in equation (3-11), Δ_n is diffraction coeficient in equation (3-12), Θ_n is Gouy phase and misalinment coeficient in equation (3-13), and β_n is optical phase shilft coeficient in equation (3-14).

$$\Delta_n = \frac{1}{\sqrt{1+n^2\left(\frac{z}{z_R}\right)^2}} e^{-\left[\frac{kz_R\left(1+5n^2\left(\frac{z}{z_R}\right)^2\right)}{1+n^2\left(\frac{z}{z_R}\right)^2} n^2 {\theta_m}^2\right]} \qquad 3\text{-}12$$

$$\Theta_n = -\tan^{-1}\left(n\frac{z}{z_R}\right) + \frac{kz_R\left(3n\frac{z}{z_R} - n^3\left(\frac{z}{z_R}\right)^3\right)}{1+n^2\left(\frac{z}{z_R}\right)^2} n^2 {\theta_m}^2 \qquad 3\text{-}13$$

$$\beta_n = 2nkz \qquad 3\text{-}14$$

In these equations, $k = \frac{2\pi n}{\lambda}$ is the wave number and n is the refractive index of the material between fiber and mirror. z is the separation of cavity.

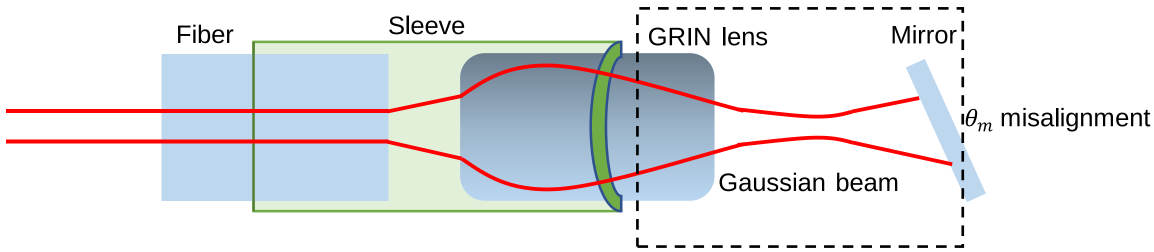

Figure 36 Fabry Perot cavity considering misalignment, Gouy phase shift, diffraction, and optical path phase shift

All the parameters presented in this chapter and the multiple coefficient reflections are negligible compared to the first reflection from mirror and the fiber surface. As a consequence, the fiber Fabry Perot interference can be simplify to a simple interference with only considering the optical path phase shift and the first reflections from each surface.

3-2 THEORY

The fiber based profilometer presented in this thesis is working based on interference of light to measure the displacement of surface. The displacement can be extracted from the interference of two beams from a reference source and object source with an optical path length difference. Phase ambiguity has been the main issue in all interferometry techniques and has led to the creation of different methods for phase unwrapping during the years. Modulation technique is one of these methods that works based on coding and decoding of the signal. In this chapter the theory of light interference, mechanical modulation (coding), Fourier transform, and phase unwrapping (decoding) is discussed.

3-2-1 SIMPLE INTERFERENCE

In fiber based Fabry Perot interference, the interference happens between the reflected light from the fiber surface and the reflection of the sampled surface that couples back into the same fiber. the light reflects from surface of the fiber acts as the reference beam and the reflection from the sample surface is the object beam. These two beams have an optical path difference because of traveling the light between fiber surface and sample surface. If the gap between these two surfaces changes (because of displacement of the sample surface or having roughness on the profile of the sample surface), an interference signal forms from constructive and destructive integration of the two beams. Equations (3-15) and (3-16) are showing the oscillation of the electric fields of the reference signal and the sample surface signal respectively. A φ_0 phase difference is added to signal $u_2(t)$ phase, because of the gap that sampled surface beam travels between the fiber surface and the sample surface. In these equations, the E_0 is the amplitude of the original lights electric field and w_0 is the frequency of the light.

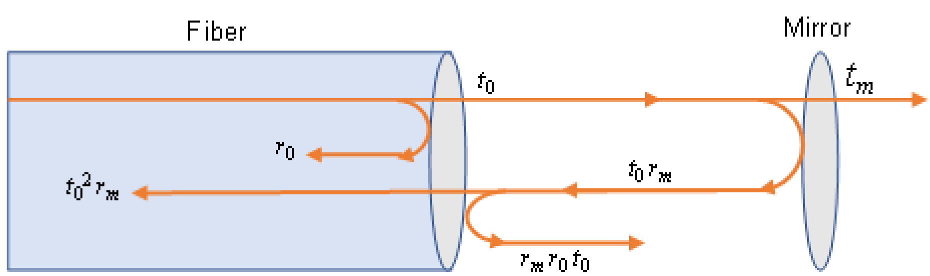

Figure 37 one directional Fabry Perot cavity

$$E_1(t) = \frac{E_0}{2}\sin(w_0 t) \quad 3\text{-}15$$

$$E_2(t) = \frac{E_0}{2}\sin(w_0 t + \varphi_0) \quad 3\text{-}16$$

where

$$\varphi_0 = 2\pi \frac{\Delta L}{\lambda} \quad 3\text{-}17$$

The interference signal can be obtained by adding both electric fields and the intensity of the detected pattern is the square of this equation as shown in equation (3-18).

$$I(t) = [u_1(t) + u_2(t)]^2 = \frac{{E_0}^2}{4}[\sin(w_0 t)^2 + \sin(w_0 t + \varphi_0)^2 + 2\sin(w_0 t)\sin(w_0 t + \varphi_0)] =$$

$$\frac{{E_0}^2}{4}\left[\left(\frac{e^{2iw_0 t} - e^{-2iw_0 t}}{2i}\right)^2 + \left(\frac{e^{2i(w_0 t+\varphi_0)} - e^{-2i(w_0 t+\varphi_0)}}{2i}\right)^2 + 2\left(\frac{e^{2iw_0 t} - e^{-2iw_0 t}}{2i}\right)\left(\frac{e^{2i(w_0 t+\varphi_0)} - e^{-2i(w_0 t+\varphi_0)}}{2i}\right)\right] =$$

$$\frac{{E_0}^2}{16}\begin{bmatrix} -e^{4iw_0 t} - e^{-4iw_0 t} + 2 - e^{4iw_0 t}e^{4i\varphi_0} - e^{-4iw_0 t}e^{-4i\varphi_0} \\ +2 - 2\left(e^{2iw_0 t} - e^{-2iw_0 t}\right)\left(e^{2iw_0 t}e^{2i\varphi_0} - e^{-2iw_0 t}e^{-2i\varphi_0}\right) \end{bmatrix} \qquad \text{3-18}$$

$w_0 \cong 10^{15}$ is the laser light carrier frequency and is too big and too fast to be measured. With considering that, all $e^{\pm w_0}$ terms are eliminated, and the intensity equation is as equation (3-21).

$$I(t) = \frac{{E_0}^2}{16}\left[4 + e^{2i\varphi_0} + e^{-2i\varphi_0}\right] \qquad \text{3-20}$$

$$I(t) = \frac{{E_0}^2}{4}(1 + \cos\varphi_0) \qquad \text{3-21}$$

When the phase difference between the reference beam and the sample surface beam φ_0 varies between zero π periodically over time, the intensity of the detected interference follows a pattern as showed in 36.

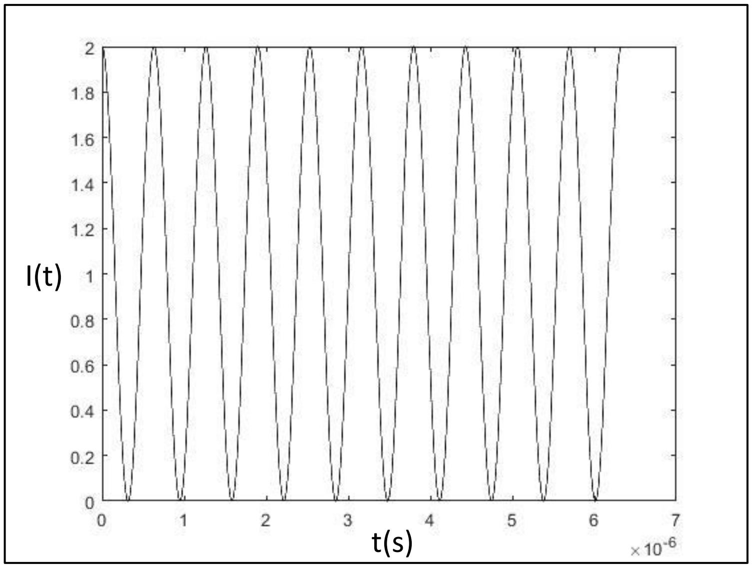

Figure 38. Interference of a beam reflected from reference surface and a beam reflected from a sample surface that has a varying phase difference with the reference beam.

3-2-2 MODULATION

When modulation is added to the system, the reference surface also oscillates with the frequency of modulation, and this adds a sinusoidal term to the phase difference between the reference beam and the sample surface beam. By adding this term, the electric field for reference beam and sample surface beam varies as equation (3-22) and (3-23) respectively, over time.

$$E_1(t) = \frac{E_0}{2}\sin(w_0 t + Bsinw_m t) \quad \text{3-22}$$

$$E_2(t) = \frac{E_0}{2}\sin(w_0 t + \varphi_0) \quad \text{3-23}$$

In these equations w_m is the frequency of modulation (reference surface oscillation frequency) and B is the amplitude of this oscillation. The intensity of the detected interference of these two beams is as equation (3-25).

$$I(t) = [u_1(t) + u_2(t)]^2$$

$$= \frac{{E_0}^2}{4}[\sin(w_0t + Bsinw_mt)^2 + \sin(w_0t + \varphi_0)^2$$

$$+ 2\sin(w_0t + Bsinw_mt)\sin(w_0t + \varphi_0)] =$$

$$\frac{{E_0}^2}{4}\left[\left(\frac{e^{2i(w_0t+Bsinw_mt)} - e^{-2i(w_0t+Bsinw_mt)}}{2i}\right)^2 + \left(\frac{e^{2i(w_0t+\varphi_0)} - e^{-2i(w_0t+\varphi_0)}}{2i}\right)^2\right.$$

$$\left.+ 2\left(\frac{e^{2i(w_0t+Bsinw_mt)} - e^{-2i(w_0t+Bsinw_mt)}}{2i}\right)\left(\frac{e^{2i(w_0t+\varphi_0)} - e^{-2i(w_0t+\varphi_0)}}{2i}\right)\right] =$$

$$\frac{{E_0}^2}{16}\begin{bmatrix} -e^{4i(w_0t+Bsinw_mt)} - e^{-4i(w_0t+Bsinw_mt)} + 2 - e^{4iw_0t}e^{4i\varphi_0} - e^{-4iw_0t}e^{-4i\varphi_0} \\ +2 - 2\left(e^{2i(w_0t+Bsinw_mt)} - e^{-2i(w_0t+Bsinw_mt)}\right)\left(e^{2iw_0t}e^{2i\varphi_0} - e^{-2iw_0t}e^{-2i\varphi_0}\right) \end{bmatrix} \quad 3\text{-}24$$

Again $w_0 \cong 10^{15}$ is the laser light carrier frequency and is too big and too fast to be measured. With considering that, all $e^{\pm w_0}$ terms are eliminated.

$$I(t) = \frac{{E_0}^2}{16}\left[4 + e^{2i(\varphi_0+Bsinw_mt)} + e^{-2i(\varphi_0+Bsinw_mt)}\right]$$

$$I(t) = \frac{{E_0}^2}{4}(1 + \cos(\varphi_0 + B\sin(w_mt))) \quad 3\text{-}25$$

After expansion of the equation (3-25)

$$I(t) = \frac{{E_0}^2}{4}(1 + \cos(\varphi_0)\cos(B\sin(w_mt)) - \sin(\varphi_0)\sin(B\sin(w_mt))) \quad 3\text{-}26$$

And using Jacobi-Anger expansion for $\cos(B\sin(w_mt))$ and $\sin(B\sin(w_mt))$,

$$\cos(B\sin(w_mt)) = J_0(B) + 2\sum_{n=1}^{\infty} J_{2n}(B)\cos(2nw_mt) \quad 3\text{-}27$$

$$\sin(B\sin(w_mt)) = 2\sum_{n=1}^{\infty} J_{2n-1}(B)\sin((2n{-}1)w_mt) \quad 3\text{-}28$$

In these equations $J_\alpha(x)$ is The Bessel function of order α. Here only the Bessel function of the first kind (positive integer values of x) is considered. See equation (3-29).

$$J_\alpha(x) = \sum_{m=0}^{\infty} \frac{(-1)^m}{m!\Gamma(m+\alpha+1)} \left(\frac{x}{2}\right)^{2m+\alpha} \qquad 3\text{-}29$$

And in this equation

$$\Gamma(n) = (n-1)! \qquad 3\text{-}30$$

is the gamma function.

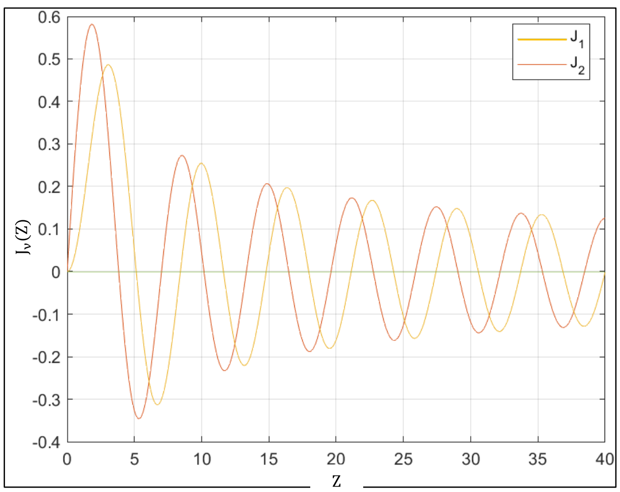

Figure 39. Bessel functions of first and second kind

Figure 39 shows the Bessel functions of the first and second kind. Substituting everything in the original intensity function gives us equation (3-31).

$$I(t) = \frac{{E_0}^2}{4}\Big(1 + \cos(\varphi_0)\big(J_0(B) + 2\sum_{n=1}^{\infty} J_{2n}(B)\cos(2nw_m t)\big) -$$

$$\sin(\varphi_0)\left(2\sum_{n=1}^{\infty} J_{2n-1}(B)\sin((2n-1)w_m t)\right)\Big) \qquad 3\text{-}31$$

3-2-3 SIGNAL PROCESSING

For extracting the amplitudes of odd and even function harmonics in the interference signal, the Fourier transform technique is being used. Fourier series are a series of periodic functions of sin and cos of multiple harmonics (n harmonics) and they are a good method for extracting coefficients of any periodic orthogonal function like Bessel functions.

3-2-3-1 FOURIER SERIES

Fourier series are a series of periodic orthogonal functions. $f(x)$ is one example of a periodic function that its period length is L. See equation (3-32).

$$f(x) = a_0 + \sum_{n=1}^{\infty} a_n \cos nx + b_n \sin nx \qquad \text{3-32}$$

The coefficients of $f(x)$ is defined in equations (3-33) – (3-35).

$$a_0 = \frac{1}{4L} \sum_{n=1}^{L} f(x) \qquad \text{3-33}$$

$$a_n = \frac{1}{2L} \sum_{n=1}^{L} f(x) \cos nx \qquad \text{3-34}$$

$$b_n = \frac{1}{2L} \sum_{n=1}^{L} f(x) \sin nx \qquad \text{3-35}$$

According to this and the fact that our intensity function is a periodic function consisting of orthogonal sin and cos functions we can extract the coefficients of sin and cos functions using Fourier series (simply multiplying these functions will give us the coefficients of each function). Equation (3-36) is our modulated intensity signal detected from the interference of two beams.

$$I(t) = \frac{{E_0}^2}{4} + \frac{{E_0}^2}{4} \cos(\varphi_0) J_0(B) + \frac{{E_0}^2}{2} \cos(\varphi_0) \sum_{n=1}^{\infty} J_{2n}(B) \cos(2nw_m t) -$$

$$\frac{{E_0}^2}{2} \sin(\varphi_0) \sum_{n=1}^{\infty} J_{2n-1}(B)\, sin((2n-1) w_m t) \qquad \text{3-36}$$

If we do a 36-bit Fourier transform a 36-bit sin and cos function of modulation frequency will multiply to the intensity function and after averaging, one coefficient will be resulted for each index n i.e.

$$a_n = \frac{1}{72}\sum_{n=1}^{L} I(t)\cos(2nw_m t) \qquad 3\text{-}37$$

$$b_n = \frac{1}{72}\sum_{n=1}^{L} I(t)\sin(2nw_m t) \qquad 3\text{-}38$$

After multiplying and averaging over each period, the a_n and b_n coefficients will be extracted. See equation (3-39) and (3-40).

$$a_n = \frac{{E_0}^2\cos(\varphi_0)}{144} J_{2n}(B) \qquad 3\text{-}39$$

$$b_n = \frac{{E_0}^2\sin(\varphi_0)}{144} J_{2n-1}(B) \qquad 3\text{-}40$$

These are the odd and even coefficients of the Bessel function of first kind and they are orthogonal relative to each other. We call them modulation harmonics. By extracting them using Fourier series it is possible to make a quadrature out of them and unwrap the phase using this quadrature.

3-2-3-2 PHASE UNWRAPPING

After modulating the signal and extracting orthogonal harmonics, a linear motion (and, therefore, phase change) with result in a locus that can be scaled to a circle when two orthogonal harmonics are plotted against each other.

Figure 40 shows the plotted first and second harmonics of a simulated signal on the left and a quadrature drawn using them. This quadrature is a 3D plot with time being the axis into the page.

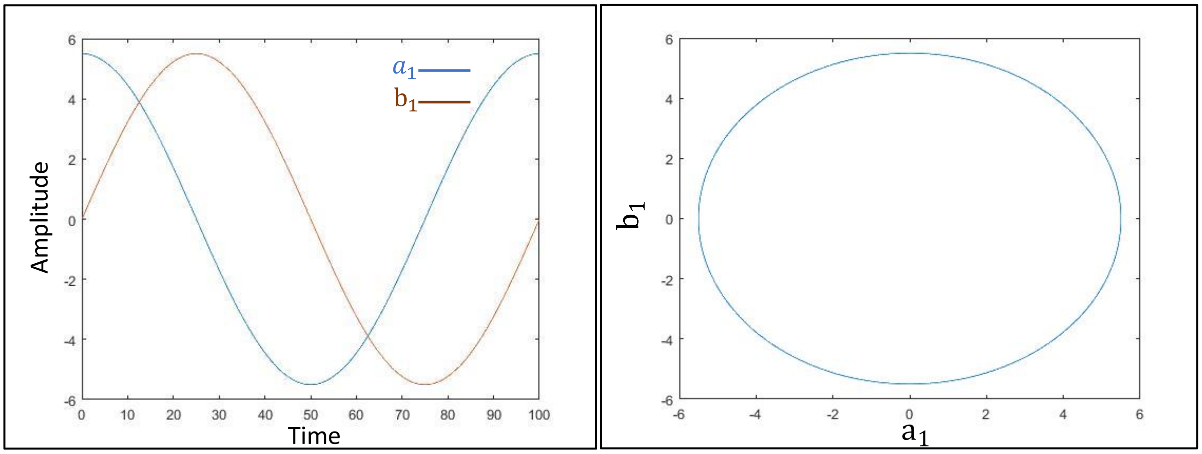

Figure 40. The plotted first and second harmonics of the simulated signal vs time and the quadrature drawn with them. In the real world, a_1 and b_1 are not having same amplitude.

The phase of the quadrature is extracted using equation (3-41).

$$\varphi = \tan^{-1}\frac{first\ harmonic}{second\ harmonic} \qquad 3\text{-}41$$

And displacement can be calculated using the number of quadrature and the direction of moving.

$$\Delta L = \frac{\varphi}{2\pi}\lambda \pm N\lambda \qquad 3\text{-}42$$

Where λ is the wavelength of light and N is the number of the circles. When the circle is forming clockwise λ adds to the equation and when it is counterclockwise λ subtracts from the equation. This way depending on which way the sample surface is moving, the phase increments or decrements and the correct displacement can be calculated.

3-2-4 TWO DIRECTIONAL MEASUREMENTS

When the measurements occur upon two surfaces, the interference happen between tip of GRIN lens reflection and each of the reflected lights from different surfaces as illustrated in Figure 41.

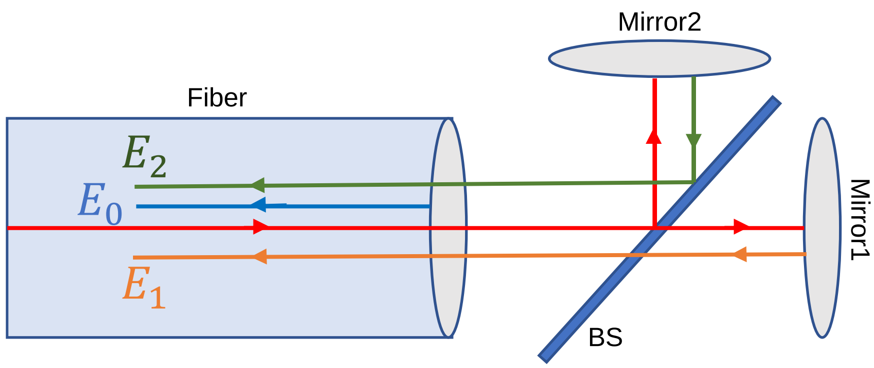

Figure 41 two directional Fabry Perot cavity

The electrical field for the tip of GRIN lens and reflection from each of the surfaces will be as equation (3-43) and (3-44) and (3-45).

$$E_1(t) = \frac{E_0}{2}\sin(w_0 t + \varphi_0) \tag{3-43}$$

$$E_2(t) = \frac{E_0}{4}\sin(w_0 t + \varphi_1) \tag{3-44}$$

$$E_3(t) = \frac{E_0}{4}\sin(w_0 t + \varphi_2) \tag{3-45}$$

where

$$\varphi_0 = 2\pi\frac{\Delta L}{\lambda} \tag{3-46}$$

$$\varphi_1 = 2\pi\frac{\Delta L + L_1}{\lambda} \tag{3-47}$$

$$\varphi_2 = 2\pi\frac{\Delta L + L_2}{\lambda} \tag{3-48}$$

And the intensity of interference signal is as equation (3-50).

$$I(t) = [u_1(t) + u_2(t) + u_3(t)]^2$$

$$= \frac{{E_0}^2}{16}[4\sin(w_0 t)^2 + \sin(w_0 t + \varphi_1)^2 + \sin(w_0 t + \varphi_2)^2$$

$$+ 4\sin(w_0 t)\sin(w_0 t + \varphi_1) + 4\sin(w_0 t)\sin(w_0 t + \varphi_2)$$

$$+ 2\sin(w_0 t + \varphi_1)\sin(w_0 t + \varphi_2)] =$$

$$\frac{{E_0}^2}{16}\left[\begin{array}{c} 4\left(\frac{e^{2iw_0 t} - e^{-2iw_0 t}}{2i}\right)^2 + \left(\frac{e^{2i(w_0 t+\varphi_1)} - e^{-2i(w_0 t+\varphi_1)}}{2i}\right)^2 \\ + \left(\frac{e^{2i(w_0 t+\varphi_2)} - e^{-2i(w_0 t+\varphi_2)}}{2i}\right)^2 \\ +4\left(\frac{e^{2iw_0 t} - e^{-2iw_0 t}}{2i}\right)\left(\frac{e^{2i(w_0 t+\varphi_1)} - e^{-2i(w_0 t+\varphi_1)}}{2i}\right) \\ +4\left(\frac{e^{2iw_0 t} - e^{-2iw_0 t}}{2i}\right)\left(\frac{e^{2i(w_0 t+\varphi_2)} - e^{-2i(w_0 t+\varphi_2)}}{2i}\right) \\ +2\left(\frac{e^{2i(w_0 t+\varphi_1)} - e^{-2i(w_0 t+\varphi_1)}}{2i}\right)\left(\frac{e^{2i(w_0 t+\varphi_2)} - e^{-2i(w_0 t+\varphi_2)}}{2i}\right) \end{array}\right]$$

$$= \frac{{E_0}^2}{64}\left[\begin{array}{c} -4e^{4iw_0 t} - 4e^{-4iw_0 t} + 8 - e^{4iw_0 t}e^{4i\varphi_1} - e^{-4iw_0 t}e^{-4i\varphi_1} \\ +2 - e^{4iw_0 t}e^{4i\varphi_2} - e^{-4iw_0 t}e^{-4i\varphi_2} + 2 \\ -4\left(e^{2iw_0 t} - e^{-2iw_0 t}\right)\left(e^{2iw_0 t}e^{2i\varphi_1} - e^{-2iw_0 t}e^{-2i\varphi_1}\right) \\ -4\left(e^{2iw_0 t} - e^{-2iw_0 t}\right)\left(e^{2iw_0 t}e^{2i\varphi_2} - e^{-2iw_0 t}e^{-2i\varphi_2}\right) \\ -2\left(e^{2iw_0 t}e^{2i\varphi_1} - e^{-2iw_0 t}e^{-2i\varphi_1}\right)\left(e^{2iw_0 t}e^{2i\varphi_2} - e^{-2iw_0 t}e^{-2i\varphi_2}\right) \end{array}\right] =$$

$$I(t) = \frac{{E_0}^2}{64}\left[12 + 4e^{2i\varphi_1} + 4e^{-2i\varphi_1} + 4e^{2i\varphi_2} + 4e^{-2i\varphi_2}e^{2i\varphi_0} + 2e^{-2i(\varphi_2-\varphi_1)} + 2e^{2i(\varphi_2-\varphi_1)}\right] \quad 3\text{-}49$$

$$I(t) = \frac{{E_0}^2}{16}(3 + 2\cos\varphi_1 + 2\cos\varphi_2 + cos((\varphi_2 - \varphi_1)) \quad 3\text{-}50$$

3-2-4-1 MODULATION

After adding modulation in the direction of each measurement (mirror1 and mirror 2) independently, the phase of each beam and the interference intensity changes as:

$$\varphi_0 = 0 \qquad 3\text{-}51$$

$$\varphi_1 = \emptyset_1 + A\sin(w_{m1}t) \qquad 3\text{-}52$$

$$\varphi_2 = \emptyset_2 + B\sin(w_{m2}t) \qquad 3\text{-}53$$

and the intensity of the interference signal is as equation (3-54).

$$I(t) = \frac{{E_0}^2}{16}(3 + 2\cos\varphi_1 + 2\cos\varphi_2 + \cos(\varphi_2 - \varphi_1))$$

$$= \frac{{E_0}^2}{16}(3 + 2\cos(\emptyset_1 + A\sin(w_{m1}t)) + 2\cos(\emptyset_2 + B\sin(w_{m2}t)) + \cos(\emptyset_2 - \emptyset_1 + B\sin(w_{m2}t) - A\sin(w_{m1}t)))$$

$$= \frac{{E_0}^2}{16}(3 + 2\cos(\emptyset_1)\cos(A\sin(w_{m1}t)) - 2\sin(\emptyset_1)\sin(A\sin(w_{m1}t)) + 2\cos(\emptyset_2)\cos(B\sin(w_{m2}t)) - 2\sin(\emptyset_2)\sin(B\sin(w_{m2}t)) + \cos(\emptyset_2 - \emptyset_1)[cos(B\sin(w_{m2}t))\cos(A\sin(w_{m1}t)) + \sin(B\sin(w_{m2}t))\sin(A\sin(w_{m1}t))] - \cos(\emptyset_2 - \emptyset_1)[\cos(B\sin(w_{m2}t))\cos(A\sin(w_{m1}t)) + \sin(B\sin(w_{m2}t))\sin(A\sin(w_{m1}t))]) \qquad 3\text{-}54$$

The Jacobi Anger expansions are presented in equations (3-55) to (3-58).

$$\cos(A\sin(w_{1m}t)) = J_0(A) + 2\sum_{n=1}^{\infty} J_{2n}(A)\cos(2nw_{1m}t) \qquad 3\text{-}55$$

$$\sin(A\sin(w_{1m}t)) = 2\sum_{n=1}^{\infty} J_{2n-1}(A)\sin((2n-1)w_{1m}t) \qquad 3\text{-}56$$

$$\cos(B\sin(w_{2m}t)) = J_0(B) + 2\sum_{n=1}^{\infty} J_{2n}(B)\cos(2nw_{2m}t) \qquad 3\text{-}57$$

$$\sin(B\sin(w_{2m}t)) = 2\sum_{n=1}^{\infty} J_{2n-1}(B)\sin((2n-1)w_{2m}t) \qquad 3\text{-}58$$

using them into the intensity equation will gives us equation (3-59).

$$I(t) = \frac{{E_0}^2}{16}(3 + 2\cos(\emptyset_1)(J_0(A) + 2\sum_{n=1}^{\infty} J_{2n}(A)\cos(2nw_{1m}t)) - 2\sin(\emptyset_1)(2\sum_{n=1}^{\infty} J_{2n-1}(A)\sin((2n-1)w_{1m}t)) + 2\cos(\emptyset_2)(J_0(B) + 2\sum_{n=1}^{\infty} J_{2n}(B)\cos(2nw_{2m}t)) - 2\sin(\emptyset_2)(2\sum_{n=1}^{\infty} J_{2n-1}(B)\sin((2n-1)w_{2m}t)) + \cos(\emptyset_2 - \emptyset_1)[(J_0(B) + 2\sum_{n=1}^{\infty} J_{2n}(B)\cos(2nw_{2m}t))(J_0(A) + 2\sum_{n=1}^{\infty} J_{2n}(A)\cos(2nw_{1m}t))] + \cos(\emptyset_2 - \emptyset_1)[(2\sum_{n=1}^{\infty} J_{2n-1}(B)\sin((2n-1)w_{2m}t))(2\sum_{n=1}^{\infty} J_{2n-1}(A)\sin((2n-1)w_{1m}t))]) \qquad 3\text{-}59$$

and for n=1,2 equation (3-60) is obtained.

$$I(t) = \frac{{E_0}^2}{16}(3 + 2\cos(\emptyset_1)(J_0(A) + 2J_2(A)\cos(2w_{1m}t) + 2J_4(A)\cos(4w_{1m}t) - 2\sin(\emptyset_1)(2J_1(A)\sin(w_{1m}t) + 2J_3(A)\sin(3w_{1m}t)) + 2\cos(\emptyset_2)(J_0(B) + 2J_2(B)\cos(2w_{2m}t) + 2J_4(B)\cos(4w_{2m}t)) - 2\sin(\emptyset_2)(2J_1(B)\sin(w_{2m}t) + 2J_3(B)\sin(3w_{2m}t)) + \cos(\emptyset_2 - \emptyset_1)[(J_0(B) + 2J_2(B)\cos(2w_{2m}t) + 2J_4(B)\cos(4w_{2m}t)(J_0(A) + 2J_2(A)\cos(2w_{1m}t) + 2J_4(A)\cos(4w_{1m}t)))] + \cos(\emptyset_2 - \emptyset_1)[(2J_1(B)\sin(w_{2m}t) + 2J_3(B)\sin(3w_{2m}t))](2J_1(A)\sin(w_{1m}t) + 2J_3(A)\sin(3w_{1m}t))] \qquad 3\text{-}60$$

Considering only the first and second harmonics and eliminating the interference between reflections of two mirrors (the light reflected from mirror 1 interfered with the light reflected from mirror 2 is eliminated using optical filtering methods described later in this thesis), will represents equations (3-61) to (3-64) for harmonics 1 and 2 and for measurements of each mirror intensity interference separately.

$$I(t)_{w1m1} = \frac{{E_0}^2}{16}(-2\sin(\emptyset_1)(2J_1(A)\sin(w_{1m}t)) \qquad 3\text{-}61$$

$$I(t)_{w1m2} = \frac{{E_0}^2}{16}(2\cos((\emptyset_1)(J_0(A) + 2J_2(A)\cos(2w_{1m}t))) \qquad 3\text{-}62$$

$$I(t)_{w2m1} = \frac{{E_0}^2}{16}(-2\sin(\emptyset_2)(2J_1(B)\sin(w_{2m}t))) \qquad 3\text{-}63$$

$$I(t)_{w2m2} = \frac{{E_0}^2}{16}(2\cos((\emptyset_2)(J_0(B) + 2J_2(B)\cos(2w_{2m}t))) \qquad 3\text{-}64$$

Here equation 3-61 is the signal for first harmonic first arm, equation 3-62 for second harmonic first arm, equation 3-63 for first harmonic second arm, and equation 3-64 for second harmonic second arm.

Considering $E_0 = 1, w_{1m} = 0.1, w_{2m} = 0.2, A = B = 1,\ \emptyset_1 = 2\pi w_1 t,\ \emptyset_1 = 2\pi w_2 t,$ t=1:1000, $w_1 = 0.01,\ \ w_2 = 0.02$, the interference signal for harmonics extracted from the measurement of each mirror and also the quadrature plotted with these harmonics can be plotted. Figure 42 shows the first harmonic of mirror one measurement (equation 3-61) (a), and second harmonic of same measurement (equation 3-62) (b). Also these two harmonics are plotted versus each other (c).

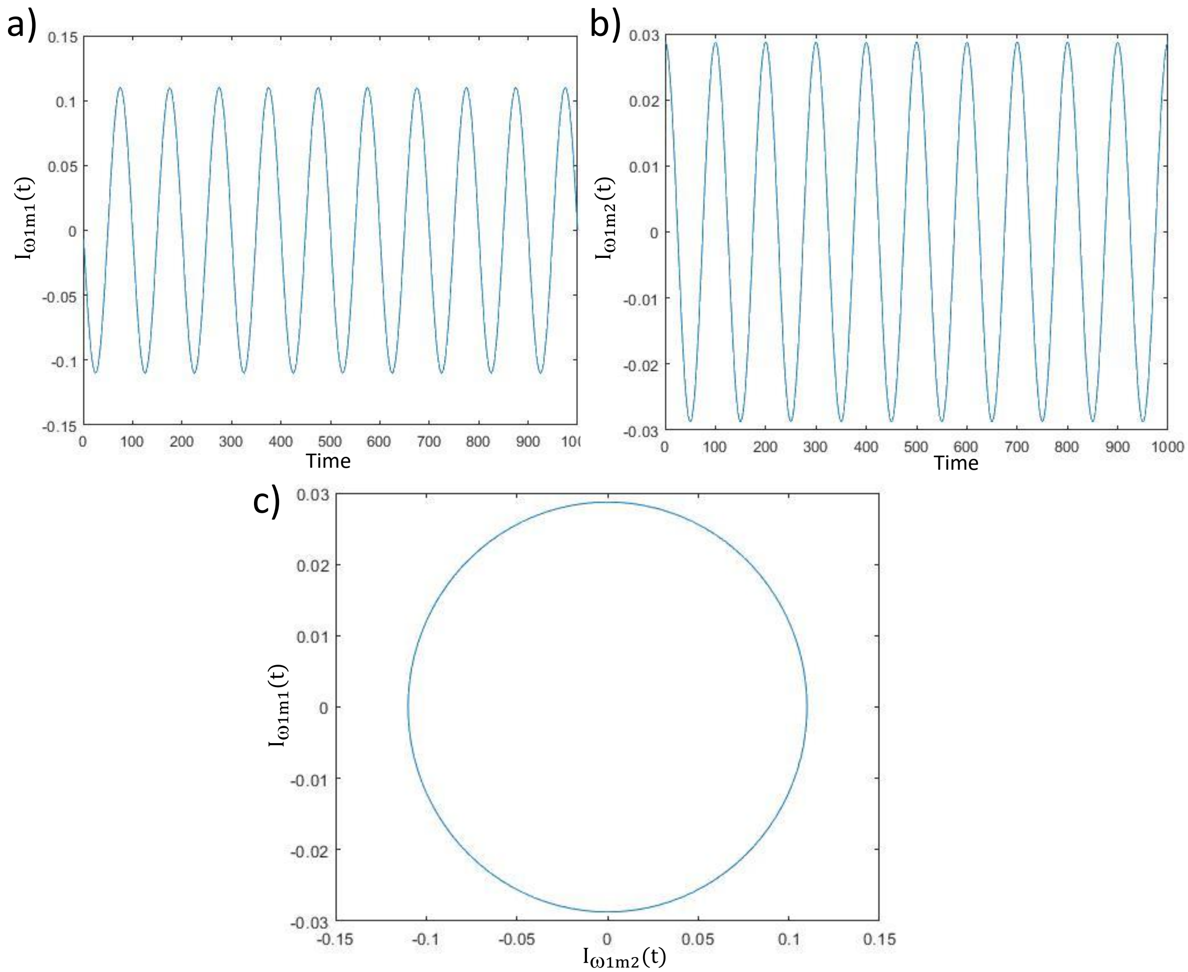

Figure 42. a) First harmonic first arm, b) Second harmonic first arm, c) First arm quadrature

Figure 43 shows the first harmonic of mirror two measurement (equation 3-63) (a), and second harmonic of same measurement (equation 3-64) (b). Also, these two harmonics are plotted versus each other (c).

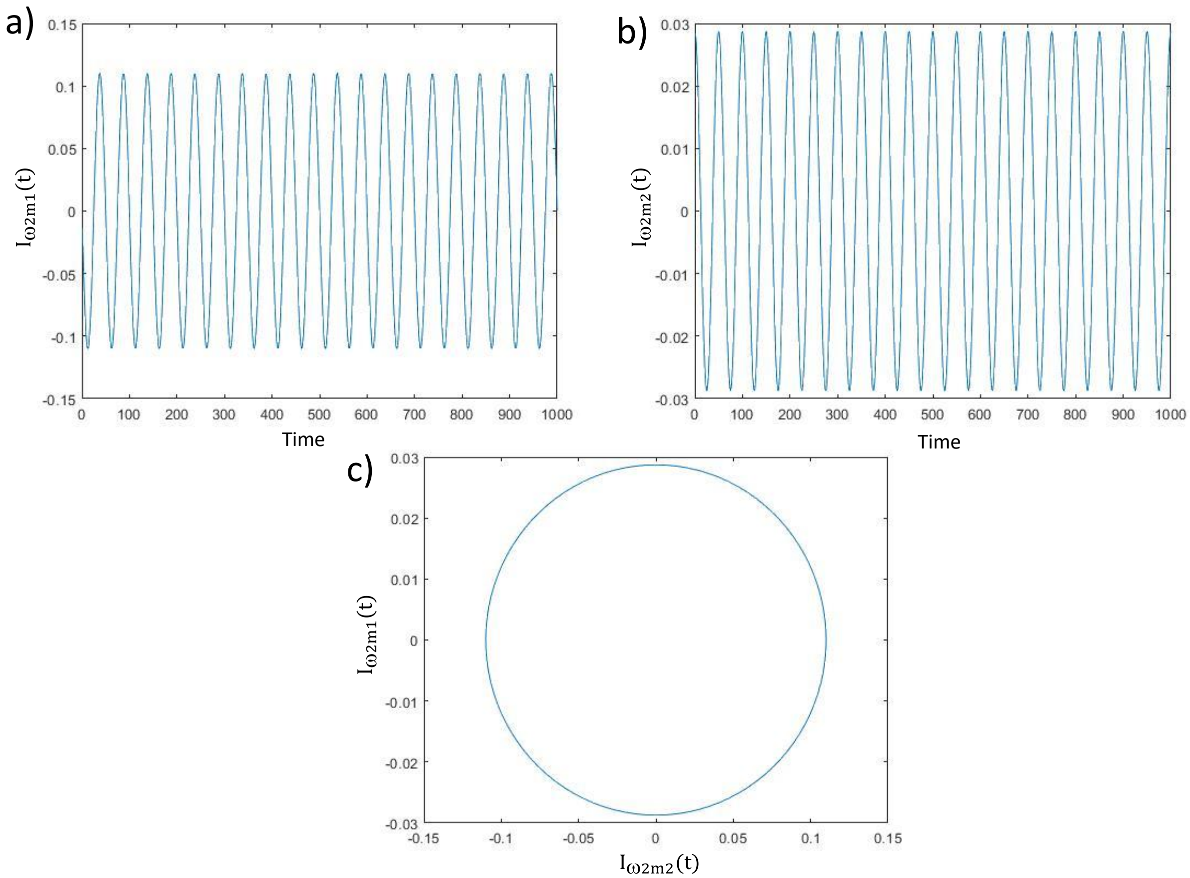

Figure 43. a) First harmonic second arm, b) Second harmonic second arm, c) Second arm quadrature

3-3 CONCLUSIONS

The theory given in this chapter represents the mathematical equations of the optical interferometry and signal conditioning units. The optical design and implementation of the Fabry-Perot interferometry that discussed in detail for a uni-directional cavity and bi-directional cavity in this chapter is going to be presented in chapter 4 (section 4-1). In addition of that one directional and two directional modulation systems in explained in detail in chapter 4 (section 4-2).

The signal conditioning part (Fourier transform) for a one-directional or two-directional system is discussed in chapter 5 (section 5-2) and the results of all measurements using one-directional or two directional approaches is presented in chapter 6.

CHAPTER 4 PROBE DESIGN IMPLEMENTATION

Both a one directional probe and two directional probes have been created during this study. The one directional probe is a profilometer with capability of scanning the profile of a surface placed orthogonal to the measurement axis of the probe. The two directional probe on the other hand, is designed to scan two orthogonal surfaces (orthogonal to the axis of the probe and along the axis of the probe) independent from one another and simultaneously. The system of opto-mechanical design is same for both probes other than some minor differences that are explained in more detail in section 4-2. This chapter explains the opto-mechanical-electrical design of the systems in general, a detailed description of the one directional and two directional designs of the probe and different configuration for implementation of the two directional probe, and the structure of the final manufactured and fabricated probes and testing apparatus.

4-1 SYSTEM

This system comprises one or more coherent light sources that transmit through a partially transmissible reference surface into a beam splitter, the beams emerging from the beam splitter are incident on sample surfaces and a portion of each beam is reflected and coupled back into the optical system, see Figure 44. Within the optical system is an oscillator capable of independently dynamically varying optical path lengths in the directions of the split beams and thereby introducing optical modulation. These modulated light beams pass back through the reference surface combining with the original partially reflected beam to create an interference pattern. Such a configuration is commonly referred to as a Fabry Perot interferometer. These interference beams contain phase information at the frequencies of modulation and can be separately measured from the signal at one or more detectors.

Referring to the block diagram shown in Figure 44 the source is either one or two coherent sources (laser diodes in this case) that are launched into optical fibers. For either number of lasers the source is combined into a single fiber that delivers the light to the probe. Light emerging from the fiber passes through a GRIN lens for focusing and a beam splitter to split the light into two orthogonal paths. A piezoelectric actuator connected between the probe body and the optical assembly is used to mechanically modulate this assembly along the two optical axes. Light emerging from the probe is reflected by the surface under test back into the beam splitter where it combines with internal reflections, mainly from the end of the fiber and Grin lens. Interference of these two beams results in phase modulation that, in turn, produces harmonics that are used as quadrature signals to extract phase information (Nowakowski. et al., 2016), (Schulz, and Lehmann, 2013), (Arablu and Smith, 2013), (Boef, 1987).

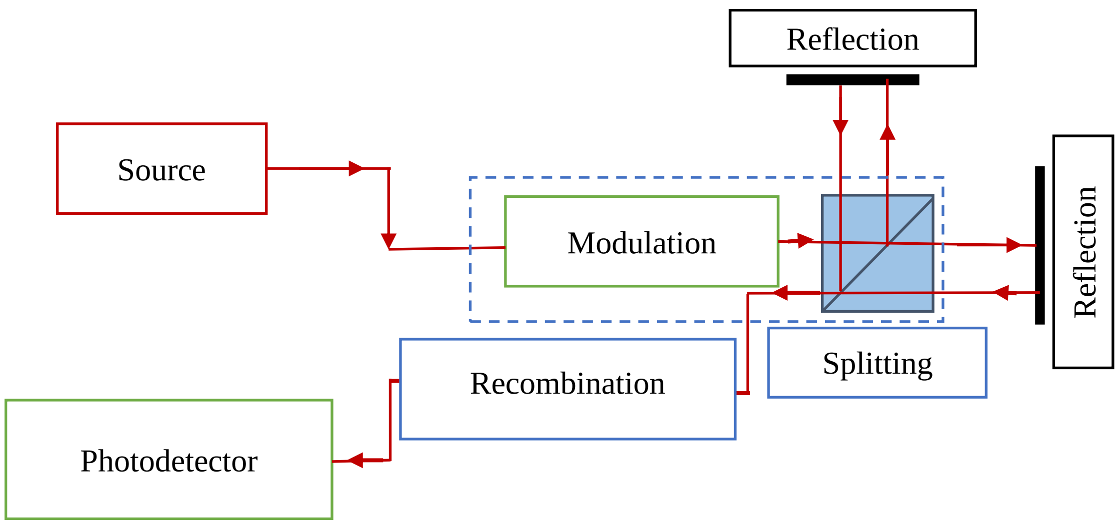

Figure 44. General configuration of the two-direction optical probe system.

4-2 PROBE OPERATION

In this thesis a Fabry-Perot interferometry fiber-based probe is designed, fabricated, and tested to perform a surface measurement using mechanical modulation of the light. For that purpose, two different designs of the probe were implemented. First, a one directional probe was designed and fabricated to evaluate the performance of a Fabry-Perot interferometry probe for measuring topography of a surface. After doing some measurements and determining the performance specifications of the system, a two directional probe was created. This design has the advantage of scanning multiple surfaces with different directions, simultaneously and the compact design makes it possible to scan hard to access surfaces like the inside surfaces of tiny holes.

4-2-1 ONE DIRECTIONAL MEASUREMENT

In this design, a 633 nm laser light source (Arroyo instruments, 205 TEC Butterfly) is launched into a two by one optical fiber (Thorlabs, TW630R5F1) which goes through the optical probe head. The probe head is designed to hold a piezo electric actuator plate (Noliac, NAC2001) in between two aluminum parts and has a hole in the center to pass the fiber through. A high electric voltage signal with desired modulation frequency is applied to the aluminum parts. A GRIN lens (Thorlabs, GRIN2306A) is assembled to the fiber ferrule using a glass sleeve and the assembly is attached to the second aluminum part, see Figure 45. The piezo plate actuator modulates the phase of light by mechanically moving the GRIN lens up and down. The light focuses on the measuring surfaces that is within the focal length of the GRIN lens and reflects back to the GRIN lens. The light couples back to the fiber and is detected using a photodetector. Signal from the photodetector goes through the signal conditioning unit for amplification and filtering and, after converting to digital signals, applying Fourier transform and phase unwrapping algorithms. A schematic overview of the system is shown in Figure 44.

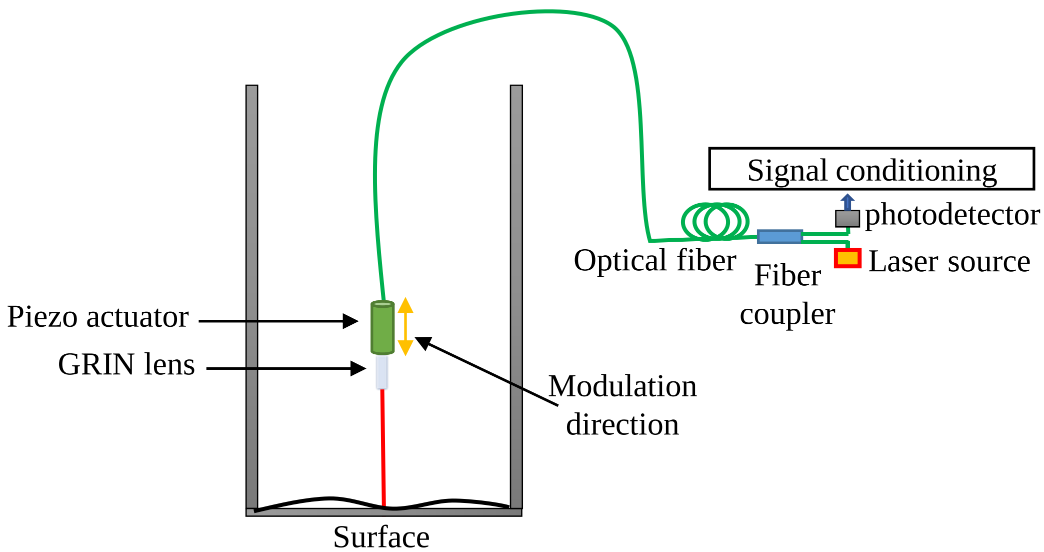

Figure 45. Schematic of a one-directional optical probe

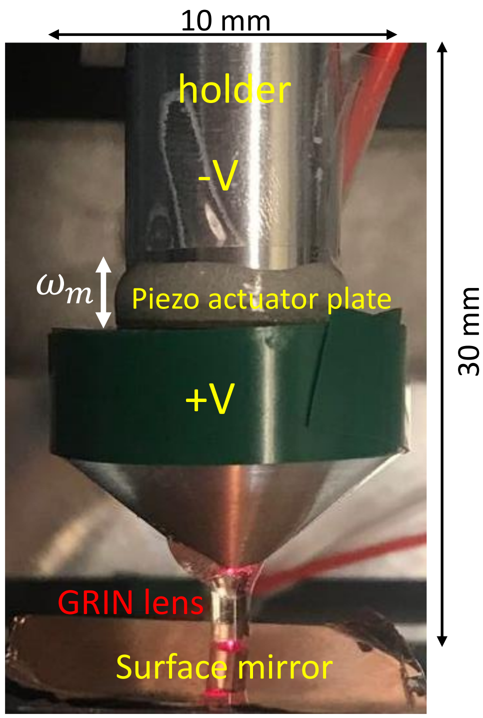

Figure 46. One directional probe head design.

4-2-2 TWO-DIRECTIONAL MEASUREMENTS

General operation of the two-directional probe is illustrated in Figure 47. In this case, light from the laser source feeds into a two by one fiber coupler, the output of which transmits light to the probe. As illustrated light emerging from the modulated optical system is reflected by the surfaces 1 and 2 of the specimens under test. Interference that occurs within the probe transmits back along the fiber and a portion of this arrives at the photodetector. Lock-in amplifiers are used to measure the modulation harmonics.

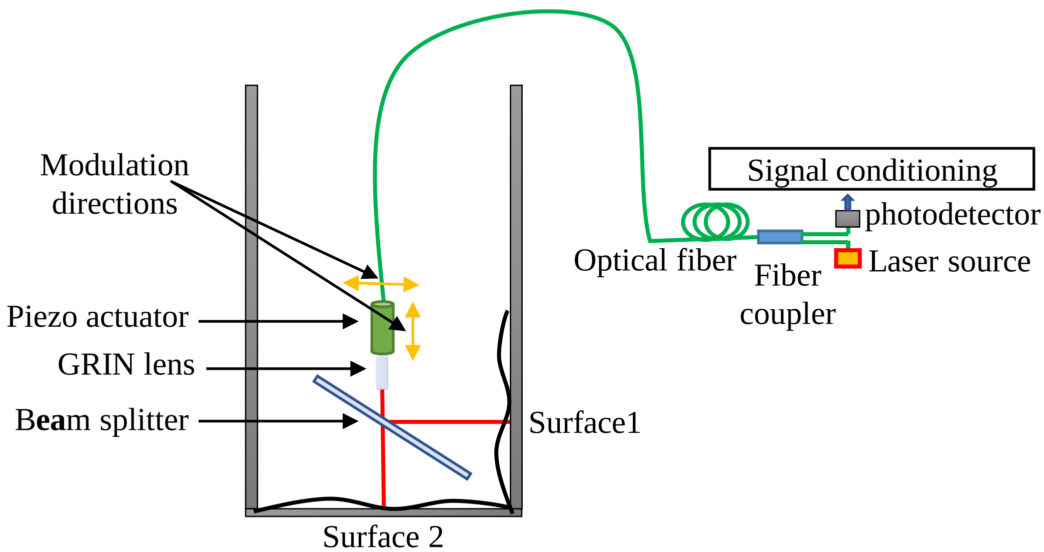

Figure 47. Schematic of two-directional optical probe

In this thesis a single and dual source probe have been fabricated and tested. Implementation of the single source probe is shown in Figure 48. For this single source probe, a 633 nm laser diode is used (Arroyo instruments, 205 TEC Butterfly) with current and temperature control (Arroyo instruments, 6310 ComboSource). The laser source feeds directly into a single mode fiber (Thorlabs, P5-630AR) that in turn is connected to a two by one coupler (Thorlabs, TW630R5F1). The single output from the coupler is attached to the GRIN lens (Thorlabs, GRIN2306A) assembly that is bonded to the beam splitter as shown in **Error! Reference source not found.**. For this single wavelength probe, a 50-50 silvered mirror tilted at a 45-degree angle relative to the GRIN lens axis splits the beam into two orthogonal directions, one along and the other perpendicular to the axis. As well as fixing the GRIN lens and splitting mirror, the aluminum body (detailed in Figure 48) of the beam splitter also attaches to the piezoelectric tube actuator (Piezo Drive, TB1005) that provides the mechanical modulation of the probe tip. The base of the probe is bonded to the other end of the piezoelectric actuator that is fastened into a mechanical motion control system that is used for positioning the probe relative to the specimen surfaces prior to testing. Shutters are used so that interference is limited to a single optical path and these shutters can be rapidly switched to determine phase in each probe direction.

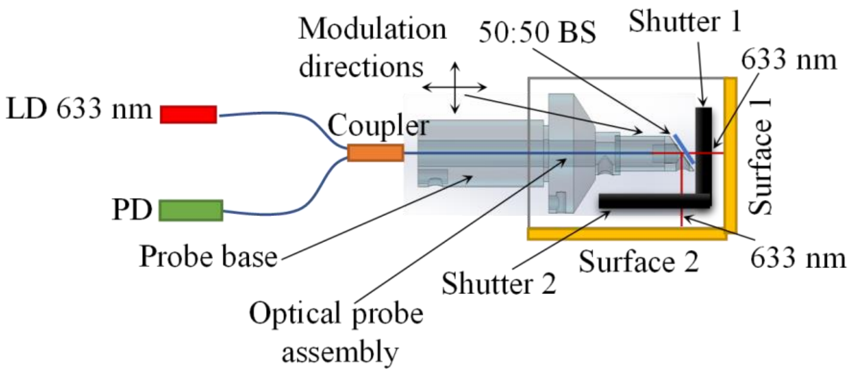

Figure 48. Configuration of a shutter separation optical probe using a single light source.

A detailed cross section of the dual source probe is shown in Figure 49. This second implementation shares common components of the previous design. However, this new design uses two sources of different wavelengths 633 nm (Arroyo instruments, 205 TEC Butterfly) and 660 nm (Thorlabs, LP660-SF60) that are combined into a single mode fiber. For this dual source probe, a dichroic mirror is used as the beam splitting element. This has the advantage that the full intensity of each laser diode is available in each axis and the sources do not interfere and therefore can be readily used simultaneously.

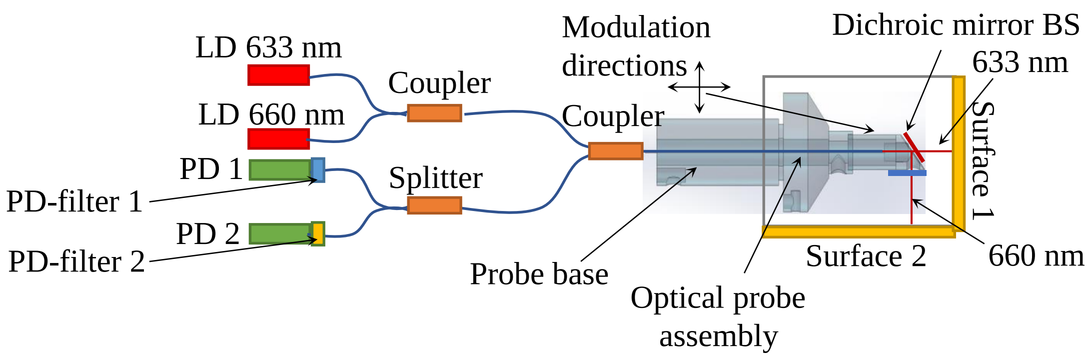

Figure 49. Configuration of a wavelength separation optical probe with two different wavelength light sources.

A photograph of the dual source probe (with background removed but otherwise unmodified) is shown in Figure 50. The reason for the second dichroic mirror indicated in this figure will be explained in chapter 5.

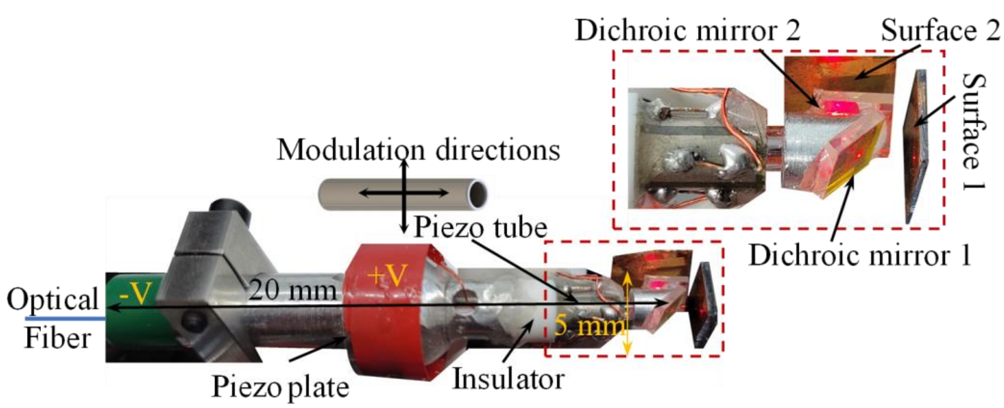

Figure 50. A picture of the two directional optical probe assembly including two dichroic filters and the two mirrors being under the test.

Figure 51 shows a detailed cross section of the probe in this case using the dichroic mirror splitter. Common to both probes are the assembly of the moving probe head. As can be observed, the fiber is attached to a ferrule that is bonded into the sleeve. The GRIN lens is also bonded to the same sleeve. In turn, this sleeve is bonded into an aluminum beam splitter body. The beam splitter body has a 45° surface for bonding the beam splitter mirror 1 and the complete assembly is then bonded onto the end of a piezoelectric tube actuator. As light emerges from the fiber, a small portion will reflect back, and this light becomes the source of interference.

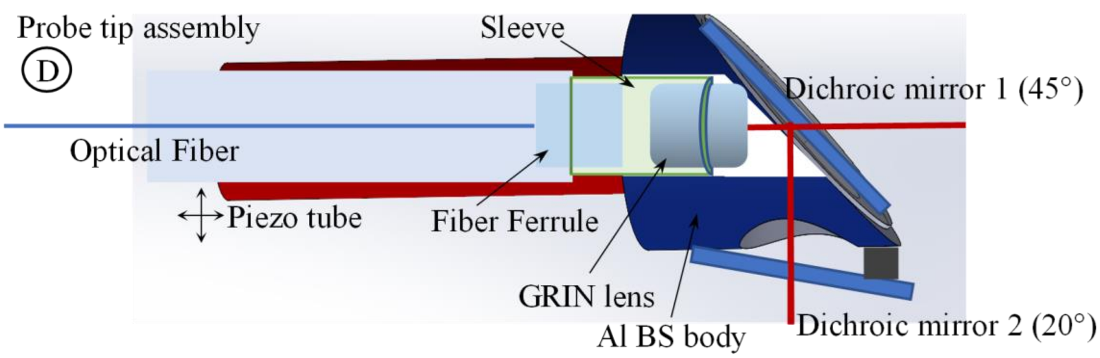

Figure 51. The solid model of the optical probe design using a dichroic beam splitter.

A cross section of a third configuration that were only designed for separation of measurements of two different surfaces and avoid interference between them is shown in Figure 52. This design is as same as the single source probe with one difference of using a polarized beam splitter instead of a simple intensity 50/50 beam splitter. In this case the state of the polarization for the measurement of each surface will be different (S for vertical surface and P for horizontal surface) and this makes it possible, to do both measurements simultaneously and independently.

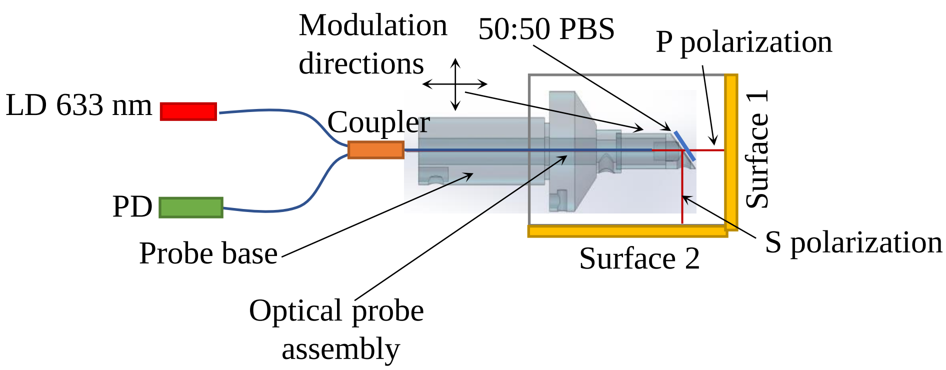

Figure 52. Configuration of a polarization separation of optical probe

4-3 FINAL PROBE DESIGNS AND TESTING METHOD

To demonstrate independent measurement from orthogonal surfaces, two plain mirrors (surface mirror 1 and surface mirror 2 in Figure 54) were attached to separate piezoelectric translation stages with their translation axis along each probe axis. Movement of each stage is measured using capacitance displacement gauges (Lion Precision CPL-190).

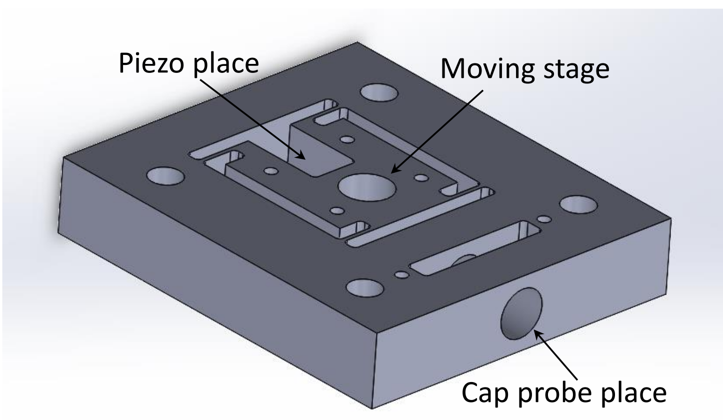

Figure 53. Photograph of a Piezo electric actuator stage.

During experiments each of the piezoelectric actuators is energized using a slowly, sinusoidally varying voltage resulting in a peak to valley motion typically of around two micrometers amplitude (corresponding to between six to ten optical fringes). These two translation stages and capacitance probes are shown schematically in Figure 54.

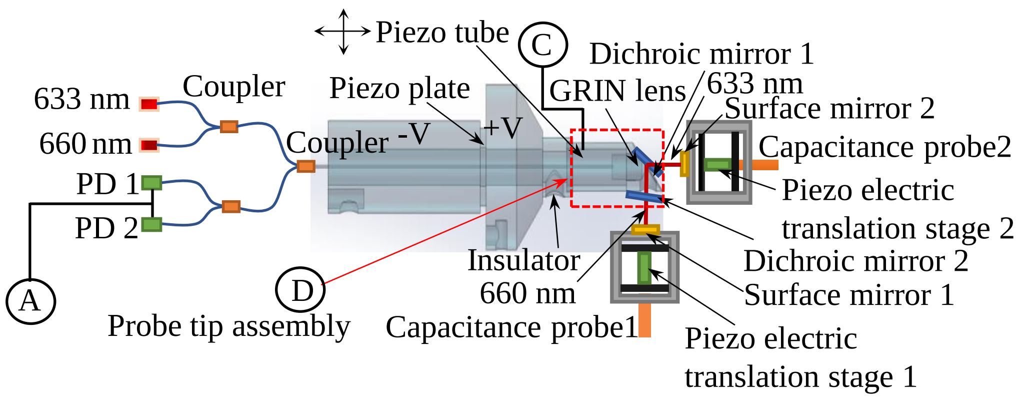

Figure 54. The measurement system including two piezo electric actuator flexure stage

CHAPTER 5 PROBE PERFORMANCE TESTING AND EVALUATION

In this chapter a detailed overview of the sub-components of the probe system including dichroic filters (bandwidth and transmission measurements), signal processing hardware, and phase extraction procedures is presented. In section 5-3, the phase extraction procedure including the test procedure and the results of capacitance gauge calibration, methods of modulation, effect of temperature on the test, noise bandwidth, compensations and errors, signal conditioning units and laser stability is presented.

5-1 DICHROIC MIRROR SPLITTER FABRICATION

Figure 54 shows two dichroic mirrors (mirror 1 (Optical Filter Shop, Visible Bandpass Filter – 680 nm FWHM 20 nm), mirror 2 (Optical Filter Shop, Visible Bandpass Filter – 667 nm FWHM 17 nm) in the probe assembly. Figure 55 (a) shows a dichroic filter being compared to a 50/50 silver deposited beam splitter with both elements leaning against a stick. Figure 55 (b) is showing the procedure of mounting dichroic filter 2 on the probe assembly. In this assembly it was necessary to arrange the second dichroic filter at an angle of 20° to the beam reflecting from the first dichroic mirror beam splitter. This was achieved by placing the probe onto a flat plate. The beam splitter mirror was then aligned to be perpendicular to the plate surface using a precision square. Following this, a 20° angle plate was used to bring the second dichroic filter into contact with the head of the probe after which it was secured using epoxy fillets.

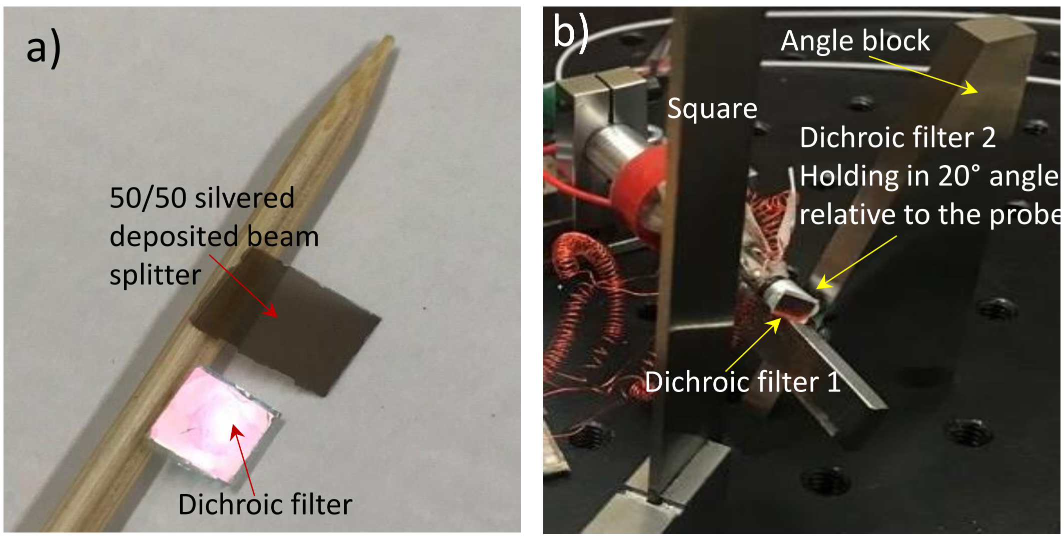

Figure 55. a) A picture of dichroic filter and 50/50 beam splitter, b) A picture of the design to assemble the dichroic filter 2 holed in 20° relative to the probe.

The second dichroic mirror was necessary to fully isolate the two wavelengths. The reason for using two dichroic mirrors can be understood from curves of mirror transmission as a function of incident angle and wavelength shown in Figure 56 (dichroic filter 1) and Figure 57 (dichroic filter 2). Figure 56 shows the wavelength transmission curves for incident angles ranging from 0 to 45 degrees for dichroic filter1. Because the beam splitter needed to be 45 degrees, the measured transmission spectrum is shown bold red and the wavelengths of the two laser sources are shown by vertical lines. From Figure 56 there is 75% transmission for 633 nm wavelength and near 0% at 660 nm. There will remain a significant reflection of the 633 nm beam reflecting colinear with the 660 nm beam. The second mirror has been added to remove this fraction of the 633 nm beam and its transmission characteristic as a function of incident angle is shown in Figure 57. Extracting the transmission characteristic at a 20-degree incident angle can be seen that the 633 nm component is substantially removed while 90% of the 660 nm beam will continue through. Hence mirror 2 is placed in the optical path at this 20-degree angle. Because mirror 1 is used to split the two wavelengths, it can be considered as a beam splitter while mirror 2 removes unwanted reflection at 633 nm and therefore functions as a filter.

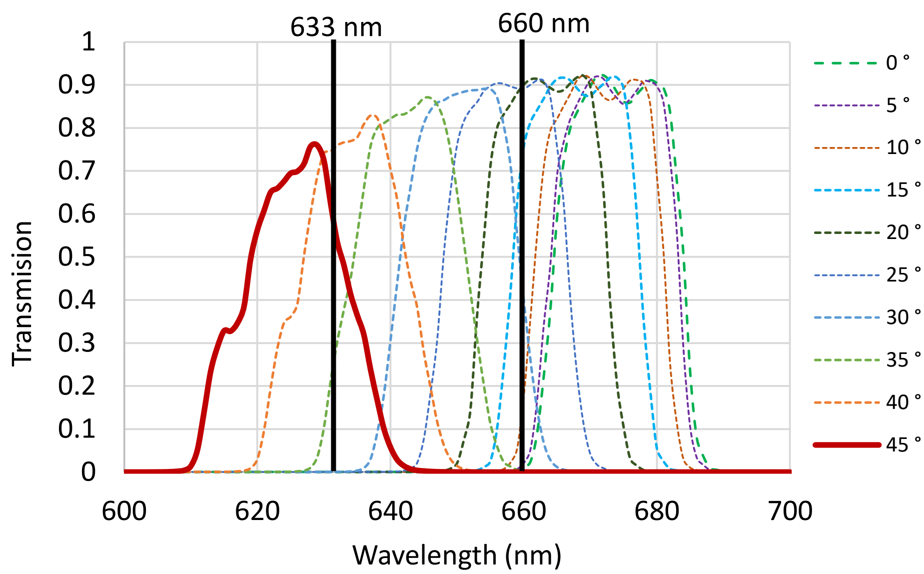

Figure 56. Transmission function of dichroic filter one for 0 to 45° angle.

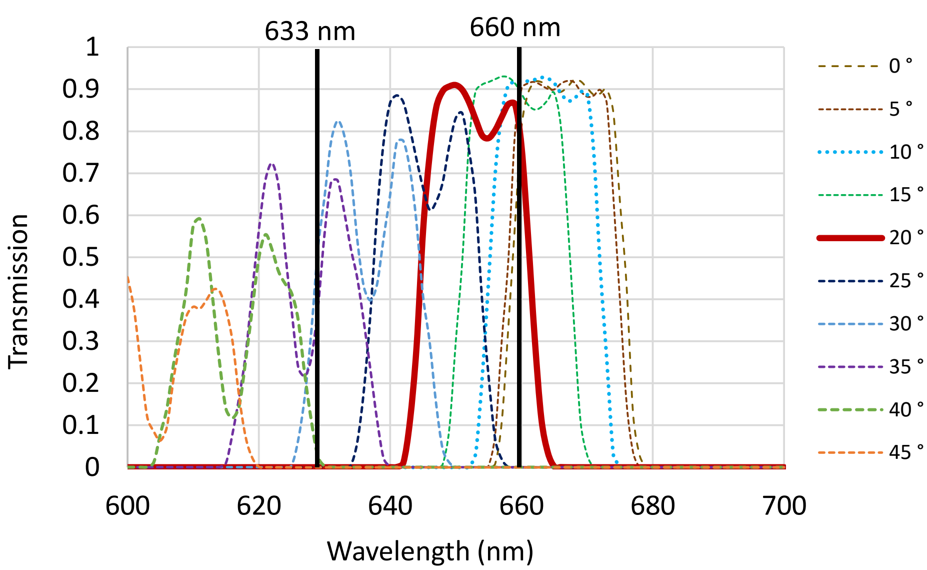

Figure 57. Transmission function of dichroic filter two for 0 to 45° angle.

5-2 SIGNAL PROCESSING

The modulated interference beams from the probe are transmitted back to the fiber coupler and will emerge from the free end. In principle the harmonics for simultaneous measurement using the dual source probe will occur at separate frequencies. In practice, during these experiments the harmonics and their subsequent interactions made it difficult to separate harmonic amplitudes using lock-in techniques (Lucia Diaz Perez, 2019). For the measurements in this paper, the dual source probe output beam was split and filtered using dichroic mirrors (Optical Filter Shop, Visible Bandpass Filter – 620 nm FWHM 20 nm) and (Optical Filter Shop, Visible Bandpass Filter – 660 nm FWHM 10 nm) one in front of each detector to isolate the laser source wavelengths and therefore separate interference paths. The output intensities measured by each detector are then processed through a Sallen-Key high-pass filter (100 Hz cut-off). In practice the harmonic signal voltages were in milli-volts range and further analog amplification and signal offset was required prior to digitization and analysis. This final analog signal was digitized using a 16-bit analog to digital convertor ADC (Texas Instruments, ADS8412EVM) and transferred at 1 Msps into the FPGA for Fourier analysis (see Figure 61). Fourier coefficients are then transferred into a real-time processor for normalization and quadrature phase extraction, see Figure 58 and Figure 59.

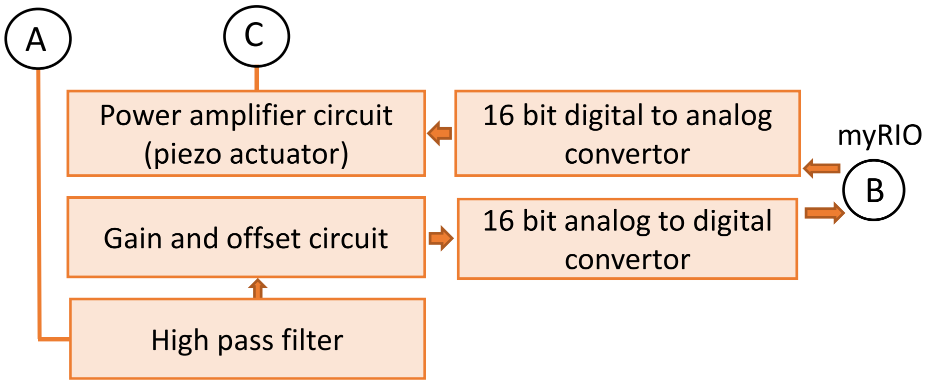

Figure 58. Diagram of the analog modulation and signal conditioning interactions.

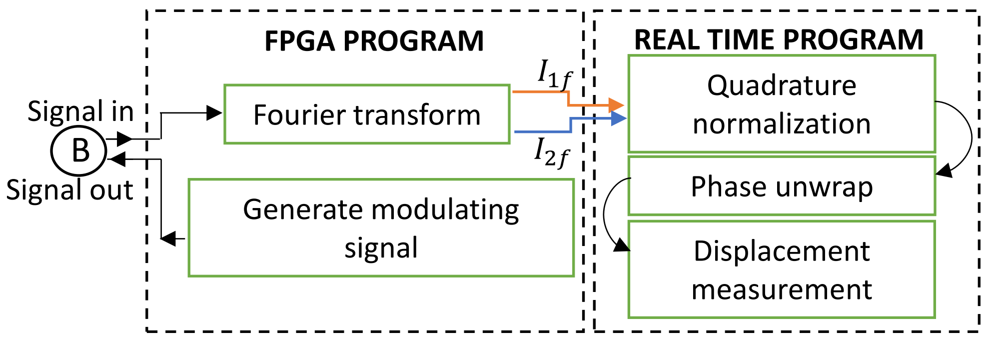

Figure 59. Diagram of the digital signal generation and processing units including FPGA and Real-time programming.

After analog signal processing, measured data is streamed into the FPGA where Fourier components of the harmonics are extracted. The phase is measured synchronous with the sinusoidal modulation signals sent to two digital to analog converters (Digilent pmod DA3, 410-241) that, in turn, provide the drive signal to the power amplifier circuits (OPA541AP) that produce the drive for mechanical oscillation for the probe head. See Figure 60.

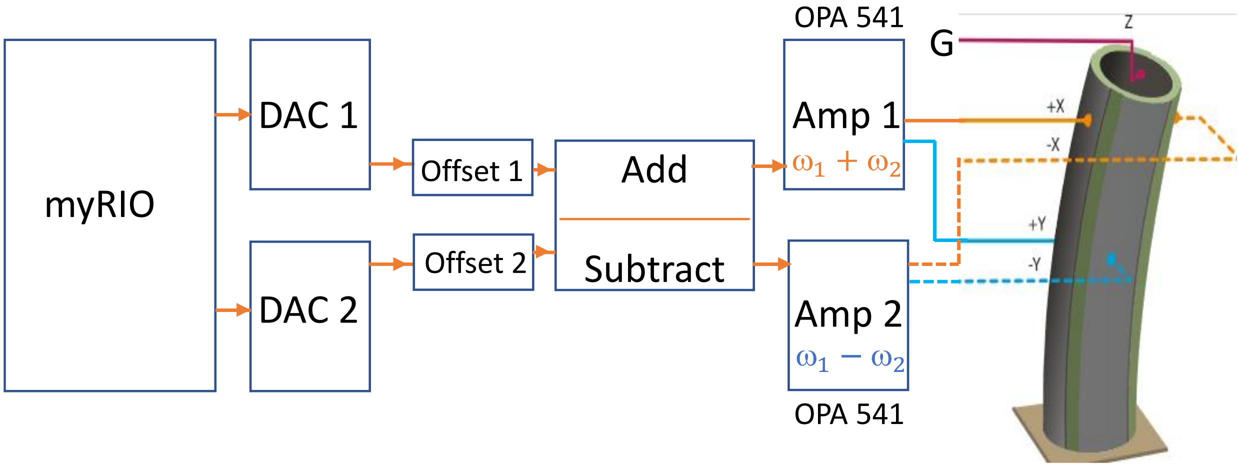

Figure 60. A diagram of the modulation signal conditioning.

Fourier coefficients are obtained using a lookup table. These Fourier coefficients are then transferred into a real-time processor where fringe amplitudes are renormalized, and unwrapped phase is used to provide a measure of displacement computed using equation (3-42).

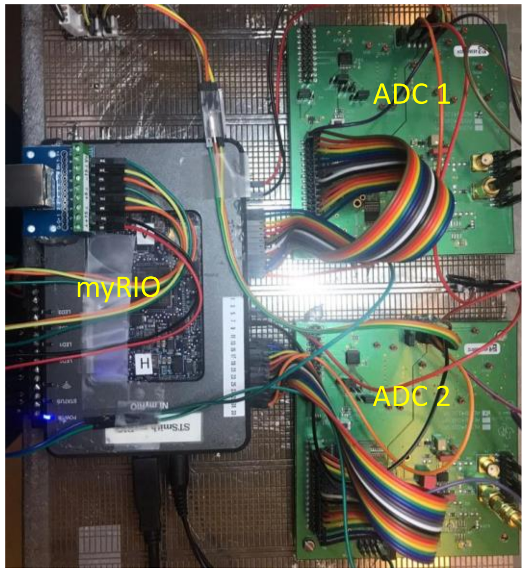

Figure 61. Photograph of ADC/myRIO connection.

5-3 PHASE EXTRACTION

For phase extraction and measurement of the profile of a surface in one-directional probe and displacement of two mirrors in two-directional probe, separate test bench was designed and assembled. In this section the test procedure for each of the one-directional and two-directional probes is explained and the results of all compensations and corrections are given.

5-3-1 TEST PROCEDURE

5-3-1-1 ONE-DIRECTIONAL PROBE TEST

For testing the one-directional probe, a controlled closed loop stage was designed and made using mechanical blocks, a voice coil as the actuator, an LVDT gage for monitoring displacement and an angle adjustable stage to remove tilts of the stage and adjust the alignment of the specimen surface relative to the direction of motion of the stage. The one-directional probe is held on top of the stage and the specimen (a diamond-turned aluminum sample) is placed on the moving platform. A stage angle aligner was designed and made using springs and screws.

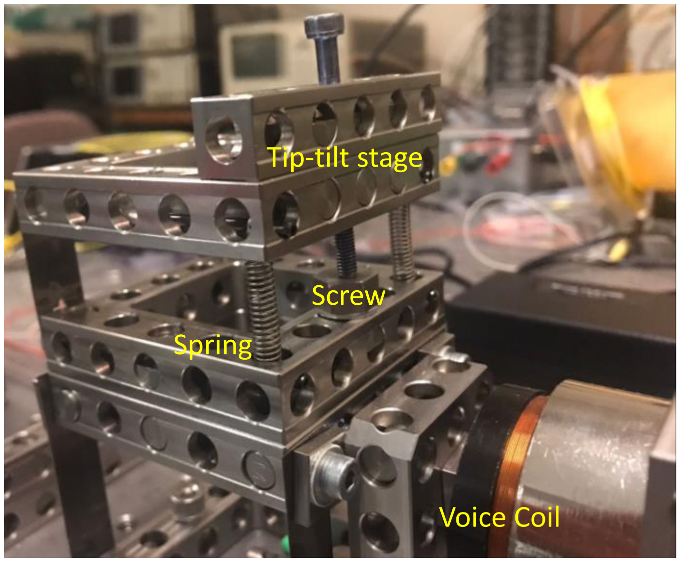

Figure 62. A picture of a tip-tilt aligner stage.

A PID controller was implemented to provide the desired displacement based on feedback from the LVDT. The program for a PID controlled loop system is written in LabVIEW. The range of scan in this experiment was 1.2 mm and the speed of scan was 0.1 mm/s.

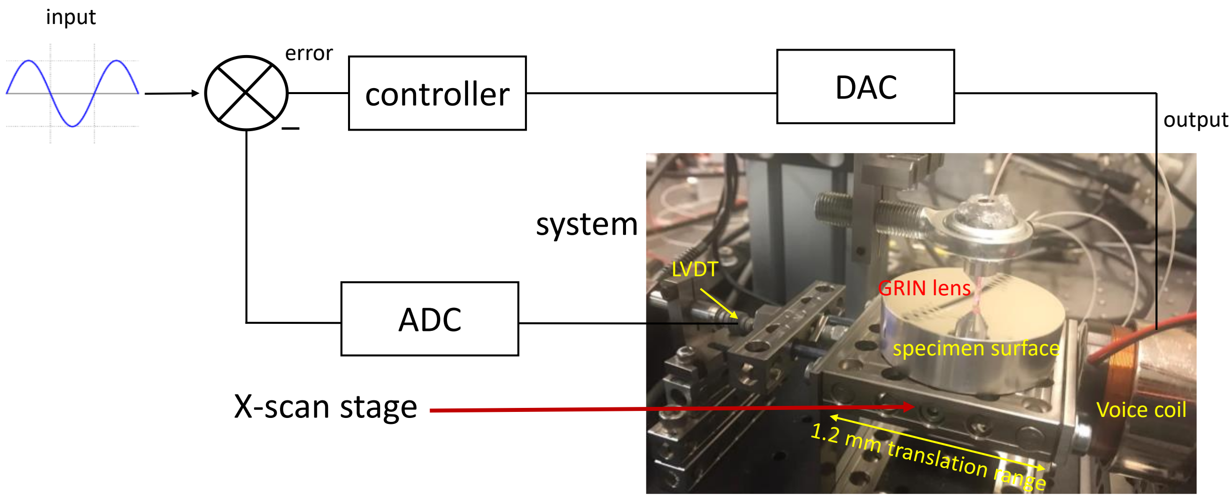

Figure 63. PID controlled loop stage for one-directional probe test procedure

5-3-1-2 TWO-DIRECTIONAL PROBE TEST

For two-directional probe, two piezo electric actuator stages (see Figure 53) were designed in solid works and fabricated. Each of these stages were used to move a copper mirror back and forth along each sensing direction of the probe. A capacitance gauge is mounted on each stage and measures the movements of each mirror for later comparison with the displacement measurements of the probe.

After mounting the mirrors on the piezo electric actuator stages, the probe is also placed on a x-y micrometer stage in a relatively appropriate distance from the mirrors. Using two tip-tilt aligners for the mirror holders and x-y micrometer stage for the probe, the two directional Fabry-Perot interferometer was manually aligned to present the best interferometric signal on each of the directions (the interferometric signal can be observed in an oscilloscope when the piezo electric actuators are working, and the stages are displacing back and forth). The setup for two-directional probe test is shown in Figure 64.

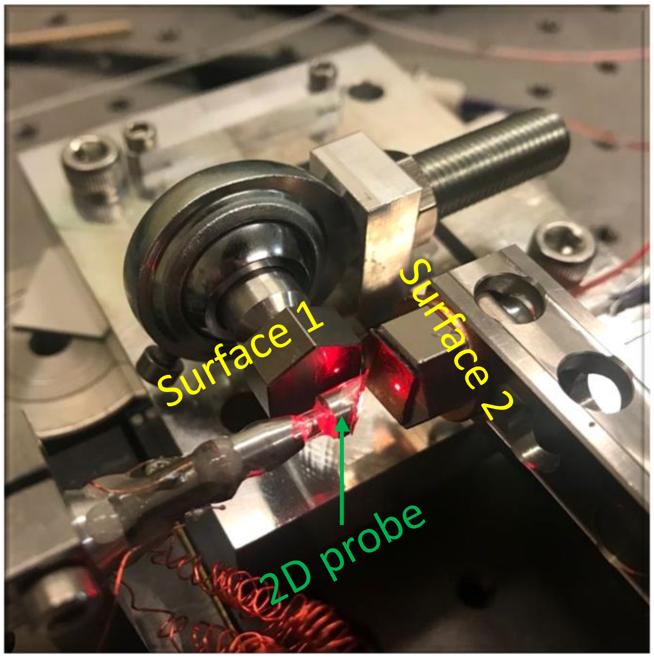

Figure 64. A picture of the two directional probe test bench.

5-3-2 PERFORMANCE TESTING RESULTS

A schematic of the whole system for evaluating a two-directional probe using the wavelength separation configuration is shown in Figure 65. This system includes the probe assembly, the two-directional probe test bench, the analog signal conditioning units and the digital signal processing units.

Light from 633 nm and 660 nm lasers is coupled into a two by one fiber-coupler and, using a second fiber-coupler, the combined sources are transmitted to the probe (D in Figure 65) which includes the GRIN lens and fiber ferrule assembly, the dichroic filter holder, and the piezo electric actuator tube. The interference modulated signal reflected back from the displacing mirrors (test stages) is coupled back to the third two by one fiber-coupler and the wavelength from each measurement is filtered using another dichroic filter mounted on two photo detectors. After high-pass filtering, amplifying, and offsetting, the signal from the photo detectors (A) is, converted to digital signals that are transferred into the FPGA within a NI myRIO (B). In the FPGA a Fourier transformation is computed to extract the orthogonal harmonics. Quadrature signals are obtained, and the phase is unwrapped in the real-time program. In the same FPGA program, a modulating signal is generated and converted to an analog output signal. After some analog processing (adding and subtracting) and amplification these modulation signals are applied to the piezo electric actuator tube (C). A piezo electric actuator plate is also considered in the setup to provide actuation along the probe axis in some cases when only one directional measurement is required.

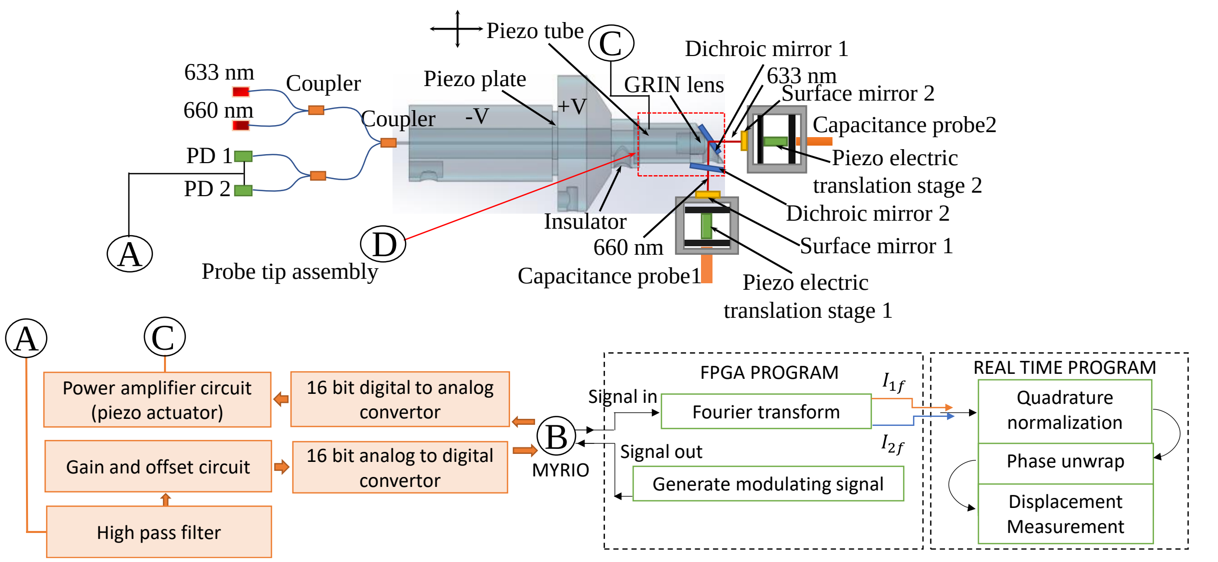

Figure 65. A schematic of the two-directional wavelength separation configuration setup including signal conditioning and signal processing units.

A picture of the whole system including the probe assembly, the test stages (piezo electric actuator stages and the signal generator and amplifiers) and monitoring capacitance probes, the signal conditioning units, signal analyzer and the signal processing LabVIEW screen is shown in **Error! Reference source not found.**.

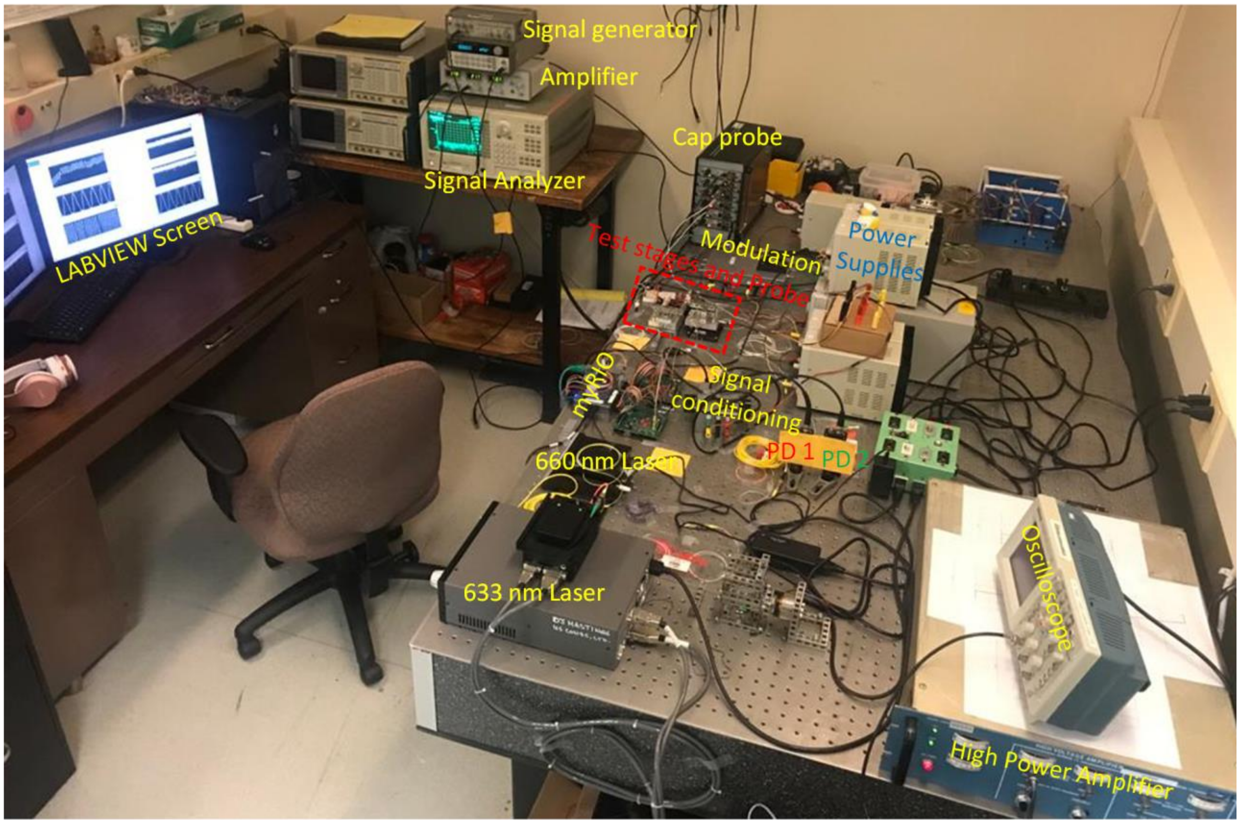

Figure 66. A picture of the two-directional system setup including the whole components.

5-3-2-1 CAPACITANCE GAUGE CALIBRATION STUDY

For comparing the displacement measurement of the probe to a reference measurement, a capacitance probe is mounted on each piezo electric actuator stage. These probes are calibrated and the analog signal voltage versus displacement of a reference surface is plotted for each of them (these measurements have been done manually using a precise micrometer stage). The resulted number for calibration of cap probe one 2.014808 [V/μm] and two 2.009753 [V/μm] is and respectively. Figure 67 is showing the plotted calibration measurements for capacitance probe one and two.

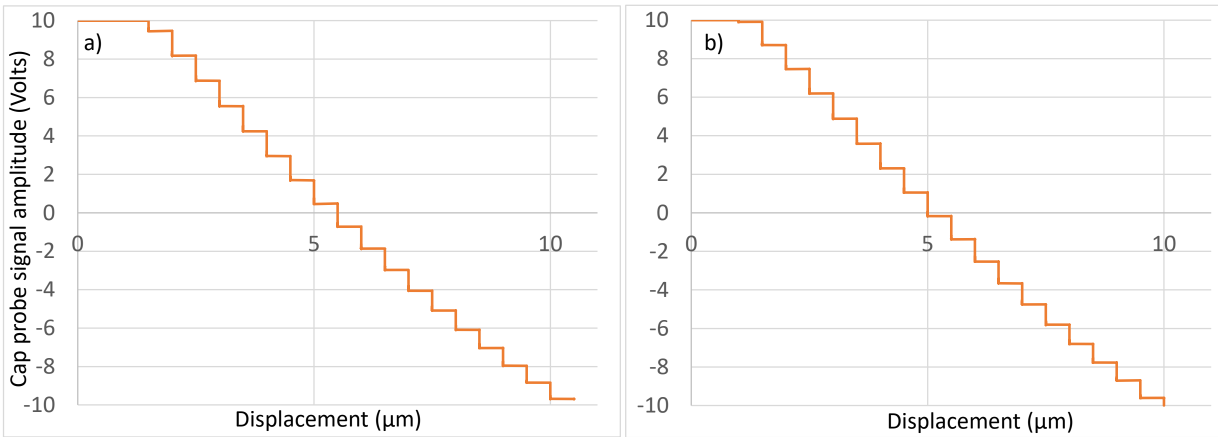

Figure 67. The calibration measurements of a) capacitance probe 1, b) capacitance probe 2 for signal amplitude (volts) vs Displacement (μm).

The cap probe displacement measurements is read through the analog to digital convertors of myRIO and converts to equivalent micrometer displacement measurements using the calibration data for each of the probes. After that it is being compared to the displacement measurements of the probe in the LABVIEW real-time program.

5-3-2-2 MODULATION

For different experiments in this thesis, different kinds of piezo electric actuators have been used depending on what is required for a specific task. For one-directional probe a plate piezo electric actuator was used. The reason of using a plate actuator is it helped to assemble a probe to be as compact as possible. This plate actuator was in a square and for purpose of this experiment was transformed into a ring shape using diamond cutting tools.

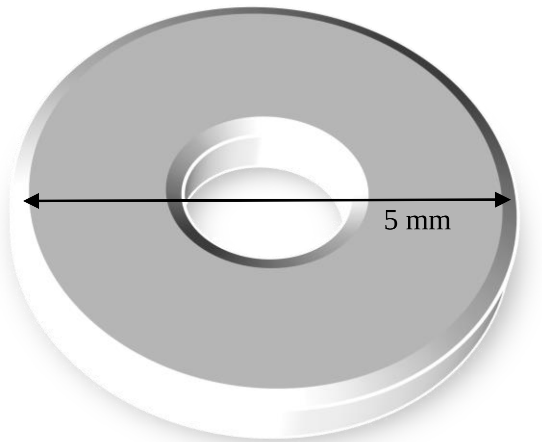

Figure 68. Piezo electric actuator plate for axial modulation of a one directional probe.

The range that a piezo electric actuator can move is dependent on the thickness of the material, see Figure 64. Equation (5-1) is showing the range ΔL that a piezo electric actuator can move under electric field of strength E.

$$\Delta L = d_{33} L E \qquad 5\text{-}1$$

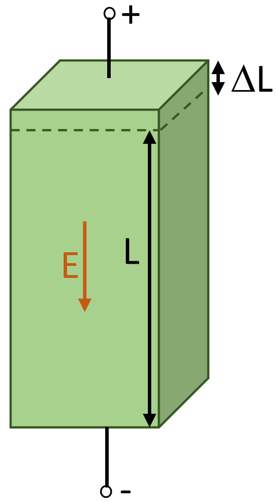

Figure 69. Piezo electric actuator.

where d_{33} is piezo electric charge constant, L is the thickness of the actuator and E is the electrical field applied on the actuator. Because the field is given by the applied voltage divided by length equation (5-1) reduces to

$$\Delta L = d_{33}V. \tag{5-2}$$

For stack type actuators the total displacement is the sum of displacements of each individual element.

For the two directional probe a tube piezo electric actuator was used. Piezo electric tube is a cylindrical shape tube that 4 electrode plates are placed in equal spacing around it. By applying electric field on each of these plates, it cause the material to contract or extend depend on the electrical field direction. this makes the tube to be able to move along the central axis or perpendicular to it. In addition to the compact size and ideal shape for purpose of this experiment it has the capability of simultaneously moving in three orthogonal directions. This feature of tube piezo electric actuator is beneficial for a two directional modulation probe which was the purpose of this experiment.

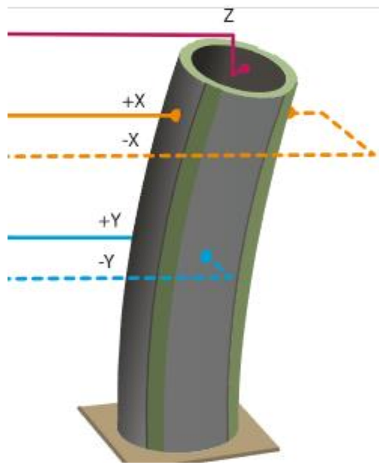

Figure 70. Piezo electric actuator tube.

For the test bench, two piezo electric actuator stack was used in the piezo electric actuator flexure stages. A piezo electric actuator stack is consisting of a stack of many piezo electric layers that are mounted on top of each other all in same direction of polarity. The reason of using these stacks was the pretty much high range of movement and the stiffness of it which makes it a good option for the flexure stage application.

Figure 71. Piezo electric actuator stack.

5-3-2-3 EFFECT OF TEMPERATURE

To decrease the effect of temperature, several things was being considered. For lasers, a temperature and current controlled laser diode was purchased to stabilize wavelength and intensity as far as possible. Optical fibers are the other components that are also sensitive to variations of temperature. To avoid instability, they were all kept into the boxes and taped down onto the large optical bench to prevent movement and rapid temperature changes. The last component that was important to keep the temperature around it constant was the optical components (the probe assembly and test stage) was isolated from all electronics and instruments.

5-3-2-4 NOISE-BANDWIDTH

After recording the interference signal from the dual source probe measurements, analog signal conditioning, analog to digital conversion, applying Fourier transform on the digital signal, and finally unwrapping phase and draw a quadrature, it is necessary to estimate noise in each axis of the probe and have an evaluation of the system precision and resolution of the surface measurements. For that purpose, a digital high-pass filter with a cutoff frequency of 0.1 Hz is applied to the dataset, and the residuals of each measurement are computed. For the dual-source probe, the filtered noise measurements are shown in Figure 72 from which a rms value of 8.1 nm was measured for each probe axis. To determine a noise floor for each probe axis, the mirror translation stages were turned off so that the mirrors remained stationary after which the probe noise in each axis reduced to a rms value of 2.8 nm. One axis of this noise floor measurement can be seen as the white points within the moving mirror noise trace. A similar analysis of the single-source measurements results in a rms noise of 9.7 nm on the vertical axis and 7.9 nm on the horizontal axis.

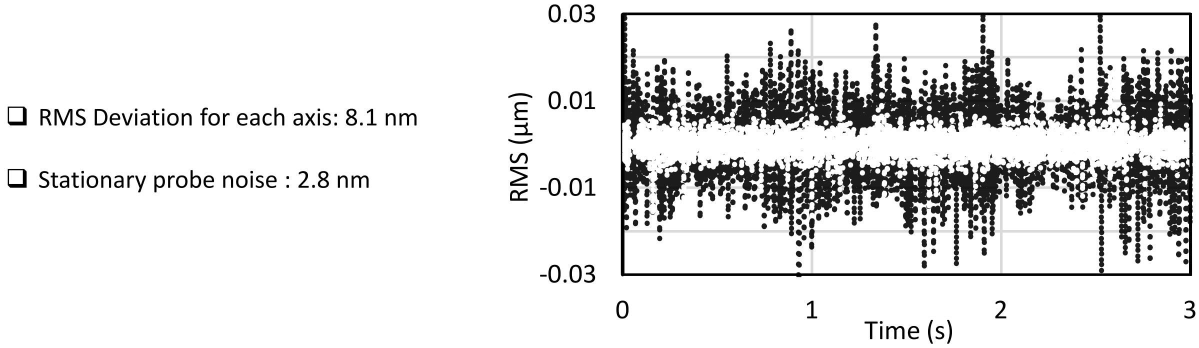

Figure 72. High pass filtered data from the measurements of dual-source probe, indicating measurement noise for 633-nm wavelength axial measurement (black) and measurement noise floor corresponding to stationary mirrors (white).

5-3-2-5 COMPENSATIONS-CORRECTIONS

The one directional probe was used to measure the profile of a diamond turned polished aluminum surface sample using a GRIN lens to focus the light onto the surface (see Figure 73). After recording the data in this measurement, the result was showing a slight tilt on the stage that the sample was placed on, and also a small curve on the sample surface itself as it is illustrated in Figure 74. This tilt is because of some problems in the mechanical stage alignment and assembling. The surface curvature is also a part of the polishing process and cannot be avoided completely.

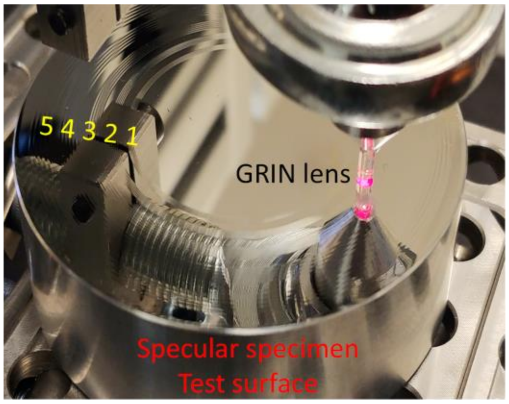

Figure 73. Diamond-turned surface sample.

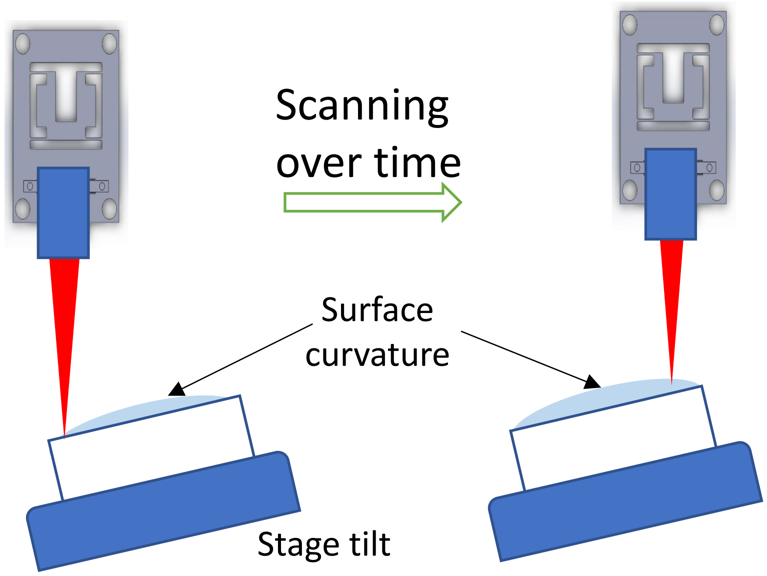

Figure 74. A schematic of the scanning process, showing the stage tilt and surface curvature.

The tilt was removed mechanically by designing and mounting a tilt aligner on top of the stage, but it was not removed completely because of the limitations in manual and mechanical alignments. This tip tilt aligner was an extra stage with capability of rotating toward an angle using screws and springs as illustrated in Figure 75.

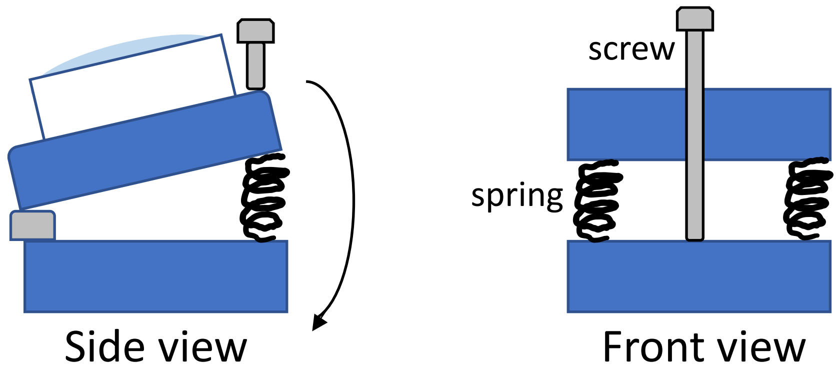

Figure 75. Schematic of the tip-tilt aligner functionality.

For removing the remained tilt and the surface curvature it was also necessary to remove the errors analytically. Figure 76, is showing the raw measurements of the sample and Figure 77 is indicating the results of the measurements after processing and removing the tilt and surface's curvature. This result is also compared with the stylus profilometer measurements as a reference. The amplitude of 40 µm for the raw data is because of the tilt and the curvature of the surface and shows up over the range of 1.2 mm lateral scan. This error is removed in the compensated results.

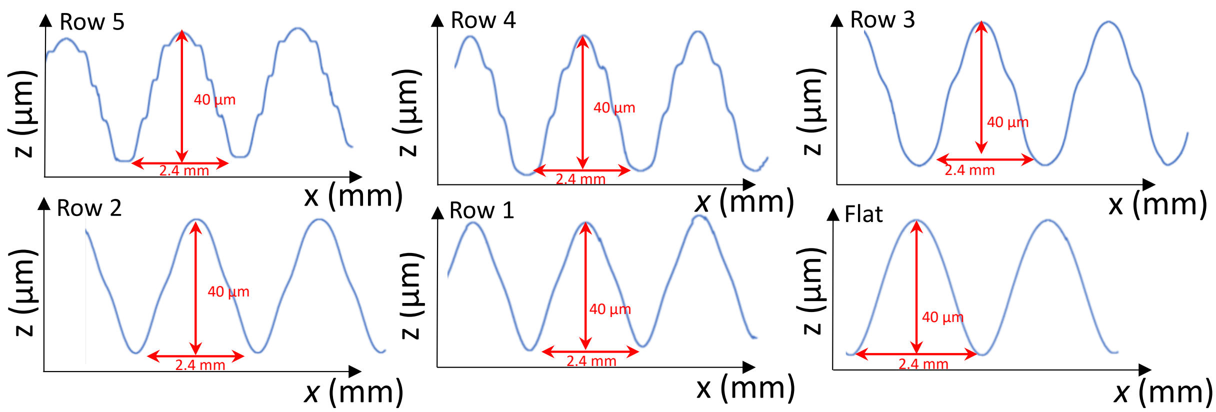

Figure 76. The raw measurements of the diamond turned aluminum surface profile for Row 5 to Raw 1 and the flat area using one-directional probe, before curve removal

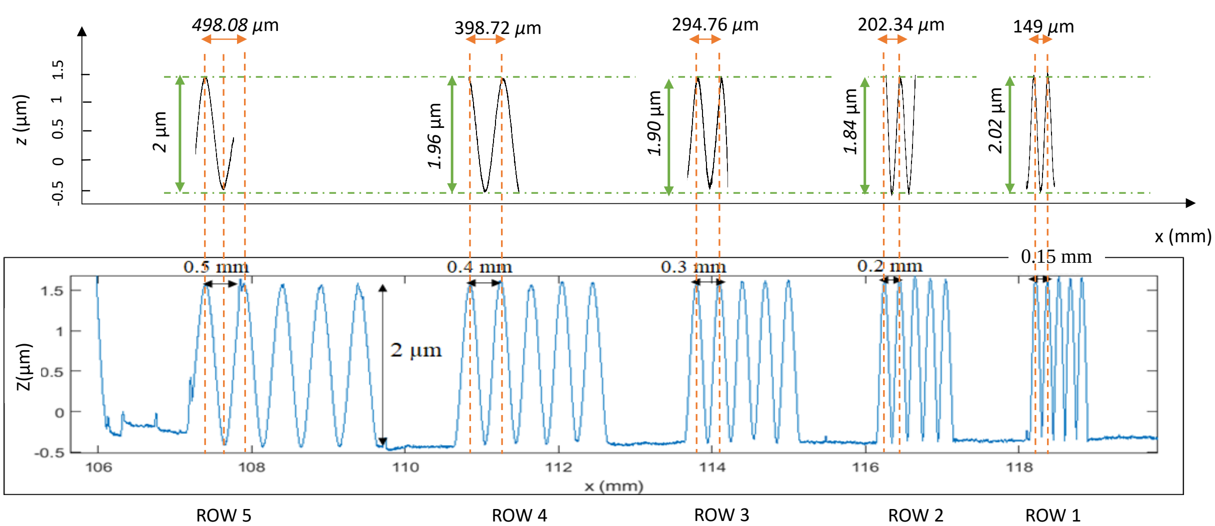

Figure 77. The profile measurements of a diamond turned aluminum surface sample using one-directional probe, after curve removal and compare the results with stylus profilometer measurements.

5-3-2-6 SIGNAL CONDITIONING

The signal conditioning unit consists of two main parts, and these are the photodetectors signal prior to digitization and the modulation signal to be applied to the piezoelectric actuators. The signals from photodetectors are weak and need to be amplified before digital conversion for Fourier transformation. Also, for increasing the stability, it was necessary to remove the DC component of the signal by using high-pass filters. After filtering, the signal goes through an offset and gain circuit to increase the amplitude. The last step is converting to a digital number using 16 bit analog to digital converters and transferring these numbers to the NI myRIO to apply the Fourier transform and demodulation analysis. Figure 78, is a diagram of photodetector signal reading part and Figure 79, is a Multisim screening of the whole signal conditioning units.

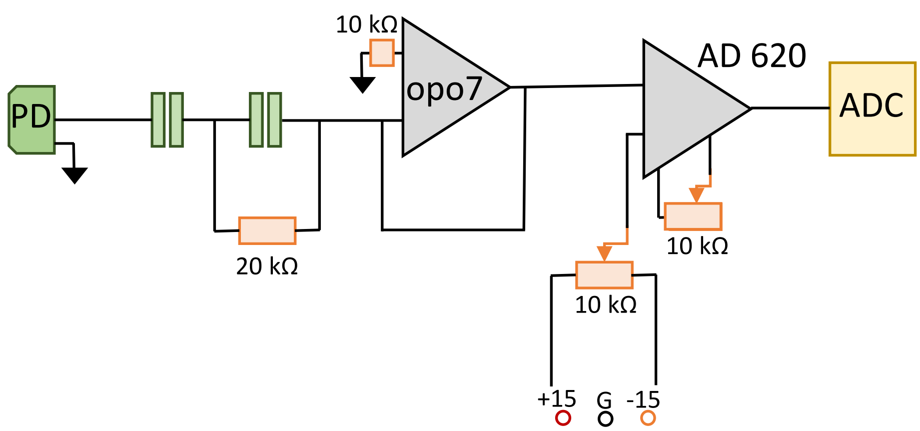

Figure 78. A diagram of signal conditioning unit, photodetector signal reading part.

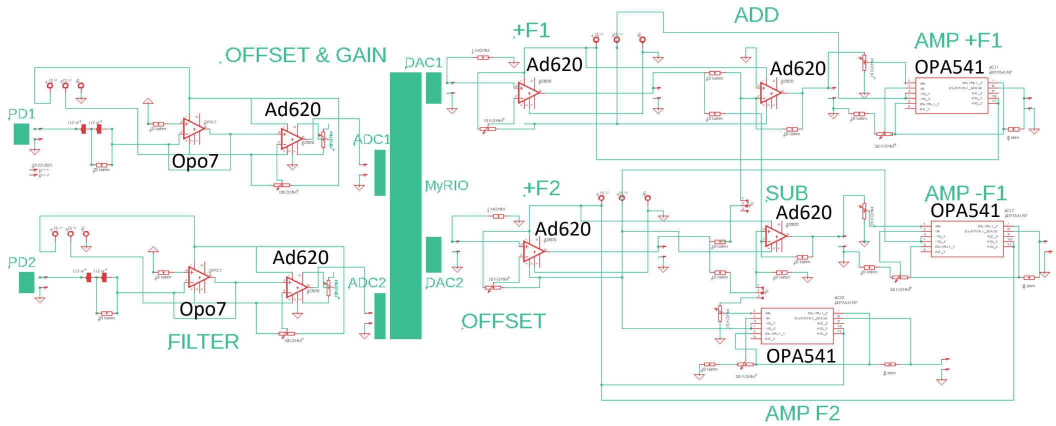

Figure 79. A schematic of a circuit diagram for all components of the signal conditioning unit.

The other main component of the signal conditioning circuit diagram is the modulation units. The generated modulation frequency produced in LABVIEW FPGA program, first needs to get its DC component set to zero using an offset circuit, after outputting from the digital to analog converter (the PMOD DAC generates a positive signal), and after that the two frequencies ω_1 and ω_2 are added and subtracted to generate $\omega_1 + \omega_2$ and $\omega_1 - \omega_2$. The reason of generating these signals is to actuate the piezo electric actuator tube into two orthogonal directions, each with one of these frequencies. This happens because, by applying $+\omega_1$ on all four electrodes of the tube actuator, it will extend and actuate in the Z direction with ω_1 frequency, and by applying $+\omega_2$ on two neighbor electrodes and $-\omega_2$ on the two opposite electrodes, the tube actuator oscillates into the X direction with ω_2 frequency. Figure 80, is a diagram of the modulation signal part and Figure 81 is showing a picture of the whole signal conditioning units.

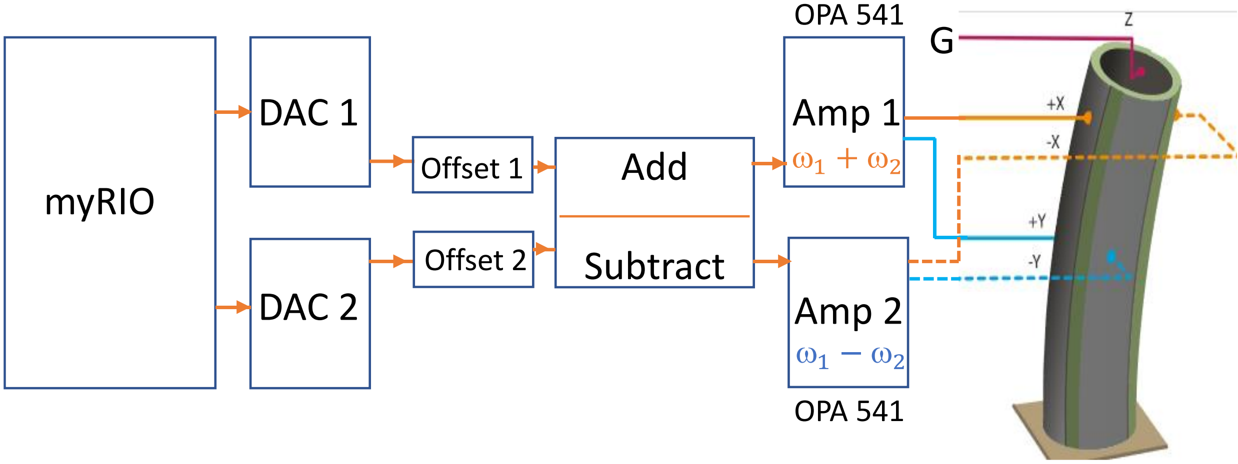

Figure 80. A diagram of signal conditioning unit, modulation signal part.

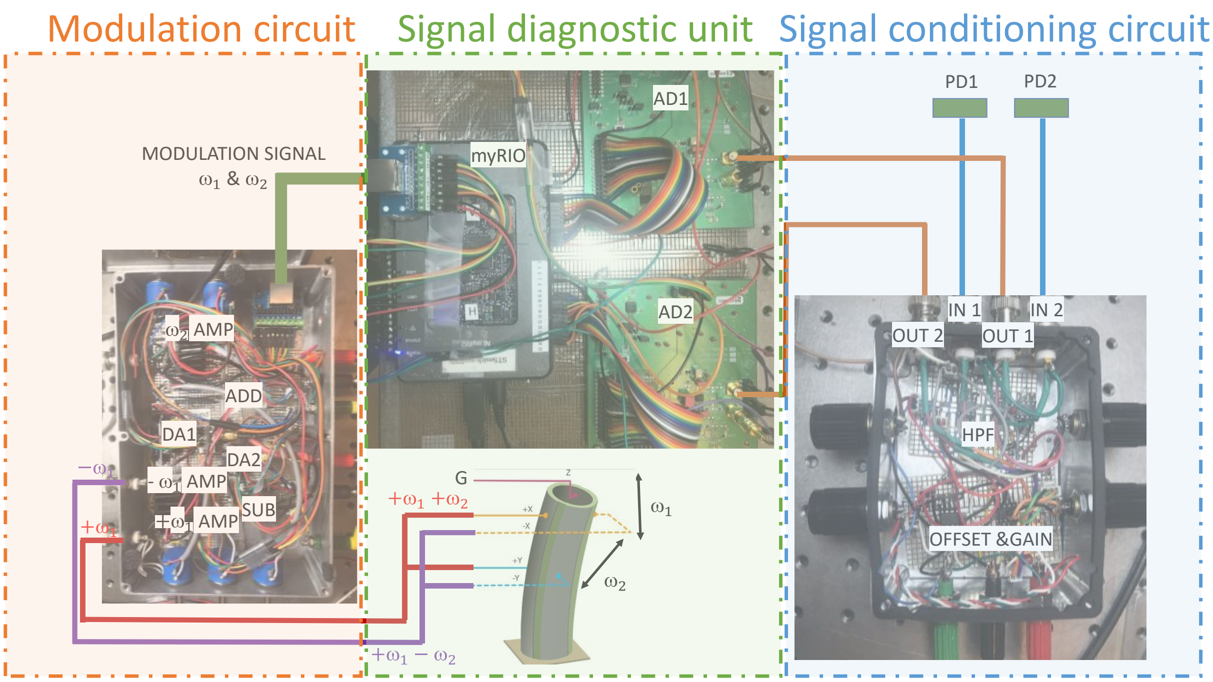

Figure 81. A picture of the signal conditioning units including the ADC's, Modulation unit and signal diagnostic unit.

5-3-2-7 LASER STABILITY

For choosing the best laser diode solution for doing Fabry-Perot interferometry for this experiment, several performance parameters were considered these being: compactness, cost, short wavelength, stability, and power. Although all these parameters were important the most important thing that had to be considered was intensity and frequency stability. For the purpose of choosing the best available laser, a comprehensive study was carried out for testing and documenting different lasers stabilities. Table 3 shows reduced listing of information gathered and it is described in more detail in Appendix B.

Table 3. Stability measurements of different laser diodes (appropriate for interferometry purpose).

Laser Description	Average Power [mW]	Power Fluctuation [µW]	Signal to Noise	Signal to Noise Ranking
Thorlabs HL6312G	0.847	1.82	465	1
VLM-6500003-LPA2	2.078	7.1	293	2
Ebay Dot Laser	35.98	318	113	4
VFL	29.5	307	31	6
US Laser M635-5I	3.92	20.2	194	3
Q-Photonics QFLD-635-40S (100 mA drive current, 25°C)	11.65	144	81	5

After inspecting the available options for choosing the appropriate laser, making a current driver circuit was the next step to ensure that we get the best stable signal out of the chosen laser. This circuit is designed to work on two modes of current feedback and photodiode feedback. The circuit is a simple closed loop feedback control system that supplies the feedback from either the current through the reference resister or the photodiode placed into the laser circuit. Figure 82 shows the picture and the diagram of this current controlled driver circuit.

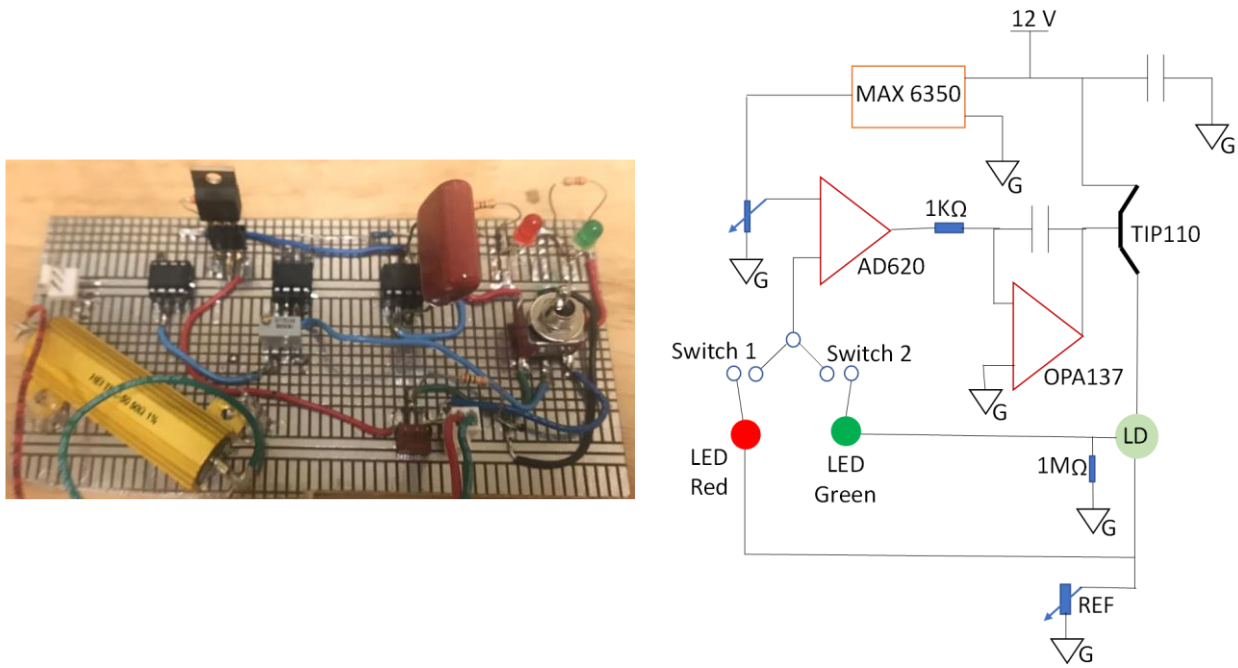

Figure 82. Laser current driver circuit picture (left), and diagram (right).

After current controlling, the last step was to couple the laser light into a fiber and also pass the light through an optical isolator to avoid back reflections. For that purpose, two collimating lenses are used and a V groove alignment fixture for holding these lenses coupled into the fiber and laser was designed. This V groove was designed to provide the appropriate location for keeping two lenses parallel to minimize manually angular alignment of the laser using a tip-tilt aligner and a x-y-z stage to optimally launch into the fiber. Figure 83 shows the solid model and a picture of the setup for laser to fiber coupler.

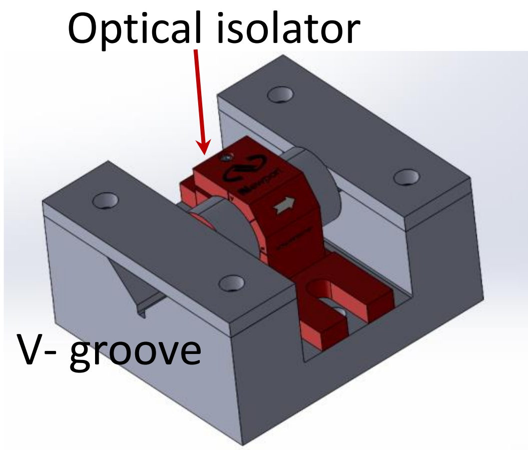

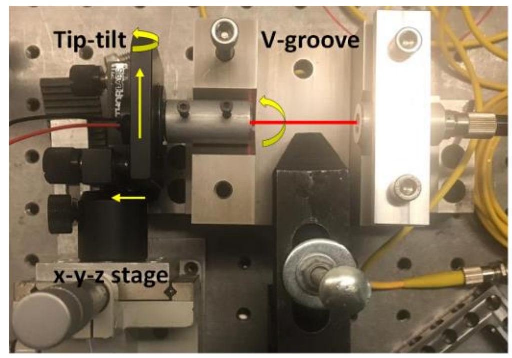

Figure 83. Solid model (left) and a picture of the setup (right) for the laser to fiber coupler V groove and optical isolator.

CHAPTER 6 SURFACE MEASUREMENTS

6-1 UNI-DIRECTIONAL PROBE MEASUREMENTS

A photograph of the experimental apparatus showing the GRIN lens-based fiber probe measuring the central portion of the test specimen is shown in Figure 84. In this experiment a diamond turned (it has five groups of ripples on top with different spacing between them starting from 0.15 mm to 0.5 mm and heights of 2 µm) polished aluminum sample is being inspected using the uni-directional Fabry Perot interferometer, fiber-based probe. The solid model of this sample and a cross-sectional view of the sinusoidal waves diamond-turned on its surface is illustrated in Figure 85. The uni-directional fiber probe and specimen traverse stage have been fabricated and tested with major performance parameters listed in Table 4.

Table 4. Uni-directional probe specifications.

specification	Working distance	Vertical resolution	Lateral resolution	Vertical range	Lateral range	speed
value	0 – 1 mm	3.25 nm	17.5 µm	10-300 µm	1.2 mm	0.1 mm/s

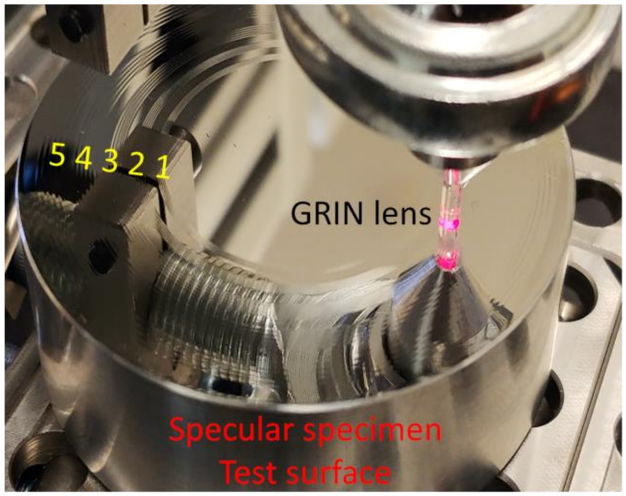

Figure 84. Specular specimen test surface, made for evaluation of uni-directional probe.

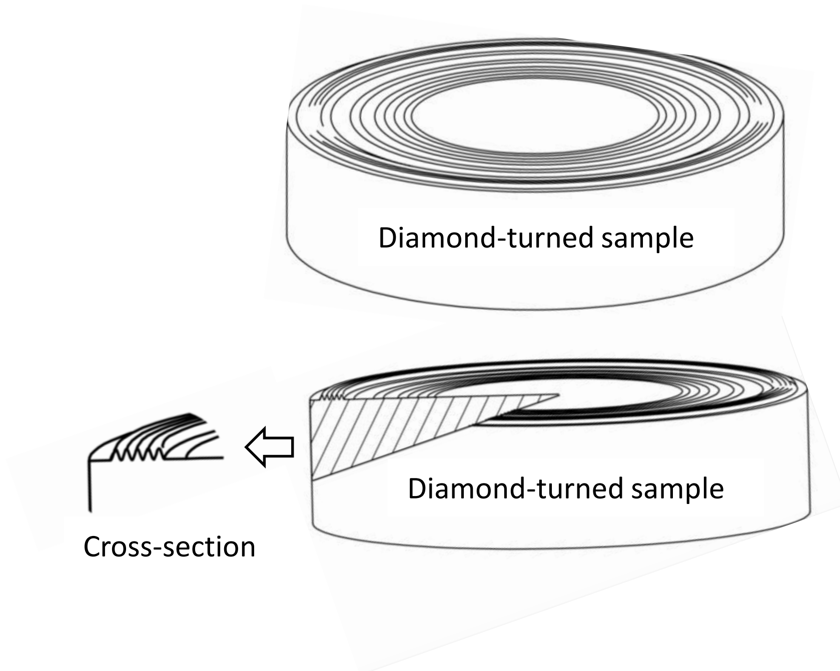

Figure 85. Solid model and the cross-section of the diamond-turned sample. The sinusoidal surface variation has been exaggerated for visualization.

Figure 86 (top part) shows preliminary measurements of the test specimen surface on a section containing a sinusoidal profile with peak to valley amplitude 2 μm and 0.15, 0.20, 0.30, 0.4 and 0.5 mm lateral spacing (wavelength). For comparison, measurement in a similar region using a stylus profilometer (Mahr LD260) is also shown in Figure 86 (bottom part). The deviations between the measurements are comparable to the expected uncertainties of the two profilometers. The stylus profilometer has resolutions in the sub-nanometer range and residual noise of <20 nm rms. When measuring there are additional disturbances from mechanical vibrations and deviations from rectilinearity of the slideway bearing. A reasonable estimate for measurement uncertainty based on characterization measurements would be about 10-15 nm (Arumugam, 2021).

Figure 87 shows the comparison results of the uni-directional optical probe and the Stylus profilometer probe in both the horizontal (spacing between the ripples) and vertical (height of the ripples) measurements for all five rows of ripples on the diamond turned aluminum sample. From these analysis the rms deviation is comparable to the uncertainties of both probes at the 10-15 nm level.

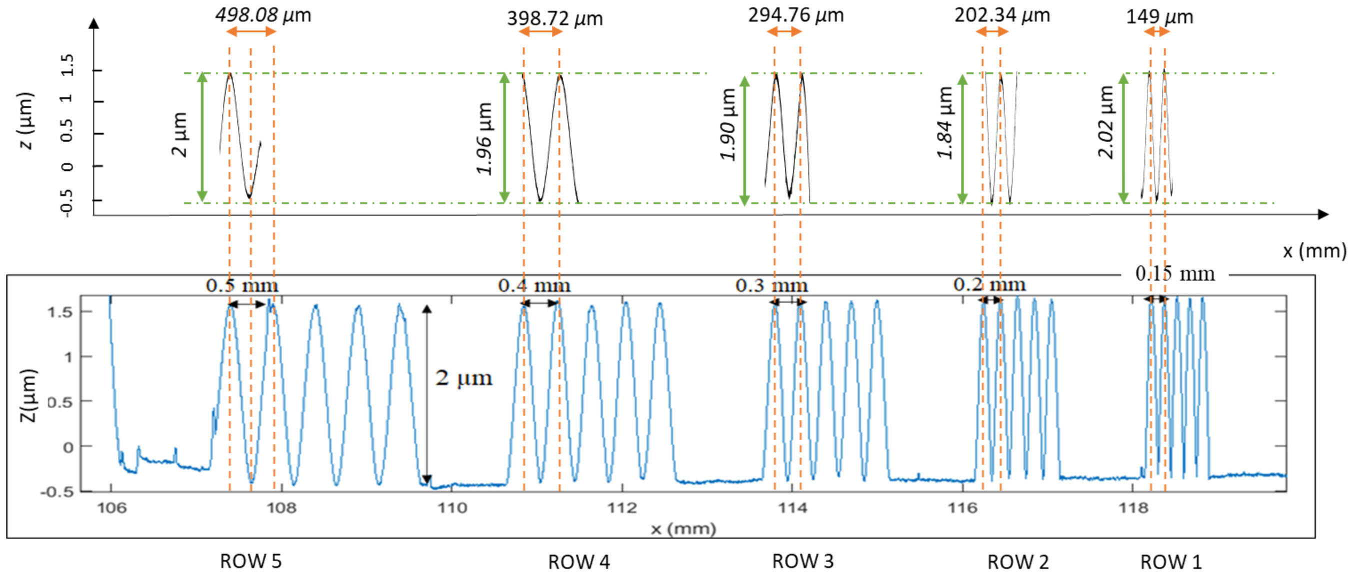

Figure 86. Measurements of a profile of the specimen surface using uni-directional probe (top), compared to stylus profilometer probe measurements (bottom).

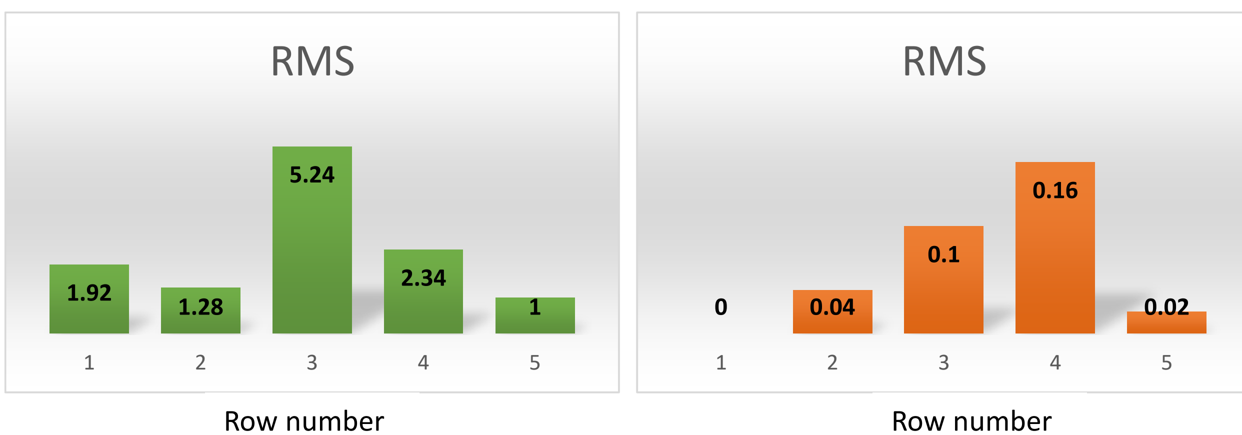

Figure 87. RMS calculations of comparing the uni-directional optical probe and the Stylus profilometer probe.

6-2 BI-DIRECTIONAL PROBE MEASUREMENTS

Results of measurements from both the switched single-source and the dual-source probes described in Section 5-3-1 are presented here. In both experiments, the reference surfaces are slowly modulated, and both capacitance and unwrapped phase displacement signals are simultaneously recorded.

6-2-1 SHUTTER METHOD SURFACE MEASUREMENTS

Motions of the two orthogonal surfaces (mirrors being displaced along the respective optic axes) measured using the single-source probe are shown in Figure 88. In both plots in Figure 89, the solid line represents interferometric measurements, and the dashed line represents measurements of the mirror motion using capacitance displacement gauges. In this figure, displacement of mirror 2 is shown top left and, displacement of mirror 1 top right. Optical probe measurements are shown by a solid line, and capacitance gauge output is shown by a dashed line. Displacement measurements of both mirrors is represented on the lower graph. Each plot contains 5000 measurement points over a three second period. The apparent 180-deg phase shift between the capacitance sensor and the probe measurements is because, in the setup of this experiment, motion of the mirror for an increasing probe gap corresponds to a decrease in separation of capacitance electrodes. This inversion of sensor sensitivities also helps to separate the two signals that would otherwise overlap making comparison difficult. Both measurements indicate a cyclic motion of peak-to-valley amplitude 1.5 μm that corresponds to an optical path length change of 4.7 fringes for the 633-nm source.

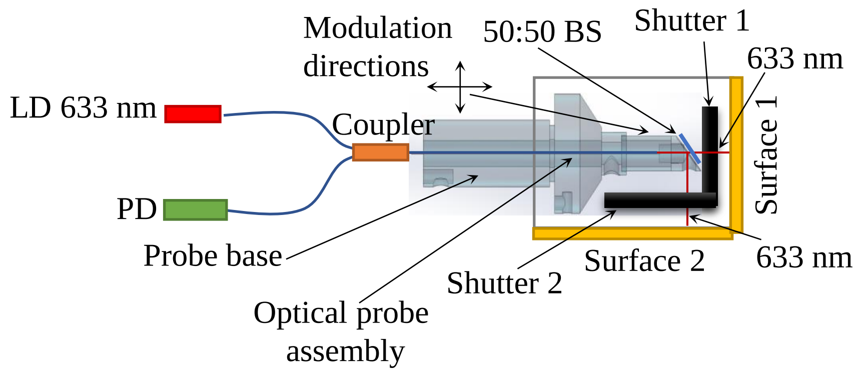

Figure 88. schematic of shutter method single source probe for two-directional measurements.

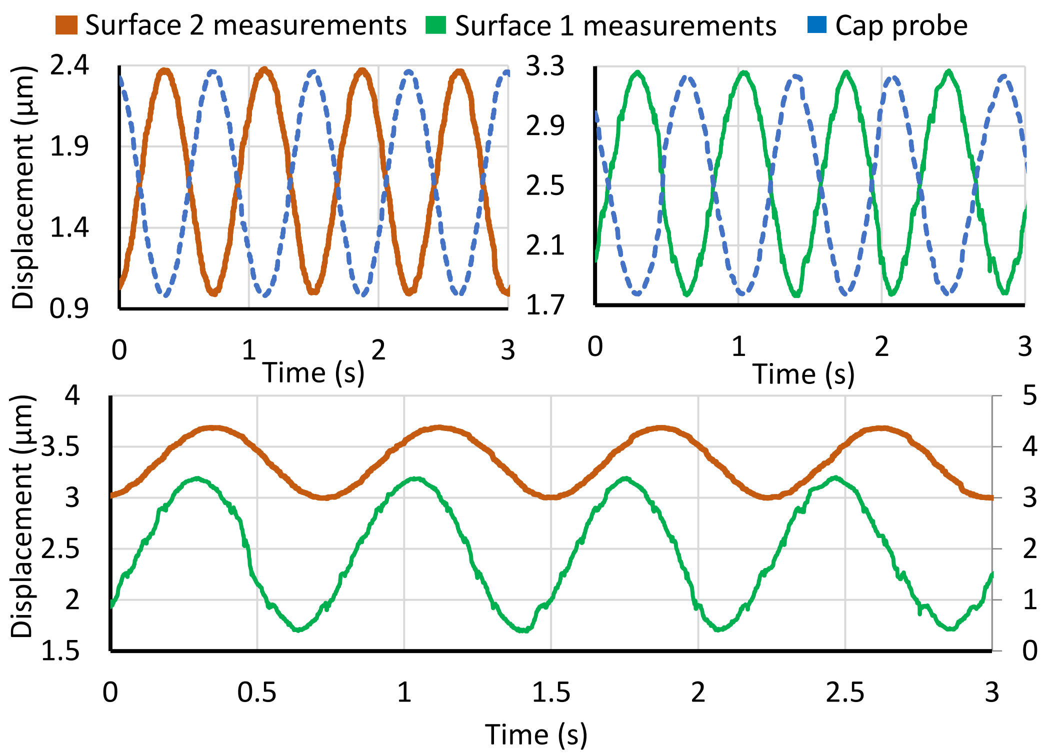

Figure 89. Single-source probe measurements of sinusoidally moving mirror displacement of amplitude 1.5 μm (approximately five fringes) over a measurement time of 3s.

Analysis for single-source probe measurements results in a rms noise of 9.7 nm on the vertical axis and 7.9 nm on the horizontal axis. These results are shown in Figure 90 and Figure 91.

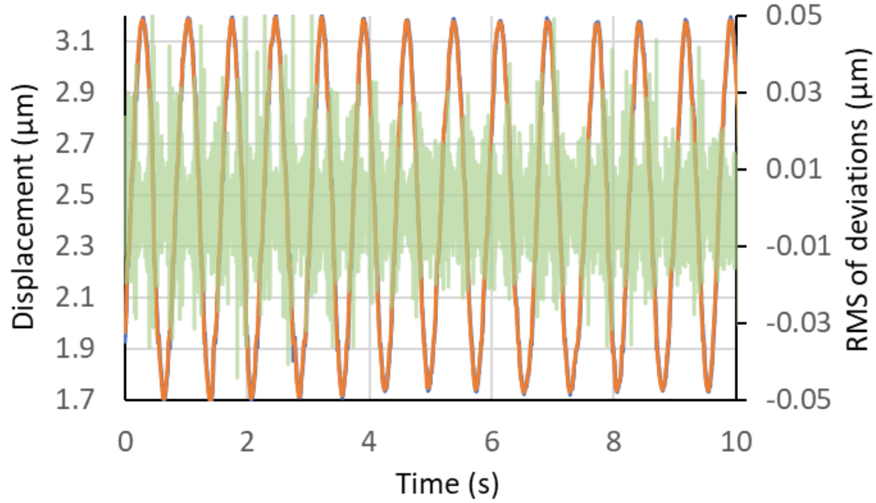

- STDEV 0.009747 (µm)
- Modulation frequency 2.39 kHz

Figure 90. Displacement and rms noise measurements of single-axis probe vertical axis.

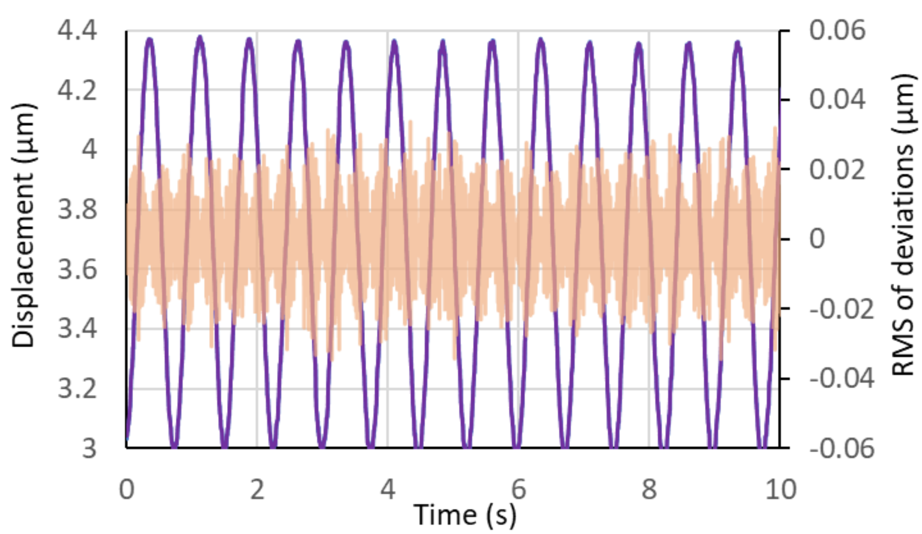

- STDEV 0.007901 (µm)
- Modulation frequency 2.43 kHz

Figure 91. Displacement and rms noise measurements of single-axis probe horizontal axis.

6-2-2 TWO WAVELENGTH SIMULTANEOUS SURFACE MEASUREMENT

Figure 93 shows similar measurements as Figure 89, only, in this case, the measurements were obtained simultaneously using the dual-source probe. In this figure, displacement of mirror 2 is shown over a measurement time of 2 seconds at top left, and displacement of mirror 1 over a measurement time of 10 seconds, top right. Optical probe measurements are shown by a solid line, capacitance gauge output is shown by a dashed line, and simultaneous optical probe measurements of both axes' signals over a period of 2.5 seconds, lower plot. For these measurements the peak-to-valley amplitude was 2.1 µm with the optical measurements being shown as a solid line, and capacitance displacements were again shown as dashed lines. For this set of measurements, the mirrors were cycled backwards and forwards at different rates to demonstrate the independence of measurement more clearly.

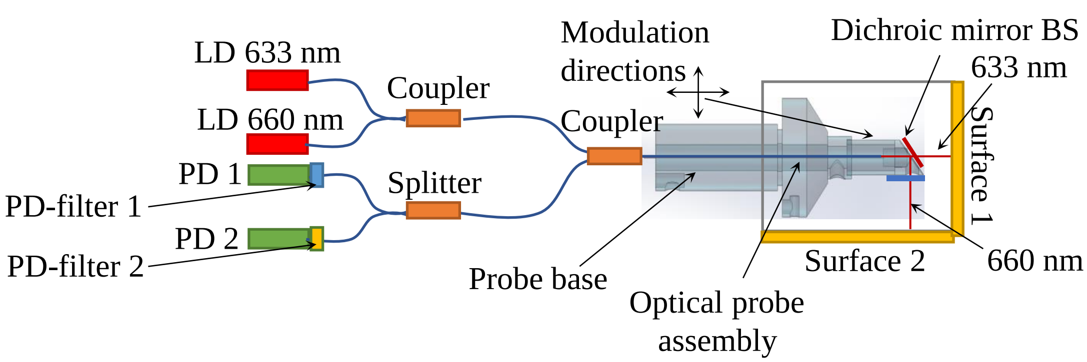

Figure 92. Dual source probing method for two directional measurements.

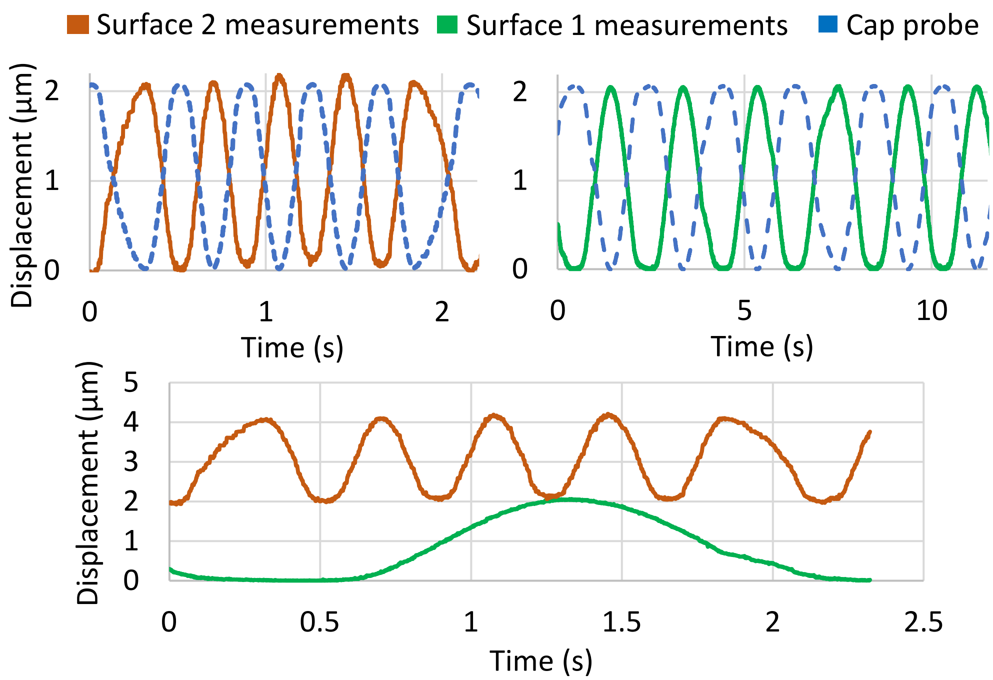

Figure 93. Simultaneous mirror measurements using the dual-source probe for sinusoidally moving mirror displacements of amplitude 2 µm (approximately seven fringes).

For evaluation of the noise, a digital high-pass filter with a cutoff frequency of 0.1 Hz is applied to the dataset, and the residuals of each measurement are computed. For the dual-source probe, the filtered noise measurements are shown in Figure 94 and Figure 95 from which a rms value of 8.1 nm was measured for each vertical and horizontal probe axis.

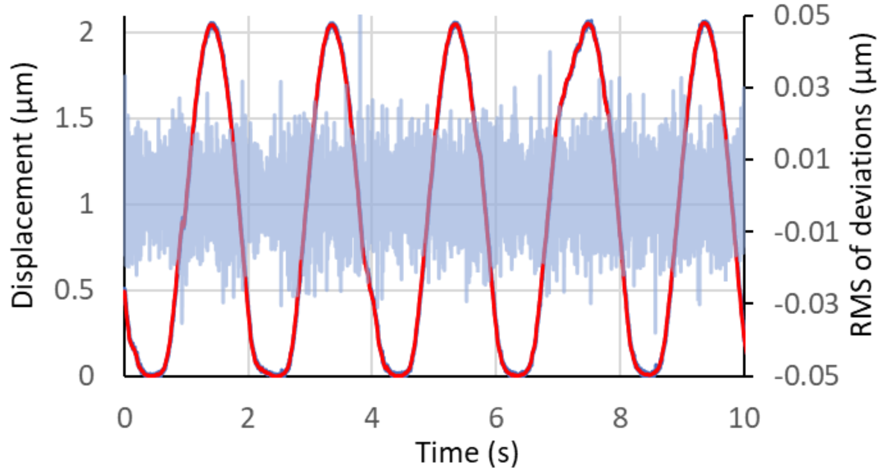

- STDEV 0.008094 (µm)
- Modulation frequency 819.001 Hz

Figure 94. Displacement and rms noise measurements of dual-axis probe vertical axis.

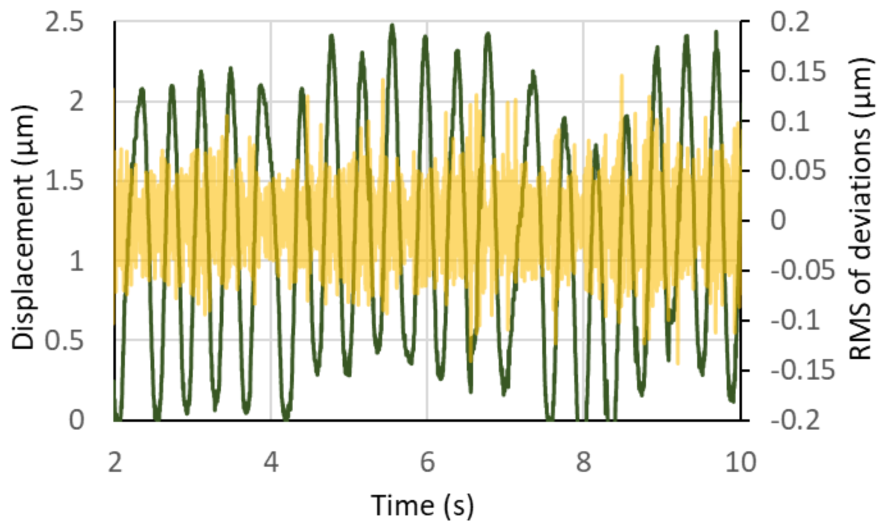

- STDEV 0.008094 (µm)
- Modulation frequency 232.234 Hz

Figure 95. Displacement and rms noise measurements of dual-axis probe horizontal axis.

6-3 CONCLUSIONS

This chapter has demonstrated the use of a multi-axis fiber-based displacement probe utilizing Fabry–Perot interferometry and mechanical modulation to obtain quadrature signals. Utilizing these principles, two probe designs have been fabricated, one being a shuttered single source probe, and the other being a dual-source probe with simultaneous measurement. The current optical probe design is 5-mm diameter and 20-mm long and can be readily attached to any supporting instrument structure. Both probes demonstrated noise during measurement of the moving mirrors consistently lower than 10-nm rms over a bandwidth limited to the mechanical modulation frequencies that range between 200 Hz and 2.43 kHz for the current probe designs. Whereas, these carrier frequencies are limited by available amplifiers and components of assembly, in principle, there is no reason why these cannot be substantially increased by using more compact lighter components of assembly and more powerful electronic drivers. Noise measurements with the mirrors being stationary indicated a noise floor of less than 3 nm. The reason for the increased noise during measurement is likely a combination of mechanical and electrical noise of the translation of stage and experimental apparatus. Fabrication and operation of these probes was not without challenges. One of the major challenges was obtaining high power (greater than 20-mW) stable laser diode sources. In previous work, laser diode sources capable of providing stable Fabry–Perot measurements over a period of greater than 19 h using a 30-mW source in a temperature- and humidity-controlled environment have been demonstrated. The sources used in this paper were operated at 11.6 and 22.5 mW power in standard laboratory environment and showed considerably less stability under these environmental conditions. The reference surface for Fabry–Perot interferometry was the surface at the fiber-GRIN lens interface. In practice, this resulted in photodiode harmonic voltages of a few millivolts or less that had to be substantially amplified prior to Fourier analysis, a process that resulted in a reduced signal to noise. For more optimal probe design, the reflectivity of the reference surface should be matched so that the two interfering beams are of similar intensity. For the purpose of demonstrating operation, these probes were fabricated from separately manufactured components. A more compact probe would result by directly depositing the mirror coatings and using modulation actuators of dimensions comparable with the GRIN lens. A more compact design would also facilitate measurement in more confined spaces and likely increase modulation frequencies.

CHAPTER 7 CONCLUSIONS AND FUTURE WORK

7-1 CONCLUSIONS

This thesis presents design, fabrication, integration, test results and evaluation of a novel fiber-base Fabry-Perot interferometer probe system, which is suitable for metrological inspection of hard to access surfaces and capable of operating in confined spaces. To achieve this functionality, laser diode stabilization was studied, and techniques implemented to provide a stable and coherent light source for interferometric displacement measurement. The Fabry Perot configured interferometer utilizing this stabilization was evaluated with a Michelson configuration standard optical assembly. In this study, signal modulation techniques were also introduced for quadrature phase detection. Signal processing and quadrature phase extraction was implemented in an FPGA processor. Also, analog signal conditioning was implemented for modulation harmonic extraction, offset removal, and amplification.

A novel fiber based compact multi-axis surface measuring probe is invented in this thesis and three variants corresponding to a one directional probe, a single source-two directional probe, and a dual source-two directional probe have been designed and built. After performing the probe fabrication and validation of operation, surface measurement capabilities of all probe systems are demonstrated. Developments required to create this functionality include

- Stabilized laser diodes for interferometric displacement measurement (Ch 5).
- Utilize these stabilized sources as Fabry Perot configured interferometer demonstrated with Michelson configuration standard optical assembly (Ch 5).
- Utilization of modulation for quadrature detection (Ch 5).
- Implemented signal processing and quadrature phase extraction in an FPGA processor (Ch 5).
- Implemented analog signal conditioning for modulation harmonic extraction, offset and amplification (Ch 5).

- Invented a novel fiber-based, compact, multi-axis surface measuring probe (Ch 4).
- Designed and built three variants of the probe (Ch 4).
- Performing probe fabrication and validation of operation (Ch 4).
- Demonstrated surface measurement capabilities of all probe systems (Ch 6).

Having demonstrated operation of a prototype multi-axis probe, to assess performance it is necessary to understand that contribute to measurement noise. A list of noise sources and an estimate of their contribution is listed in Table 5. For comparison the performance of a similar modulated fiber interferometer is also listed. The interferometer used in this comparison comprises only a two-by-two fiber-coupler with the modulated reference mirror providing the signal on one fiber and the test specimen mirror being measured by the second fiber. For this reference system the separation between fibers and mirrors are optimized to maximize signal to noise and the whole system is operated in a temperature-controlled laboratory environment.

Table 5. Noise contributions of the multi-axis probe and a comparison with a Michelson interferometer utilizing the same modulation, phase extraction method.

Spec/Number	***Signal to noise**	**Bandwidth**	***Displacement resolution**	**Reflections within the optical system**	**Analog to digital converter noise**	**Modulation depth control**	**Losses in the optics (BS, FILTER, DM)**	**Fiber coupling to the returned beam, (Distance from probe surface, %)**	**Surface tilt**	**Reference**
Reference system	3.36	20 Hz	30 nm	Unknown	2 bits	150 nm	% 66.31	0.2 mm, 5% 1 mm, 0%	Not measured	(Hasting, 2021)
Multi-axis probe	7.51	18 Hz	14 nm	Unknown	2 bits	112 nm	% 66.31	0.2 mm, 5% 1 mm, 0%	Not measured	This thesis

*Signal to noise measurement data for the reference system is was obtained for a system that had been in continuous operation for more than a 20-hour period of time in a temperature controlled laboratory environment held at 20±0.1 °C. Additionally, the complete optical system comprised a compact optical assembly fastened to a solid optical bench with a small optical air path. Hench there are substantial differences in terms of size, complexity, and environment with the reference system probably representing more closely the limits of this measurement technique. Optimization of test and experimental conditions for the Multi-axis probe assembly will be a necessary target for future work.

*The displacement resolution for Multi axis probe is showing an improvement. This is speculated to be mainly due to using a GRIN lens so that light is focused rather than the reference system which is not utilizing a focused light for the measurements.

7-2 FUTURE WORK

This section outlines the possible future works to improve the multi-directional Fabry Perot interferometer probe.

The current system is a laboratory demonstration showing the feasibility of the operating principles of this new optical probe. The goal of this study was to demonstrate operation and identify factors influencing probe performance. Based on these studies it is apparent that this system has the capability of improvement in the design, fabrication, and testing.

Both the probe size can be more compact (one of the main motivations for developing this approach) and the test bench for mirror displacement can also be improved for more comprehensive performance testing. Many components of the probe were obtained as stand-alone parts that were then fabricated together to provide full probe functionality. Most of these parts were significantly larger than necessary from a purely functional perspective. For example, deposition of specific dichroic filter coatings could reduce the size of the mirrors and even eliminate one of them. Additionally, piezoelectric displacement is dependent only on voltage and therefore the tube element could again be considerably reduced in size or replaced by even smaller individual elements.

The probe has not been evaluated by measuring profiles of a two-dimensional surface and for this purpose, a two directional sample surface needs to be provided and inspected using the two directional probes plus an independent measuring process for comparison. Also, a new test bench needs to be designed and made to scan two surfaces simultaneously.

The stability of the second laser source used in these studies is still an issue. This will improve the results of measurements substantially.

Most of the mechanical, optical, and electrical components have been manually manufactured and fabricated and they can be made using more controlled production processes. The optical alignments and the test procedure for scanning a two directional sample surface can be automated using two directional stages and dedicated precision fixtures.

The software can be optimized and run on dedicated real-time processors to increase processing speed and consequently the speed of scanning.

And finally, an optical model of the system can be developed in Zemax and optimized to enhance the optical components of the probe.

REFERENCES

1. Byeong Ha Lee, Young Ho Kim, Kwan Seob Park, Joo Beom Eom, Myoung Jin Kim, Byung Sup Rho and Hae Young Choi. “Interferometric Fiber Optic Sensors.” Review of Sensors (2012), volume 12, issue 3, 2467-2486.
2. Yunzhi Wang, Fang Xie, Sen Ma, Lianlian Dong. “Review of surface profile measurement techniques based on optical interferometry”. June 2017, Volume 93, June 2017, Pages 164-170.
3. Groot, Peter de. “Principles of Interference Microscopy for the Measurement of Surface Topography.” Advances in Optics and Photonics 7, no. 1 (2015): 1. doi:10.1364/AOP.7.000001.
4. Mark Davidson, Kalman Kaufman, Isaac Mazor, Felix Cohen, "An Application of Interference Microscopy to Integrated Circuit Inspection and Metrology," Proc. SPIE 0775, Integrated Circuit Metrology, Inspection, & Process Control, (17 April 1987); https://doi.org/10.1117/12.940433.
5. Minsky, M. (1961). Microscopy apparatus (U.S.Patent No.3013467A).U.S.Patent.patents.google.com/patent/US3012467A/en.
6. Artigas R. (2011) Imaging Confocal Microscopy. In: Leach R. (eds) Optical Measurement of Surface Topography. Springer, Berlin, Heidelberg. https://doi.org/10.1007/978-3-642-12012-1_11.
7. T. Dresel, G. Häusler, and H. Venzke. “Three-dimensional sensing of rough surfaces by coherence radar,” Appl. Opt. 31, 919–925 (1992).
8. Francois-Blateyron. “Chromatic Confocal Microscopy.” Optical Measurement of Surface Topography, edited by Richard Leach, Springer, 2011, page 71-91.
9. Apre Instruments. (2018, March 7). Laser Fizeau Interferometer History. https://apre-inst.com/laser-fizeau-interferometer-history/
10. T. T. Kajava, H. M. Lauranto, and A. T. Friberg, "Interference pattern of the Fizeau interferometer," J. Opt. Soc. Am. A 11, 2045-2054 (1994).
11. U. Paul Kumar, N. Krishna Mohan and M.P. Kothiyal. “Multiple wavelength interferometry for surface profiling” Optics and Lasers in engineering, volume 84 p 10-25 (2016).
12. Popescu, Dan P et al. “Optical coherence tomography: fundamental principles, instrumental designs and biomedical applications.” Biophysical reviews vol. 3,3 (2011): 155. doi:10.1007/s12551-011-0054-7
13. Aumann S., Donner S., Fischer J., Müller F. (2019) Optical Coherence Tomography (OCT): Principle and Technical Realization. In: Bille J. (eds) High Resolution Imaging in Microscopy and Ophthalmology. Springer, Cham. https://doi.org/10.1007/978-3-030-16638-0_3
14. Takamasa Suzuki, Jiro Shimazaki, Osami Sasaki, Samuel Choi, "Optical coherence tomography using nonstationary signal processing based on continuous wavelet transform," Proc. SPIE 12057, Twelfth International Conference on Information Optics and Photonics, 120574L (1 November 2021); https://doi.org/10.1117/12.2606987
15. Brezinski, M. Capabilities, limitations, and misconceptions of using OCT to assess vulnerable plaques. Nat Rev Cardiol 11, 638 (2014). https://doi.org/10.1038/nrcardio.2014.62-c1
16. Bak E. (2021) Pitfalls in OCT Imaging. In: Park K.H., Kim TW. (eds) OCT Imaging in Glaucoma. Springer, Singapore. https://doi.org/10.1007/978-981-16-1178-0_9

17. Myung K. Kim, "Principles and techniques of digital holographic microscopy," SPIE Rev. 1(1) 018005 (1 April 2010) https://doi.org/10.1117/6.0000006
18. U. Schnars and W. Jüptner, "Direct recording of holograms by a CCD target and numerical reconstruction," Appl. Opt. 33, 179-181 (1994)
19. Ankesh Tiwari, Pradeep Kumar Yadav, Richa Srivastava and Navin Chaurasiya. "Optical Fiber Sensor: Review and Applications." Optical Fiber Sensor: Review and Applications. Volume 6, Issue 1 March 2018.
20. Garry Berkovic and Ehud Shafir, "Optical methods for distance and displacement measurements," Adv. Opt. Photon. 4, 441-471 (2012)
21. Zhu Nan-nan, Zhang Jun. "Surface roughness measurement based on fiber optic sensor", Measurement, Volume 86, 2016.
22. A. D. Kersey et al., "Fiber grating sensors," in Journal of Lightwave Technology, vol. 15, no. 8, pp. 1442-1463, Aug. 1997, doi: 10.1109/50.618377.
23. Chen, J., Liu, B. & Zhang, H. Review of fiber Bragg grating sensor technology. Front. Optoelectron. China 4, 204–212 (2011). https://doi.org/10.1007/s12200-011-0130-4.
24. B.K. Nowakowski, D.T. Smith, S.T. Smith. "Highly Compact Fiber Fabry-Perot Interferometer: A New Instrument Design." Review of Scientific Instruments (2016). Document.
25. Tao Jin, Wei Wang, Lars Daul, Ludger Koenders and Wenmei Hou. "A low – finesse all – fiber sinusoidal phase modulation interferometer for displacement measurement. " Optics communications (2021). Volume 493.
26. Pratt, Paul R. Wilkinson and John R. "Analytical Model for Low Finesse, External Cavity, Fiber Fabry-Perot Interferometers Including Multiple Reflections and Angular Misalignment." Applied Optics (2011). Document.
27. Arablu, M., Smith, S.T., 2018. Polydyne displacement interferometer using frequency-modulated light. Review of Scientific Instruments 89, 055007. doi:10.1063/1.5026569
28. Lucia Diaz Perez, Kumar Arumugam, Masoud Arablu, Stuart T. Smith. "Combined frequency-modulated signals for two-axis displacement measurement", euspen 19th International conference and Exhibition, Bilbao, ES, June 2019
29. Shabahang, F and S.T. Smith, Optical fiber surface probe using mechanically modulated Fabry Perot interferometry, 36th ASPE Annual Meeting 2021
30. Arumugam, K, Caviness, A, Shabahang, F, Smith, S. "Methods of optical profiling surfaces." 34th ASPE Annual Meeting 2019
31. Hastings, D.J. (2021). Development of an all-fiber homodyne quadrature laser interferometer for integration into a compact thermal actuator(uncc12879) [master dissertation, UNC at Charlotte]. ProQuest Dissertation Publishing.
32. B.K. Nowakowski, D.T. Smith, and S.T. Smith. "Highly Compact Fiber Fabry-Perot Interferometer: A New Instrument Design", Rev. Sci. Instrum. 87(11), 115102 (2016).
33. M. Schulz, and P. Lehmann, "Measurement of distance changes using a fiber-coupled common-path interferometer with mechanical path length modulation", Measurement Science and Technology 24(6), 065202 (2013).
34. M. Arablu, S.T.Smith, "Polydyne displacement interferometer using frequency-modulated light", Review of Scientific Instruments 89(5), 055007, (2018).

35. A. J. Boef, “Interferometric laser rangefinder using a frequency modulated diode laser”, Appl. Opt. 26(21), 4545-50, (1987).
36. Byung Seon Chun; Kwangsoo Kim; Daegab Gweon; *Review of Scientific Instruments* 80**,** 073706 (2009)
37. X. Pan, Y. Dong, J. Wen, Y. Huang, C. Deng, and T. Wang, "Highly sensitive Temperature Sensor of Fiber Bragg Grating on PbS-doped Silica Optical Fiber," in 26th International Conference on Optical Fiber Sensors, OSA Technical Digest (Optica Publishing Group, 2018), paper ThE1.
38. Požar, T., and J. Možina. "Enhanced ellipse fitting in a two-detector homodyne quadrature laser interferometer." Measurement Science and Technology 22.8 (2011): 085301.
39. Shabahang, Farzaneh, and Stuart T. Smith. "Multi-axis modulated compact fiber-based Fabry–Perot interferometric probe." Applied Optics 61.10 (2022): 2768-2774.

APPENDIX A

MATLAB program for simulating a modulated signal and extract harmonics out of it

```
clc;
clear all;
close all;
w1=0.01;
w2=0.02;
t=1:1000;
phi1=(2*pi*w1*t);
phi2=(2*pi*w2*t);
A=1;
B=1;
w1m=0.1;
w2m=0.2;

I(t)=1/16*(3+2*cos(phi1).*(besselj(0,A)+2*besselj(2,A)*cos(4*pi*w1m*t))-
2*sin(phi1).*(2*besselj(1,A)*sin(2*pi*w1m*t))+2*cos(phi2).*(besselj(0,B)+2*be
sselj(2,B)*cos(4*pi*w2m*t))-
2*sin(phi2).*(2*besselj(1,B)*sin(2*pi*w2m*t)))+1/16*(2*cos(phi1).*(2*besselj(
4,A)*cos(4*pi*w1m*t))-
2*sin(phi1).*(2*besselj(3,A)*sin(6*pi*w1m*t))+2*cos(phi2).*(2*besselj(4,B)*co
s(4*pi*w2m*t))-2*sin(phi2).*(2*besselj(3,B)*sin(6*pi*w2m*t)));

I0(t)=1/16*(3+(2*cos(phi1).*(besselj(0,A)))+(2*cos(phi2).*(besselj(0,B))));
I1(t)=1/16*(-2*sin(phi1).*(2*besselj(1,A)*sin(2*pi*w1m*t))-
2*sin(phi2).*(2*besselj(1,B)*sin(2*pi*w2m*t)));
```

```
I2(t)=1/16*(2*cos(phi1).*(2*besselj(2,A)*cos(4*pi*w1m*t))+2*cos(phi2).*(2*bes
selj(2,B)*cos(4*pi*w2m*t)));


I11(t)=1/16*(-2*sin(phi1).*(2*besselj(1,A)*sin(2*pi*w1m*t)));
I12(t)=1/16*(2*cos(phi1).*(2*besselj(2,A)*cos(4*pi*w1m*t)));
I21(t)=1/16*(-2*sin(phi2).*(2*besselj(1,B)*sin(2*pi*w2m*t)));
I22(t)=1/16*(2*cos(phi2).*(2*besselj(2,B)*cos(4*pi*w2m*t)));
% after fourier transform:
%  Y11(t)=fft(I11(t));
%  Y12(t)=fft(I12(t));
%  Y21(t)=fft(I21(t));
%  Y22(t)=fft(I22(t));


 Y11(t)=1/16*(-2*sin(phi1)*(2*besselj(1,A)));
 Y12(t)=1/16*(2*cos(phi1)*(2*besselj(2,A)));
 Y21(t)=1/16*(-2*sin(phi2)*(2*besselj(1,B)));
 Y22(t)=1/16*(2*cos(phi2)*(2*besselj(2,B)));
% plot(t,Y22(t))
% hold on
% plot(t,I12(t))
plot(Y11(t),Y12(t))
```

APPENDIX B

Stability test and coupling efficiency measurements for the optical fiber couples and splitters

Table 6. Performance metrics of several commercially available laser sources

Laser Description	Average Power [mW]	Power Fluctuation [µW]	Signal to Noise [-]	Signal to Noise Ranking
Thorlabs HL6312G	0.847	1.82	465	1
VLM-6500003-LPA2	2.078	7.1	293	2
Ebay Dot Laser	35.98	318	113	4
VFL_2	9.5	307	31	6
US Laser M635-5I	3.92	20.2	194	3
Q-Photonics QFLD-635-40S (100 mA drive current, 25°C)	11.65	144	81	5

APPENDIX C

Pictures of the signal frequency analyzing, interferometric fringes, detected quadrature, and the moving stage solid design as supplementary material.

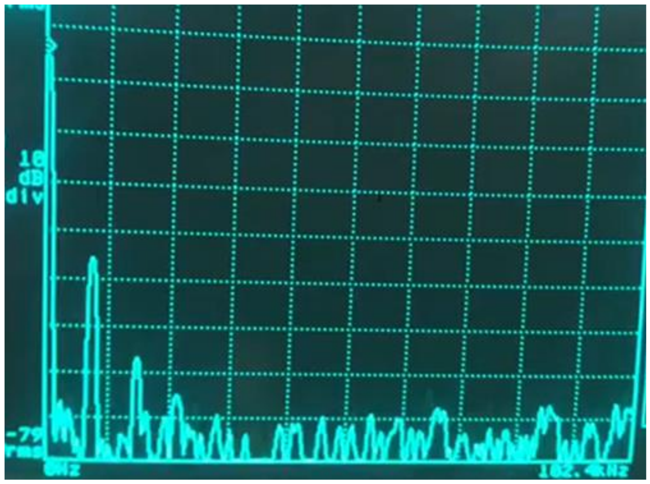

Figure 96. Screening of the signal analyzer showing the harmonics of the modulation.

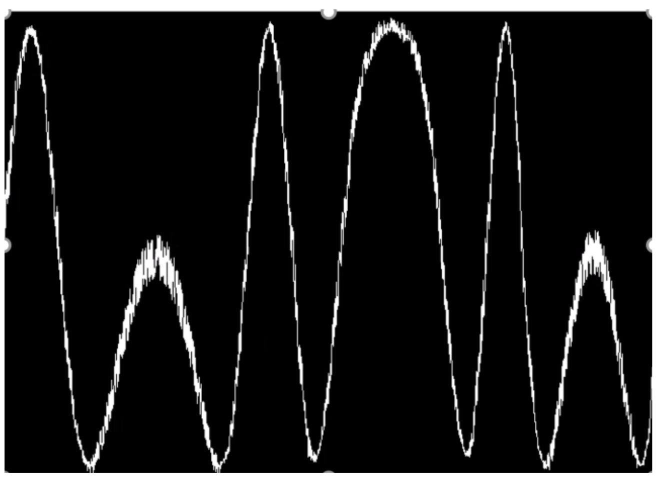

Figure 97. A picture of interferometric fringes before high pass filtering.

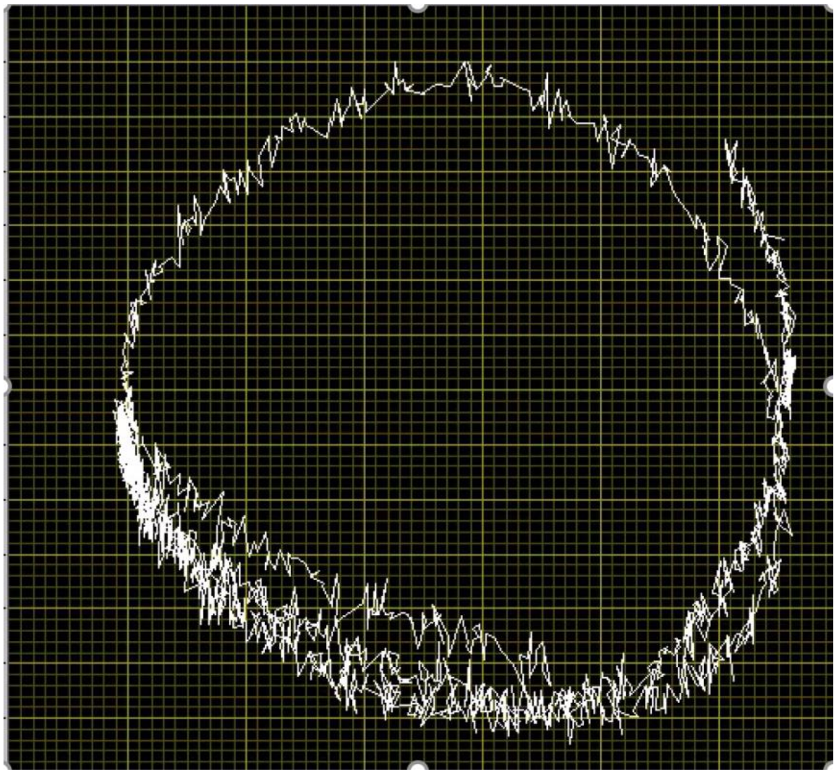

Figure 98. Detected quadrature after plotting the extracted first and second harmonics.

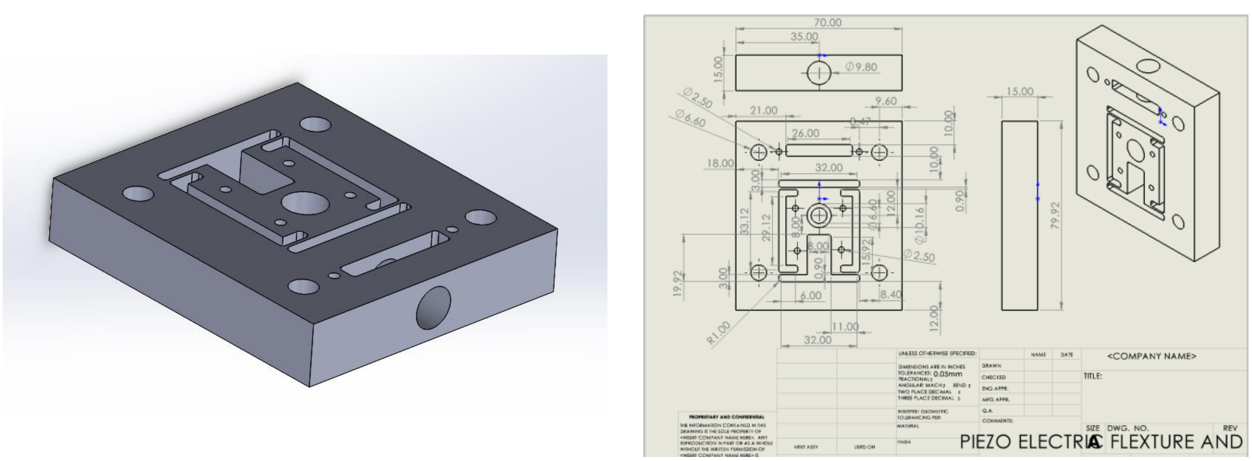

Figure 99. A solid model design for the piezo electric flexure made for the moving stage.

APPENDIX D

LABVIEW directory and the program screening

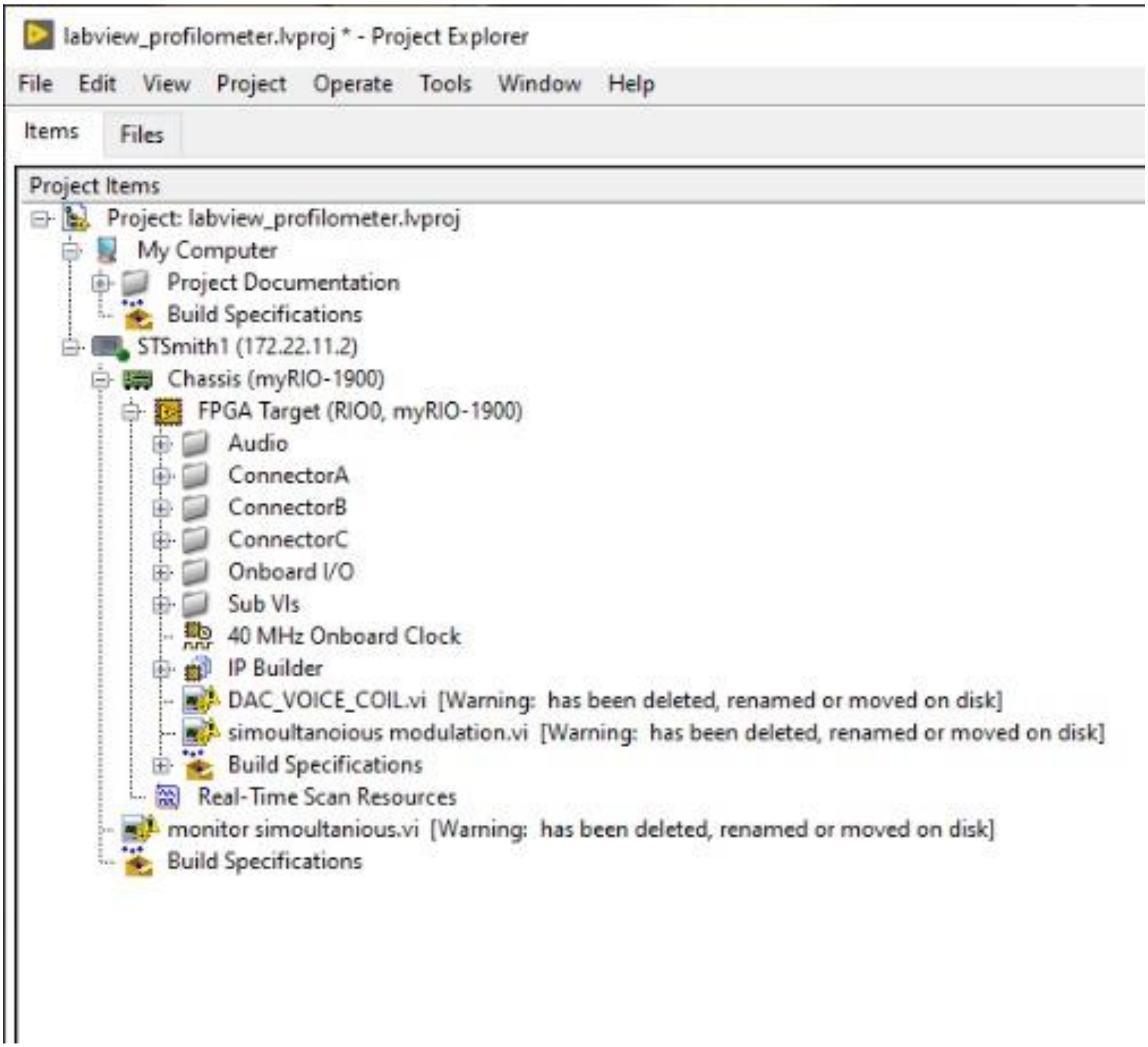

Figure 100. LABVIEW directory

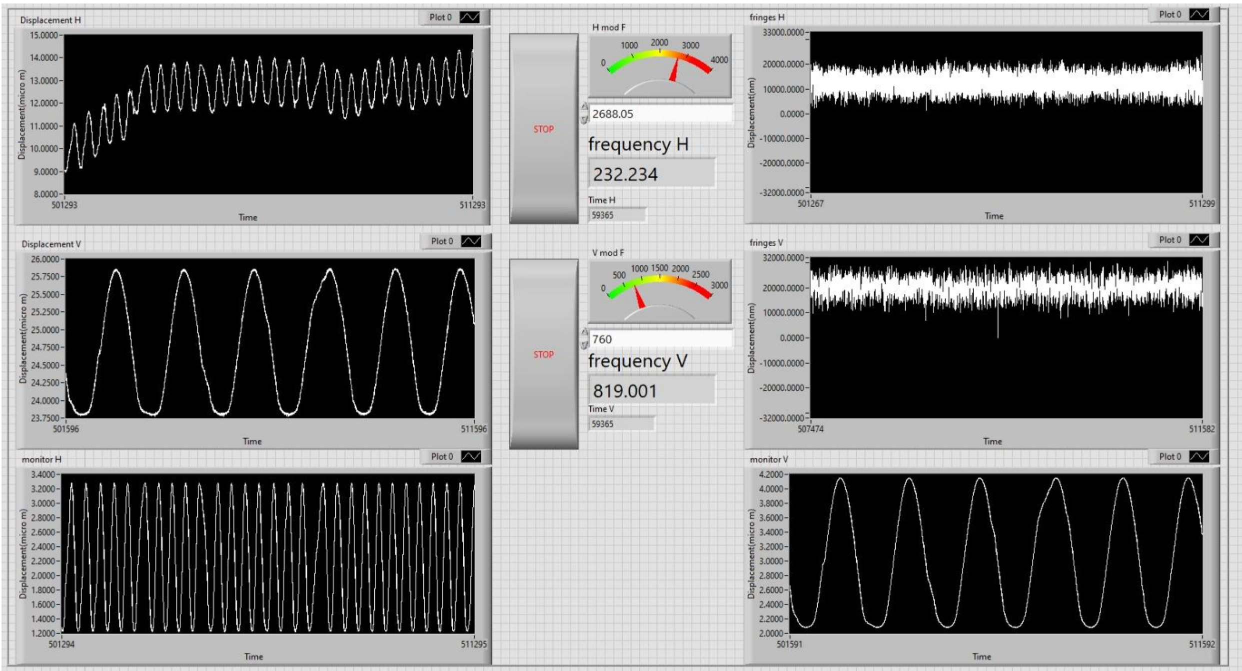

Figure 101. screening of the LabVIEW program showing the measured displacement and the monitored displacement of the stage